

Non-Destructive Evaluation of Material System Using Highly Nonlinear Acoustic Waves

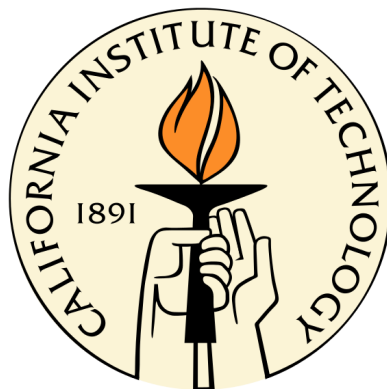
Thesis by

Devvrath Khatri

In Partial Fulfillment of the Requirements

for the Degree of

Doctor of Philosophy



California Institute of Technology

Pasadena, California

2011

(Defended September 30, 2011)

© 2011

Devvrath Khatri

All Rights Reserved

Dedication

To My Parents

Acknowledgements

First and foremost, I would like to thank Almighty God, for giving me the faith to believe and strength to pursue and courage to carry on this work.

I would like to thank California Institute of Technology (CALTECH) and Graduate Aerospace Laboratory at Caltech (GALCIT) for providing me the opportunity to join this great institute as a graduate student and to provide all the resources, which helped me, directly or indirectly, in finishing my studies and research, while making my stay memorable and comfortable.

I take immense pleasure in expressing utmost gratitude to my supervising guide and mentor Professor Chiara Daraio for giving me the opportunity, guidance, and freedom to pursue my research project. I appreciate the amount of motivation, kindness, and patience demonstrated by her throughout my research period. Under her guidance, I have the opportunity to work on cutting edge technology and to learn many things from her, which I am sure will be helpful in different stages of my life. She was always available for guidance and encouragement at short notice, with an open-door policy which helped in moving things faster. It was a wonderful experience and an honor to work with her.

I also want to express my sincere gratitude towards my thesis committee members for their time and helpful suggestions that provided me with extra encouragement, motivation, and guidance to finish my research: Professor Guruswami Ravichandran, Professor Jinkyu Yang, Professor Kaushik Bhattacharya, and Professor Sergio Pellegrino. I also thank the members of my candidacy committee for providing the direction and plan for my research project: Professor Guruswami Ravichandran, Professor Kaushik Bhattacharya, Professor Michael Ortiz, and Professor Sergio Pellegrino.

I owe many thanks to Abha Misra, Alessandro Spadoni, Duc Ngo, Georgios Theocharis, Jinkyu Yang, Malena Espanol, Stephane Job, and Stephane Griffiths for their useful advice and support in numerics and experiments to carry out the research work. In particular, I want to thank Abha, Duc, Jinkyu, and Malena for providing me exemplary guidance and motivation for my doctoral research and also valuable teachings towards becoming better in my future career. I will also like to thank my cousin, Himanshu Khatri, for giving me advice and encouragement regarding finishing my thesis and valuable suggestions for selection of my future career.

I would like to thank some of my other collaborators, with whom I had an excellent chance to work, for their support, which helped me in achieving one step closer to completion: Professor Piervincenzo Rizzo, Professor Fernando Fraternali, Professor Mason Alexander Porter, Professor Ricardo Carretero, Professor Panos Kevrekidis, Xianglei Ni, Claudio Silvestro, Damien Eggenpieler, Stephanie Samson, and Maxime Verriere.

I am also thankful to Joe Haggerty, Petros Arakelian, and Ricardo Paniagua for their valuable suggestions and help in building my experimental setup. I wish to express my thanks to Chinthaka Mallikarachchi and Xiaowei Deng for their useful suggestions on finite element simulations.

I am thankful to Caltech, the National Science Foundation (NSF), and the W.M. Keck Institute for Space Studies (KISS) for their support during my graduate studies. My KISS Graduate Student Fellowship was crucial in allowing me to have the support and freedom to explore the research topics that I am interested in; their financial support is greatly appreciated and it is their generosity that made this research possible.

I am grateful to my parents, Mr. Rajkumar and Mrs. Jyotsna Khatri, and family for their love, understanding, and support, which provided me with strength and happiness during my ups and down. I am also thankful to my mother for teaching me how to cook, which has been of great assistance to me during these past few years. I am also in debt to my uncle, Dr. Vijay Chachada, for teaching me math and science all along during my high school years, which helped me create a strong basic foundation.

Last but not least, I express sincere thanks to my friends, whom enriched my social

stay at Caltech and made it memorable. Thanks to (to name few of them) Celia Reina Romo, Christopher Kovalchick, Francisco López Jiménez, Philipp Boettcher, Leslie Lambersson, Lydia Dennis, Wendy Li, Tomasz Tyranowski, Vikas Pandit Trivedi, Kishore Mac Jaganathan, Tejaswi Panji Venumadhav, Paraj Titum, Utkarsh Mital, Thevamaran Rajinikanth Ramathasan, Greg Kimball, Pia Ghosh, Leslie Wenning, Rory Perkins, Paula Popescu, Agustin Bompadre, Andrea Leonard, Ivan Szelengowicz, Paul Anzel, Annie Liu, Bao Ha, Jack Ziegler, Olive Stohlman, Kwok, Kawai, Michio Inoue, Artemis Ailianou, Wendy Mercer, Ajay Harish, Jeff Lehew, Harish Ravishankar, Harsha Bhat, Mike Mello, Angie Capece, Charles Kuan, Hemanth Siriki, Yacine Ali-Haïmoud, Nilanjan Roy, Puja Saluja, Sanjay Kumar, Manuj Swaroop, Neha Mathur, Himanshu Mishra, Prakhar Mehrotra, Nicholas Boechler, Eleftherios Terry Gdoutos, Jordan R. Raney, Wei-Hsun Lin, and Joseph Lydon.

Abstract

A chain of granular particles is one of the most studied examples of highly nonlinear systems deriving its response from the nonlinear Hertzian contact interaction between particles. Interest in these systems derives from their tunable dynamic response, encompassing linear, weakly nonlinear, and strongly nonlinear regimes, controlled by varying the static and dynamic load applied. In chains with a very weak (or zero) static precompression, the system supports the formation and propagation of highly nonlinear solitary waves (HNSWs). The dual-nonlinear interaction between particles (i.e., a power-law type contact potential in compression, and zero strength in tension) combined with discreteness of the system, makes the granular system highly tunable. The propagation properties of these waves, such as traveling pulse width, wave speed, number of separated pulses (single or train of pulses), etc., can be controlled by modifying one or many of the parameters, like the particle's dimension, material properties, static and dynamic force amplitude, the type and duration of the initial excitation applied to the system, and/or the periodicity of the chain. The ability to control the wave properties in such chains has been proposed for several different practical engineering applications.

The dynamic properties of these granular chains have been conventionally studied using discrete particle models (DPMs) which consider the particles in the chains as point masses connected by nonlinear Hertzian springs with the neighboring particles. Although, this is a good approximation under proper circumstances, it does not capture many features of the three dimensional elastic particles such as the elastic wave propagation within the particles, the local deformation of the particles in the vicinity of the contact point, the corresponding changes in the contact area, and the collective vibrations of the particles among others. This thesis focuses on the development of a finite element model (FEM)

using the commercially available software Abaqus, which takes into account many of these characteristic features. The finite element model discretizes particles by considering them as three-dimensional deformable bodies of revolution and describes the nonlinear dynamic response of one-dimensional granular chains composed of particles with various geometries and orientations. We showed that particles' geometries and orientations provide additional design parameters for controlling the dynamic response of the system, compared to chains composed of spherical particles. We also showed that the tunable and compact nature of these waves can be used to tailor the properties of HNSWs for specific application, such as information carriers for actuation and sensing of mechanical properties and boundary effects of adjoining media in Non-Destructive Evaluation (NDE) and Structural Health Monitoring (SHM). Using experiments and numerics, we characterized interface dynamics between granular media and adjoining linear elastic media, and found that the coupling produced temporary localization of the incident waves at the boundaries between the two media and their decomposition into reflected waves. We monitored the formation of reflected solitary waves propagating back from the interface and found that their properties are sensitive to the geometric and material properties of the adjoining media. The work done in this research enhances our understanding of the basic physics and tunability of nonlinear granular media, and further establishes a theoretical and numerical foundation in the applications of HNSWs as information carriers.

Contents

Dedication	iii
Acknowledgements	iv
Abstract	vii
Contents	ix
List of Figures	xii
List of Tables	xxvii
1 Introduction	1
1.1 Motivations and Goals	1
1.2 Outline of Thesis	5
1.3 Granular Particles	6
1.3.1 Hertz’s Law	7
1.4 Linear Waves in Discrete Media	9
1.5 Nonlinear Waves in a One-Dimensional Chain of Granular Particles	11
2 Experimental Setup	15
2.1 Granular Particles Used in Experiments	16
2.2 Instrumented Sensor Particles	16
2.3 Chain of Granular Particles	19
2.4 Coupling of Nonlinear Media with Linear Elastic Media–Cylindrical Rods	22
2.5 Coupling of Nonlinear Media with Linear Elastic Media–Plates	25

3	Numerical Modeling of a One-Dimensional Chain of Spherical Particles	28
3.1	Discrete Particle Model (DPM)	28
3.2	Finite Element Model (FEM)	30
3.2.1	Integration Schemes	31
3.2.2	Contact Model in Abaqus	32
3.2.3	Particles' Modeling	33
3.3	Numerical Validation	34
3.3.1	Quasi-Static Validation	34
3.3.2	Dynamic Validation	37
3.4	Mesh Convergence	41
3.5	Symmetric Boundary Condition on Beads	44
4	Dissipation in a One-Dimensional Chain of Spherical Particles	47
4.1	Introduction	47
4.2	Simulation	49
4.2.1	Discrete Empirical Model	49
4.2.2	Finite Element Model	52
4.3	Results and Discussion	53
5	Effect of Particle Geometry on the Dynamics of Granular Media	57
5.1	Particle Size	58
5.2	Particle Shape	58
5.2.1	Contact Interaction between Non-Spherical Particles	58
5.2.2	Wave Propagation in a Chain of Non-Spherical Particles with Elliptical Contact Interaction	62
5.3	Results and Discussions	64
5.3.1	Chain of Ellipsoidal Particles	64
5.3.2	Chain of Cylindrical Particles	69
5.3.3	Chain of Hollow Spherical Particles	77
6	Coupling of Nonlinear Media with Linear Media	83
6.1	Interaction of Highly Nonlinear Waves with an Adjacent One-Dimensional Linear Medium	85

6.1.1	Effects of the Linear Media's Stiffness	88
6.1.2	Effects of the Linear Media's Geometry	99
6.1.3	Effects of Double-Layer Media: Upper-Layer Thickness	102
6.1.4	Effects of Double-Layer Media: Lower-Layer Thickness	110
6.2	Interaction of Highly Nonlinear Waves with an Adjacent Two-Dimensional Thin Plate	113
6.2.1	Effect of Aspect Ratio	114
6.2.2	Effect of Plate Boundary	120
6.2.3	Discussion	124
6.3	Nonlinear Actuator Design	126
7	Conclusion and Future Work	128
	Bibliography	132

List of Figures

1.1	Schematic diagram of nonlinear granular chain as an automated impact actuator inside of a satellite. The reflected waves from the interface will be used to monitor the structure and to detect buried defects/impurities and other boundaries' conditions.	4
1.2	The figure shows two examples of granular particles. (a) Naturally occurring pebble particles. (b) Industrial-prepared calcium nitrate particles	6
1.3	Contact force between two particles	7
1.4	Schematic representation of discrete particle point mass system	10
1.5	Chain of spherical particles, with point contact between neighboring particles	11
2.1	The four different types of granular particles used in the course of this research to study wave propagation properties in granular media and their applications: (a) spherical particles, (b) ellipsoidal particles, (c) cylindrical particles, and (d) hollow sphere	17
2.2	Schematic diagram representing the assembly of the piezogauges embedded inside selected (a) spherical particles, (b) ellipsoidal particles, (c) cylindrical particles, and (d) hollow-spherical particles, respectively	19

2.3	Experimental setup for the vertically aligned, one-dimensional chain of spherical beads. Four supporting rods were used to constrain the motion of particles in one direction, along the axis of the chain. Instrumented particles, shown in the inset, were used at the selected location in the chain to extract the experimental data. These instrumented particles were fabricated using a piezoelectric sheet between the two cut halves of the beads. The instrumented particles were connected with Tektronix oscilloscopes, which recorded the signal information. An identical particle, similar to particles composing the chain, was used as striker for exciting a single pulse in the chain. The striker was released from a known height using a controlled-release mechanism	21
2.4	Experimental results showing the solitary wave propagation in the chain of 70 stainless steel 316 type particles, when the wave is excited using an identical striker particle with impact velocity = 1.77 m/s. The sensor particles in this case were placed at location numbers 9, 16, 24, 31, 40, 50, 56, and 63 in the chain	22
2.5	Experimental setup showing the one-dimensional, vertically aligned chain composed of 20 stainless steel spherical particles placed on top of a cylindrical sample. The bottom of the sample was under fixed boundary conditions using a V-block mount. The striker particle was control released from a known height using the solenoid	23
2.6	Various specimens used in the experimental study for interaction of granular media with adjacent linear elastic media. Single-layered uniform cylindrical specimen for variation of: (a) elastic modulus; and (b) geometrical length. Double-layered composite cylindrical specimen with stainless steel layer in the top and PTFE layer in the bottom for the variation: (c) inertia of upper layer H_{upper} and (d) stiffness of lower layer H_{lower}	24
2.7	A granular media composed of stainless steel spherical particles aligned vertically along the dotted central line of an aluminum plate	27
3.1	(a) FEM consisting of two hemi-spherical particles in contact. (b) FEM showing the one-dimensional chain of 21 spherical particles in contact with each other. The first particle on the right was used as striker particle	35

3.2	Quasi-static validation of our model. (a) Logarithmic fitting of the calculated contact force as a function of the applied displacement δ . The solid dots correspond to numerically obtained contact forces at given displacements, and the solid line is the linear fit. (b) Comparison of the force-displacement relation obtained from simulations (solid (black) curve), and the Hertz contact law (Eq. (1.1), dashed (blue) curve)	36
3.3	Dynamic validation of our model. Force profile of the solitary wave at particle number 10. The dash (blue) curve corresponds to the force obtained with our FEM averaging the forces measured at the contacts. The solid (red) curve corresponds to the force obtained with our FEM at the central section of particle 10. The solid (black) curve with star markers was obtained from the HNSW theory (Eq. (1.8))	37
3.4	Wave propagation detected at particles 10 (blue) and 15 (green) from the impacted end of the chain. (a) Experiments, (b) DPM, and (c) FEM results obtained with the contact force averaging method (first approach described above). The wave was generated with a striker having an impact velocity of 0.63 m/s.	39
3.5	Comparison of the variation of HNSW's velocity as a function of wave amplitude, obtained from FEM, DPM, and theory. The solid (black) curve represents the values obtained from theory (Eq. (1.10)). The solid (red) curve with square markers represent the results obtained from DPM, and the dashed (blue) curve with circular markers represent the results obtained from FEM.	40
3.6	FEM meshes for an individual particle in the two extreme cases tested: (a) a particle with the least refined mesh density, and (b) a particle with the most refined mesh density. The particles were discretized in space using tetrahedral elements of second order for all the FEM sets.	40
3.7	Comparison of the results obtained from (a) DPM, (b) FEM set with the least refined mesh, and (c) FEM set with the most refined mesh, for the HNSW traveling in a uniform chain of 20 stainless steel spherical particles excited by a striker, with an impact velocity of 0.5 m/s	42

3.8 (a) HNSW’s force amplitude obtained from FEM in increasing order of mesh refinement. The y-axis represents the maximum contact force (N) between particles at location number 15 and 16. (b) HNSW’s velocity obtained from FEM in increasing order of mesh refinement. The x-axis for both the figures represents the assembly sets used in increasing mesh density. The solid (black) curve is the force amplitude calculated from the DPM. The dotted (blue) markers and the dashed (blue) curve are the HNSW’s force amplitude and fitting calculated from the FEM. In both panels we observe that as the mesh was refined the force amplitudes and the wave speeds converge to the value calculated from the DPM. 43

3.9 Symmetric study of particle in the chain. For this study, we generated the three different types of particles, each having a symmetric property, and compared the solitary wave propagation results with the chain of full spherical particle. (a) Full three-dimensional spherical particle, (b) hemi-spherical particle having symmetric property along one plane, (c) quarter-spherical particle for model having symmetry in two different planes along transverse direction, (d) axis-symmetric two-dimensional spherical particle 44

3.10 Wave velocity study for four different models for the homogeneous chain of 20 particles. Each model has different symmetric condition in transverse direction. The y-axis and x-axis is force (N) and time (μs), respectively. (a) For the chain composed of full three-dimensional spherical particles. (b) For the model having symmetry loading and boundary property in one transverse plane, each particle was constructed using hemispherical and symmetric property in the respective plane. (c) For the model having two transverse plane symmetry, we used quarter spherical particles. (d) For the model having axis symmetric properties, we used two-dimensional axis symmetric particles for the chain. In the wave plots, the first solid curve (blue) and second curve (red) represent the force observed at the center of the 7th and 16th particle, respectively, in the chain. The third curve (red) and fourth curve (blue) are the reflected waves from rigid wall at particles number 16 and 7. 46

- 4.1 Optimization of the dissipation coefficients (α, γ) for a chain of 70 steel particles. (a) Difference $D(\alpha, \gamma)$, as defined in Eq. (4.2), between the force maxima observed in the experiment and our model. (b) Difference $\Delta_n(\alpha, \gamma)$, as defined in Eq. (4.3), in wave forms between the experiment and our model for a sensor placed at location $n = 56$. The solid and dashed curves in panel (a) correspond to the minima obtained from panels (a) and (b), respectively. 51
- 4.2 (a) Maximum force $F_m(n)$ for experiments with impact velocities v_3 (top curves) and v_8 (bottom curves, displaced by 5 units for clarity). The (red) circles with error bars correspond to the experiment, and the (green) thick curves give the numerical best fit (see the main text) with $(\alpha, \gamma) = (1.81 \pm 0.25, -5.58 \pm 1.30)$. The dashed curves correspond to the extreme cases using the standard deviation found in the optimal parameters. (b) Velocity of traveling front versus the maximum force (in a log-log plot). The solid curves represent the best linear fit, which gives $v \propto F_m^{0.17}$; we also show a dashed line with slope $1/6 \approx .167$ 54
- 4.3 (a) Decay of solitary wave in the chain of 70 stainless steel particles for striker velocity = 1.77 m/s. The sensor-particles were placed at location numbers 9, 16, 24, 31, 40, 50, 56, and 63 in the chain. The solid (blue) curves correspond to force values measured in experiments. The solid (blue) curve with circular markers, the solid (red) curve with triangular markers, and the dashed (black) curve with squared markers represent the maximum values obtained from the experimental data, the DPM (Carretero et al., 2009) and the FEM for the best dissipation parameter, respectively. (b) and (c) Force versus time profile in the chain at the sensors positioned in particles number (b) $n = 16$ and (c) $n = 56$. The solid (blue) curve shows the experimental data, the dashed (red) curve represents results obtained with the DPM (Carretero et al., 2009), and the dashed-dot (black) curve corresponds to the results obtained with the FEM for the best dissipation parameters. 56
- 5.1 Analytical results (Eq. (1.10)) showing the variation of wave velocity with the variation of dynamic loading, in the uniform chain of stainless steel 440C type spherical beads for four different sets of particle diameters $D = [2.38, 4.76, 9.53, 19.1]$ mm 58

5.2 Schematic diagram showing the front and side views for the contact between two ellipsoidal particles, and the dimensions and the radii of the maximum and minimum principal of curvatures at the contact points between ellipsoidal particles 59

5.3 (a) Finite element mesh of: (i) two adjacent ellipsoidal particles arranged in the minor axis direction; (ii) two adjacent ellipsoidal particles arranged in the major axis direction; and (iii) two adjacent equivalent spherical particles. (b) Comparison of the contact force-displacement relations between two ellipsoidal particles arranged in minor (curve group (i)) and major (curve group(ii)) axis direction, and also between two equivalent spherical particles (curve group (iii)) obtained from both finite element simulations (dotted (blue) curves) and Hertzian elliptical contact law (solid (black) curves) . . . 65

5.4 Finite element model showing the zoom-in view of a uniform chain of ellipsoidal particles, with the particles aligned along their (b) major axis and (c) minor axis, respectively 67

5.5 (a) Comparison of experiments and numerical results on the formation and propagation of a solitary wave in a chain of 20 stainless steel ellipsoidal particles excited by impacting a stainless steel spherical striker of mass $m = 0.925\text{ g}$ with an initial velocity of 0.626 m/s. Curve group 1 shows the results for particle 7 in the chain from the top, and similarly, curve group 2 shows the results for particle 12 from the top. Experimental results are shown by solid (green) curves. (b) Dependence of the wave speed on the maximum contact dynamic force in the chains of ellipsoidal particles arranged in both minor (curve group (i)) and major (curve group (ii)) axis directions and in the chain of equivalent spherical particles (curve group (iii)) under gravitational loading. Experimental data for a chain of ellipsoidal particles arranged in minor axis direction are shown by solid (green) diamonds in curve group (iii). The solid (black) curves represent the theoretical predictions. In both panels the dashed (red) curves represent the discrete particle results and the dotted (blue) curves represent the finite element results. 68

5.6	Results obtained in a chain composed of 50 ellipsoidal particles, excited by a spherical striker with an impact velocity $v = 0.37$ m/s. The (green) solid curves represent experimental force-time signals obtained from instrumented particles positioned in locations 8, 16, 28, and 41. The (red) dashed curves represent numerical results obtained from a modified discrete particle model with linear damping. γ was the relaxation coefficient and has a value of -11.67	69
5.7	(a) Schematic diagram showing isometric view and (b) top view of two cylindrical particles in contact. (c) Comparison of the contact force-displacement relations obtained with the Hertzian contact model (solid curves), and with our finite element model (dashed curves). Results obtained for a contact between two cylindrical particles oriented at a relative angle $\alpha = 0^\circ$ (curve group (i)), $\alpha = 5^\circ$ (curve group (ii)), $\alpha = 10^\circ$ (curve group (iii)), $\alpha = 30^\circ$ (curve group (iv)), and $\alpha = 90^\circ$ (curve group (v)). (d) Detailed view of (c) for $\alpha = 5^\circ, 10^\circ, 30^\circ$, and 90° . (e) Dependence of the exponent n in a generic power-law type contact interaction between two cylindrical particles on the orientation angle α , obtained through finite element analysis	71
5.8	Schematic diagram of the cylindrical particles' chain. The chain was composed of 20 elements, stacked vertically. Piezoelectric sensors were embedded in particles at location numbers 7 and 13. The orientation angle α between two adjacent particles in the setup shown is (a) 30° and (b) 90° , respectively.	73

5.9 (a) Comparison of experimental and numerical results, obtained from the finite element and discrete particle models, for the wave propagation in a chain of cylindrical particles with orientation angle $\alpha = 90^\circ$. The results obtained from the instrumented particles placed at location numbers 7 and 13 from the top of the chain are represented by curve groups (1) and (2), respectively. The solid (green) curves represent experimental data. The dashed (red) curves are obtained from our discrete particle model, and the dotted (blue) curves from FEM. (b) Dependence of solitary wave speed on the maximum dynamic contact force in the chain of cylindrical particles when $\alpha = 30^\circ$ (curve group (i)), when $\alpha = 45^\circ$ (curve group (ii)), and when $\alpha = 90^\circ$ (curve group (iii)). Experimental data are reported only for $\alpha = 90^\circ$, and are shown by solid (green) squares. The theoretical results for all of the angles in each group are shown by solid (black) curves. The results obtained with our discrete particle model are represented by the dashed (red) curve, and the finite element results are represented by the dotted (blue) curves in each group. 75

5.10 Numerical results showing the dynamic response of a chain composed of parallel cylinders ($\alpha = 0^\circ$). (a) Force profiles in time obtained for a wave traveling in a chain of parallel particles using our finite element model (dotted (blue) curves) and our discrete particle model (dashed (red) curves). Curve groups (1) and (2) represent results obtained for the waves traveling through the 7th and 13th particles from the top of the chain. (b) Dependence of wave speed on the maximum dynamic contact force. The solid lines represent results obtained with our FEM for different values of the relative orientation angle $\alpha = [0^\circ, 1^\circ, 3^\circ, 5^\circ, 30^\circ, 45^\circ, 90^\circ]$. The dotted line, shown for $\alpha = 0^\circ$, reports data obtained with the DPM. 76

5.11 FEM results showing the dependence of the wave speed (normalized with respect to the wave speed in the case $\alpha = 90^\circ$) as a function of the orientation angle α . The three curves correspond to three different dynamic force values: the solid (blue) curve with circular markers is for $F_m = 80$ N; the dashed (red) curve with diamond markers corresponds to $F_m = 40$ N; and the dotted (black) curve with triangular markers is for $F_m = 10$ N. 77

5.12 a) Schematic diagram showing the axial symmetric FEM of two hollow spheres in contact with symmetry and boundary conditions. (b) Contact interactions obtained from FE simulations for selected values of $R_i/R_o = 0$ (curve (i) in black), $= 0.5$ (curve (ii) in green), $= 0.75$ (curve (iii) in red), $= 0.91$ (curve (iv) in blue). The markers represent the FE results, the dashed curves are the power law fittings of the FE results. The solid black curve is obtained from the Hertzian contact interaction between two solid spheres of the same radius R_o 78

5.13 Schematic diagram of the chain composed of 20 hollow spherical particles, with piezoelectric sensors embedded in particles at location numbers 7 and 13. The radius ratios R_i/R_o for the chain considered were (a) 0, (b) 0.5, (c) 0.75, and (d) 0.908, respectively. 79

- 5.14 (a) Comparison of experimental and numerical results, obtained from discrete particle and FE simulations, for the wave propagation in a chain of hollow spheres with $R_i/R_o = 0.91$. The curve group (1) in blue represents the results obtained at particle 12, the curve group (2) in red represents the results obtained at particle 19. The solid curves represent experimental data. The dashed curves are obtained from FE simulations, and the dotted curves from DP simulations. (b) Dependence of solitary wave speed on the dynamic force amplitude in the chain of hollow spheres when $R_i/R_o = 0$ (curve group (i) in black), when $R_i/R_o = 0.5$ (curve group (ii) in green), when $R_i/R_o = 0.75$ (curve group (iii) in red), when $R_i/R_o = 0.91$ (curve group (iv) in blue). Experimental data are reported only for $R_i/R_o = 0.91$, and they are shown by solid diamonds. The theoretical results in each group are represented by solid curves. The results obtained with our discrete particle model are represented by dashed curves and the finite elements results are represented by circles. (c) Comparison of logarithmic scaling of wave velocity-force relation for the chain of hollow spherical particles, $R_i/R_o = 0.908$, with the chain of solid spherical particles, $R_i/R_o = 0.0$ 81
- 6.1 Finite element model for coupling of one-dimensional chain composed of 20 spherical particles with adjacent linear elastic media: (a) a uniform single-layer linear elastic media; and (b) a composite double-layer linear elastic media. The bottom of the linear media was under fixed boundary conditions 85
- 6.2 Solitary wave propagation measured from the 7th bead in the chain against (a) stainless steel wall and (b) PTFE wall. In (b) the arrival of the primary reflected wave (PSW) is significantly delayed and the generation of a secondary solitary wave (SSW) is clearly observed. The delay time between the incident and the reflected waves is represented by the time of flight (TOF), which is the transit time between the incident and the reflected solitary waves. 89

6.3 Numerical results showing the displacement profiles in the granular chain including the striker bead (first curve on the left) and 20 particles composing the chain. The displacement of the beads is increased under the incidence of the solitary wave. After interacting with the interface, the beads tend to return to their original positions with additional small oscillations, which are particularly evident in the case of wave interaction with the PTFE cylinder. The displacement profile of the 7th particle (thicker solid blue line indicated by y_7) shows distinct portions of solitary wave travelling time (T_t) and contact time (T_c) between stainless steel and PTFE media. (a) The stainless steel wall induces small displacement ($4.39\mu\text{m}$) and short contact time ($85\mu\text{s}$) of the last bead against the bounding wall (bold red line). (b) The PTFE wall allows for a larger displacement of the last bead ($16.66\mu\text{m}$) and as a result, a longer contact time ($241\mu\text{s}$) spent on rebounding. We observe multiple impacts between the last and its neighboring beads. The first and second collisions occur at $450\mu\text{s}$ and $561\mu\text{s}$ points, as marked by circle and square, respectively 96

6.4 Comparison of experimental, theoretical, and numerical data for the time of flight (TOF) of the primary and secondary reflected solitary waves in the chain of spheres as a function of Young’s modulus of the neighboring media. (a) Arrival time of the PSW in the instrumented particle (7th from top) as obtained by theoretical models (solid red line), discrete numerical calculations (dashed blue line), and experiments. (b) Arrival time of the SSW, in similar trend to the one of the PSW with an approximately 0.1 ms delay. 98

6.5 Surface plot obtained from numerical simulations showing the formation of primary and secondary solitary waves in the time domain. The y-axis reports a set of different values of elastic moduli of the linear media adjacent to the chain of spheres. As the stiffness of the contact is decreased, the TOF of the reflected wave increases. Here, the first vertical line evident at ~ 120 ms from the impact (Time = 0) represents the arrival of the incoming solitary wave. The generation of a reflected SSW is noticeable after a critical value of elastic modulus of the contact. These simulation results were based on the force profile measured from the 7th bead in the chain, and the color bar on the right denotes the amplitude of the force profiles in N. 99

- 6.6 Comparison of experimental, theoretical, and numerical data for the amplitude ratio of the primary and secondary reflected solitary waves in the chain of spheres as a function of Young's modulus of the neighboring media. (a) Arrival time of the PSW (b) Reflection ratio of the amplitude of the PSW over that of the incident solitary wave in the instrumented particle (7th from top) as obtained by theoretical models (solid red line), discrete numerical calculations (dashed blue line), and experiments.. (c) Arrival time of the SSW, in similar trend to the one of the PSW with an approximately 0.1 ms delay. (d) Reflection ratio of the amplitude of the SSW over the amplitude of the incident solitary wave. The reflection ratio becomes smaller as the elastic modulus increases. 100
- 6.7 Surface plots showing the incident and the reflected solitary waves propagating in the time domain. The y-axis shows the different heights of the stainless steel cylinders. The first band visible on the left represents the incoming solitary waves, while the band on the right shows the reflected solitary waves (PSWs) arriving in the instrumented sensor after 0.53 ms. No secondary solitary wave is observed. Numerical results were obtained by testing 14 slender cylinder samples with different heights. The formation of the PSWs shows no sensitivity to the cylinder heights. 101
- 6.8 Time of flight and reflection ratio of the PSW reflected from the stainless steel slender cylinders as a function of the cylinders' heights. Numerical and experimental data are compared in the magnified Y-axis scale. (a) Arrival time of the PSW, with an extremely regular distribution of the experimental data in the range of 0.44 ~ 0.45 ms (less than 1% error). (b) Amplitude ratio of the PSWs. Numerical results show a minute drop from 0.764 to 0.734 around the characteristic length of the linear medium ($L = 101$ mm), which is within the range of the error bars from the experimental results. 103
- 6.9 Surface plots of incident and backscattered solitary waves as a function of upper layer's height (L_u) in the composite linear media. The primary solitary wave was observed at ~ 0.6 ms, whereas the secondary solitary waves exhibit scattered arrival time in the time domain. Experimental results show the dominance of the PSW at large L_u and the emergence of the SSWs at small L_u . The surface plots are based on the force profile measured from the 7th bead in the chain, and the color bar on the right denotes the amplitude of the force profiles in newtons. 106

6.10	Comparison of experimental, theoretical, and numerical data for the time of arrival on the instrumented particle (TOF) of the primary and secondary reflected solitary waves in the chain of spheres, as a function of the upper-layer thickness (L_u) in the composite media. (a) Time of flight for the PSWs. The arrival time is within the 0.43 to 0.47 ms range. (b) Time of flight for the SSWs. Compared to that of the PSWs, the progression is in the opposite direction with improved responsiveness.	108
6.11	Comparison of experimental, theoretical, and numerical data for the amplitude ratio of the primary and secondary reflected solitary waves in the chain of spheres, as a function of the upper-layer thickness (L_u) in the composite media. (a) Amplitude ratio for the PSWs. The amplitude reflection ratio increases as L_u grows. (b) Amplitude ratio of the SSWs. In contrast to PSW reflection in (a), larger L_u yields the smaller SSW reflection in compensation for the increased PSW reflection. For the upper layer taller than ~ 22 mm, the magnitude of the reflection ratio drops below 10%	109
6.12	Numerical results showing the surface plots of incident and reflected solitary waves in granular chain as a function of lower-layer dimension of the composite linear media. The formation of the primary reflected solitary wave is insensitive to the lower-layer thickness, showing the constant amplitude and arrival time for all lower-layer thicknesses tested. However, the secondary solitary waves reveal significant delay in their formation as the dimension of the lower layer increases	110
6.13	Comparison of experimental, theoretical, and numerical data for the time of arrival on the instrumented particle (TOF) of the primary and secondary reflected solitary waves in the chain of spheres, as a function of the lower layer thickness (L_l) in the composite media. (a) Time of flight for the PSWs. (b) Time of flight for the SSWs.	111
6.14	Comparison of experimental, theoretical, and numerical data for the amplitude ratio of the primary and secondary reflected solitary waves in the chain of spheres, as a function of the lower layer thickness (L_l) in the composite media. (a) Amplitude ratio for the PSWs. The amplitude reflection ratio increases as L_l grows. (b) Amplitude ratio of the SSWs.	112

6.15 FEM showing a uniform one-dimensional vertically aligned chain of 21 spherical particles ($D = 9.52$ mm) placed on top of a horizontal thin plate ($t = 2.28$ mm). Two of the plate edges in one direction were applied with fixed boundary condition, and the other two edges in other direction were free. The wave in the chain is excited using the first particle as striker. 114

6.16 Force profiles obtained from experiments for solitary wave propagation in the granular media ($D = 9.52$ mm) under the interaction with two different plates. (a) Force profiles for a thin plate ($t = 2.28$ mm). (b) Force profiles for a thick plate ($t = 9.52$ mm). The reflected solitary waves against the thick plate exhibit stronger (larger F_{ref}) and faster (smaller TOF) compared to the thin plate case. 115

6.17 Plot showing theoretical value of dimensionless contact time (τ_c) as a function of inelasticity parameter (λ). The dimensionless contact time approaches $\tau_{c,0} = 3.218$ for the value corresponding to $\lambda = 0$, which is the case of elastic impact of spherical particle against a semi-infinite elastic media. 118

6.18 Amplitude ratio of reflected solitary waves (AR) as a function of the ratio of the sphere diameter to the plate thickness (D/t). The solid black line represents the analytical results, while the filled and hollow marks denote the finite element model and experimental results, respectively. 119

6.19 (a) Time of flight (TOF) as a function of D/t . (b) Normalized TOF with respect to D as a function of D/t . After normalization, three different curves in (a) overlap into a single curve in (b). The solid black line represents the analytical results, while the filled and hollow marks denote the finite element model and experimental results, respectively. 119

6.20 Amplitude ratio of reflected solitary waves (ARR) as a function of distance from the support. (a) Granular crystal with small spheres ($D = 9.53$ mm). (b) Granular media with large spheres ($D = 19.1$ mm). The filled and hollow marks denote the finite element model and experimental results, respectively. 122

6.21 Critical distances (L_c) in various thicknesses (t) of plates and the diameters (D) of granular medias. Solid and dashed black lines denote the analytical predictions based on the propagation of guided waves with velocity parameter $k = 0.5$ and 0.2 (i.e., $c = 2,900$ and $1,000$ m/s), during the contact time $T_{c,0}$. The experimental and FEM results are represented by the hollow and filled marks, respectively. 123

6.22 Fully automated nonlinear actuator (a) schematic and (b) model 126

List of Tables

2.1	Material properties of different types of particles and specimens used in the experiments. The reported values are standard specifications (Efun da Inc., 2011) except Young’s moduli of polymers, which were extrapolated from Hugoniot relationship (Carter and Marsh, 1995).	18
4.1	Material properties (mass m , elastic modulus E , and Poisson ratio ν) for stainless steel, PTFE, and brass. The last two columns present our best estimates, together with their standard deviation, of the dissipation coefficients (α, γ).	54
5.1	The values of the contact stiffness k and the exponent n obtained from FE simulations for selected values of R_i/R_o	80

Chapter 1

Introduction

1.1 Motivations and Goals

In recent years, chains of granular particles have received a considerable amount of attention because of their nonlinear dynamic responses derived from the nonlinear contact interaction between adjacent particles (Brunhuber et al., 2006; Chatterjee, 1999; Coste et al., 1997; Daraio et al., 2006b; Doney and Sen, 2006; Harbola et al., 2009; Herbold and Nesterenko, 2007; Herbold et al., 2006; Hong, 2005; Job et al., 2009; Nesterenko, 1983 2001; Remoissenet, 1999; Rosas et al., 2007; Sen and Manciu, 1999; Sen et al., 2008; Vergara, 2006). It has been demonstrated that HNSWs are sensitive to granular materials' properties (Coste et al., 1997; Nesterenko, 2001), such as the elastic modulus, the density and the Poisson ratio of the particles. Coste et al. (1997), Daraio et al. (2005 2006b), and Daraio and Nesterenko (2006) studied numerically and experimentally the propagation of HNSWs in various uniform one-dimensional chains composed of particles of different materials: for example, stainless-steel, glass, brass, nylon, polytetrafluoroethylene (PTFE), and even in Parylene-coated steel particles. As predicted by theoretical formulations and verified through numerics and experiments, the wave properties in these chains depend significantly on the material parameters of granular particles composing the chain. It has also been shown numerically and experimentally that the properties of HNSW can be further varied and tuned easily: for example the wave speed can be altered over a wide range by controlling the static preload applied on the granular chains (Coste et al., 1997;

Daraio et al., 2006b; Nesterenko, 2001) or by controlling the wave amplitude (Daraio and Nesterenko, 2006; Daraio et al., 2005 2006b). The addition of periodic heterogeneities in the chain can also be used to tailor wave properties in the chain, such as, wave speed, wave amplitude, and wave width, can be changed accordingly (Porter et al., 2008 2009).

By tuning the various system parameters, the properties of the HNSWs can be controlled and designed for specific applications. Sen et al. (1998) and Hong and Xu (2002) showed the possibility of using the nonlinear solitary waves for the detection of defects and impurities in granular media. Hong and Xu (2002) showed that the backscattered signal's velocity and shape depend on the presence of light and heavy impurities in granular chains. Nesterenko et al. (2005) and Vergara (2005 2006) studied wave reflection and scattering from the interface of two granular media and found that the energy can be trapped and back-scattered from the interface depending on the interface properties. Job et al. (2005) studied experimentally and numerically the interaction of nonlinear media with a wall of different mechanical properties and found that the reflected waves from the interface depend on the wall's mechanical properties. Daraio et al. (2006a) and Vergara (2006) showed the potential usefulness of these systems in energy trapping and shock disintegration works. Besides these, some of the other areas of potential application in which highly nonlinear solitary waves can be useful are sound focusing devices (tunable acoustic lenses and delay lines), sound absorption layers, and sound scramblers (Daraio et al., 2005; Herbold et al., 2006; Nesterenko et al., 2005; Spadoni and Daraio, 2010).

The ability of the HNSWs to carry the information and their self-stabilization motivated us to study the dynamic response of chains composed of nonspherical particles, where the particles' geometries and orientations can provide us with additional design parameters and, along with particles' material properties, the facility to tune them for specific wave properties – which makes them a very attractive tool for several applications. The scalable and controllable nature of nonlinear granular media, an understanding of the wave reflection and transmission problems from various interfaces, their ability to carry information, and their minimal dependence on power requirements (as compared to function generators in ultrasonic actuation systems) combine to provide an alternative to classical instrumented hammers in impact testing as a nonlinear actuator/sensor system

in nondestructive evaluation/structural health monitoring (NDE/SHM) applications for determining material properties and geometry effects of structures. Figure 1.1 shows a schematic of a futuristic nonlinear granular actuator system which can be used in a shuttle with wireless technology as pitch-echo to test linear/non-linear structures.

To use the granular system for NDE/SHM application and many future possible applications, we need to understand the interface dynamics between nonlinear granular media and adjacent linear elastic media. It is also imperative to understand the wave propagation and energy losses in the granular chains for defining specific expected wave characteristics in physical practical applications. We also need numerical technique, which should be able to couple nonlinear granular chains with specimens of any nature (linear elastic media or nonlinear inelastic/granular media).

The dynamic properties of granular chains have been conventionally studied using discrete particle models (DPMs), which consider the particles in the chains as point masses connected by nonlinear Hertzian springs with the neighboring particles. Although this is a good approximation under proper circumstances, it doesn't capture many features of the three-dimensional elastic particles, such as the elastic wave propagation within the particles, the local deformation of the particles in the vicinity of the contact point, the corresponding changes of the contact area, and the collective vibrations of the particles, among others. Therefore, the goal of this research is to develop a finite element model, using commercially available software Abaqus, which is capable of taking into account many of these characteristic features. The finite element model developed in this work will be able to discretize particles by considering them as three-dimensional deformable bodies of revolution. The model will also be helpful in understanding the interaction behavior between nonspherical particles, and its dependence on particles' geometry and orientation. It will also be useful in studying the interface dynamics of granular chains and adjacent linear elastic media, which can be a viable and useful tool in the future to numerically study the NDE/SHM of complicated structures using granular chains as an actuator/sensing device.

For practical applications, we will also study dissipative losses in uniform granular chains of different particles' material values. In this work, we will also incorporate these losses

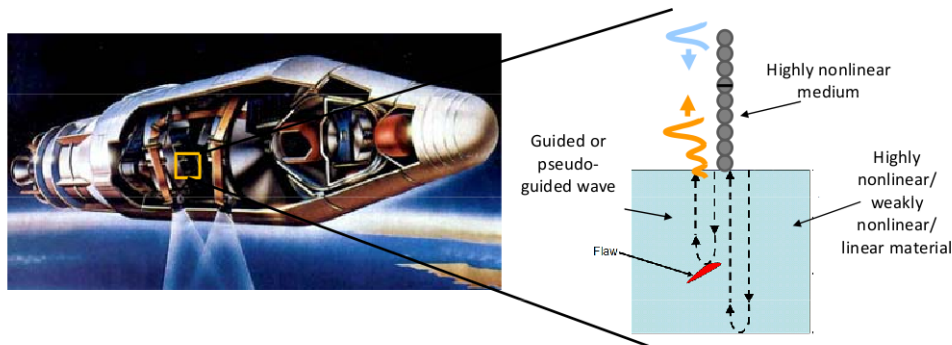


Figure 1.1: Schematic diagram of nonlinear granular chain as an automated impact actuator inside of a satellite. The reflected waves from the interface will be used to monitor the structure and to detect buried defects/impurities and other boundaries' conditions.

in our finite element model using linear Rayleigh damping parameters. For cases under certain circumstances where we can use DPM, which can be helpful in quick results, especially under one-dimensional assumptions, the goal will be to develop an analytical model with dissipative terms included, such that it should be capable of predicting, quantitatively and qualitatively, the dissipative HNSW's propagation in granular chains. As mentioned above, to understand and extend the tuning nature of HNSWs, the work will be to study the uniform chain of nonspherical particles. We used nonspherical particles, namely ellipsoidal and cylindrical particles, to study the effect of particles' geometry and orientation on the contact interaction, and also on wave dynamics in the system, as compared to the chain of spherical particles. We verified the change in the wave characteristic for non-spherical particles through experiments.

We systematically investigated the wave localization at the interface of nonlinear granular media with the linear elastic media by using cylindrical specimens of different materials and geometry as adjacent wall medium to granular chain. From a practical-application point of view, we also studied the layered cylinder as a simplistic assumption to composite media, as well as large thin plates of different thickness and boundary conditions. The results obtained from this interaction study show that the information carried by the reflected waves from the interface is sensitive to the bounding media. We found that the magnitude of the reflected waves decreases with the decrease in the aspect ratio. We also found that there exists a critical distance from the plate boundary, after which the response of reflected waves in granular chain from the interface was independent of

distance between impact point and plate boundary. In many physical applications, such as airplanes' wings, cars, ships, etc., the body is made of plate/composite-like structures, which was the motivation to study thin plate-like structures.

1.2 Outline of Thesis

In this chapter, we provide a basic review of granular particles' contact theory, wave propagation in discrete particle system, and highly nonlinear wave dynamics in discrete Hertzian chains.

Chapter 2 describes the experimental setup used during the course of this research. Chapter 3 describes the finite element model developed to simulate the dynamics of a chain of granular particles as three-dimensional deformable bodies. We also compared our FEM results with experiments and the traditional discrete particle simulations and found a good agreement between them. Chapter 4 discusses the effects of dissipation in the HNSW's propagation in the chain of granular particles, the analytical model and the finite element model, all developed to incorporate the energy losses during wave propagation. The study of dissipation in granular chains is helpful for using a nonlinear actuator in practical applications. In Chapter 5, using FEM, we study contact interaction between particles of various geometries. We use this interaction law to analytically and numerically test the dynamics of chains composed of nonspherical particles. We also verify these effects using experiments and find very good agreement.

In Chapter 6, we experimentally and numerically study the coupling of nonlinear media with linear elastic media, such as cylindrical rods and thin plates. From this study, we learn that the interface dynamics are sensitive to the adjacent media, which leads to the formation of multiple reflected HNSWs in granular chains. The nature and number of these multiple reflected HNSWs depend on the coupling between the two media.

1.3 Granular Particles

By granular material, we refer to an aggregate of discrete macroscopic particles, the sizes of which are comparable to the size of the total system, and usually large enough that the thermal motion fluctuations can be neglected. Many researches, including [de Coulomb \(1776\)](#), [Faraday \(1831\)](#), and [Reynolds \(1885\)](#) studied various properties of granular particles and provided helpful information in the early development of this field. [Richard et al. \(2005\)](#), a material scientist, mentioned in his paper that granular materials are ubiquitous in nature and are the second most manipulated material in industry (the first being water). These particles can be found easily in nature and in many industrial applications. For example, sand and raw materials (grain, ore, and sugar) represent the basic form of granular particles found in nature. Powders, such as calcium propionate (calcium salt), a white particle-line solid, are widely used as preservatives for a wide range of baked goods in industry. Soda ash powder is another form of granular particle used widely in chemical industries, such as glass and paper manufacturing, among several others. Bearings, another form of simple yet important granular particle, can also be found in many mechanical machines, cars, bicycles, motors, aircraft, etc. Figure 1.2 shows an example of natural and industrial granular particles.

The importance and uniqueness of these granular particles stem from the understanding that they behave differently than the standard states of matter, i.e., solid, liquid, and gas ([Duran, 2000](#)). Conventional liquid and gas follow Brownian motion during mixing



Figure 1.2: The figure shows two examples of granular particles. (a) Naturally occurring pebble particles. (b) Industrial-prepared calcium nitrate particles

process, whereas the granular particles behave differently and the process typically results in segregation. When the granular particles are non-cohesive, the repulsive component is the dominant interaction force between them, because of which the effective particle shape also depends on external boundaries, gravity, and other parameters. On the other hand, when the granular particle surface is non-adhesive, for several static and dynamic conditions the interstitial fluid present can be neglected.

1.3.1 Hertz's Law

In our study, we used granular particles of non-conforming geometrical shapes and primarily influenced by Hertz contact law interaction (Hertz, 1882). When two of these particles approach each other under no external loading, the initial contact made between their surfaces is the point of contact (or possibly a line contact). Hertz (1882) published the first paper “Contact between solid elastic bodies,” describing the local elastic deformation relation between two spherical particles. Since then, Hertz's law has been used extensively in various fields of contact mechanics, such as for wheel-rail contact, metal forming, gasket seals, etc.

Hertz considered two identical spherical particles of radius R with the assumption that both of the particles are topographically smooth on macro and micro scales, so that the

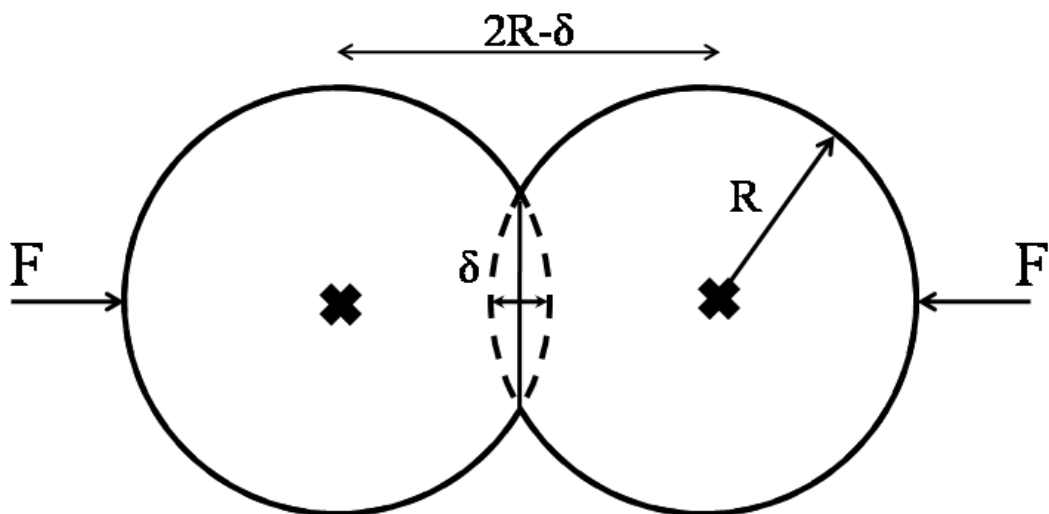


Figure 1.3: Contact force between two particles

elastic wave's motion in the particle can be neglected, and that the tangential surface interaction between the particles is frictionless. Figure 1.3 shows the schematic of two particles in contact under compressive force F . When these particles are pressed against each other towards the contact point O , with the relative approach between the distant points of two particles as $\delta = \delta_1 + \delta_2$, where δ_1, δ_2 represents the displacement of distant point for particles 1 and 2, respectively, such that $\delta > 0$ for compression and $\delta < 0$ for tension, the particles deform locally at the point of contact O and form a circular contact area. Due to the material's nature to return to its original shape, a repelling force is developed between the two particles. It is assumed that the radii of curvatures of the contacting particles are large as compared to the radius of contact circle, which results in small deformation and, combined with stiff materials, the problem is considered as linear elastic. The problem is also considered as elasto-static, i.e., the material interaction is linear elastic and the two particles are in static equilibrium such that the displacement δ is independent of time. With these assumptions, the interaction force derived by Hertz for two spherical particles is (Hertz, 1882; Johnson, 1987)

$$F(\delta) = \begin{cases} k\delta^{3/2} & \text{if } \delta > 0 \\ 0 & \text{if } \delta < 0 \end{cases} \quad (1.1)$$

where $k = \frac{2E}{3(1-\nu^2)} \sqrt{\frac{R_1 R_2}{R_1 + R_2}}$ is the spring constant between the particles during compression. R_1 and R_2 are the radii of the particles, and E and ν are Young's modulus and Poisson's ratio, respectively, for the particle's material. F , the compressive force between the particles, is considered positive in compression ($\delta > 0$) and zero in tension ($\delta < 0$). During the compression process, the force is initially weak as compared to linear or harmonic spring force for small values of δ , and it rises sharply when the δ value is increased as compared to linear spring force. This is because the interaction force in the Hertz model is proportional to the $\delta^{3/2}$, a complete nonlinear contact interaction behavior between two spherical particles which results from the geometrical effects only, and the proportionality relation depends on the contact geometry of the two particles. A detailed generalization of the Hertz contact law was developed by Spence (1968), which describes the interaction of two particles of arbitrary axisymmetric contact surface. Spence calculated the stress distribution and the contact area of overlap between the two particles to determine the

interaction force between the particles. For a more specific case, when the interacting particles are cube or conical shaped, the interaction force is proportional to δ and δ^2 , respectively (Fu, 2007). Thus, using particles of different geometry, the contact interaction relation can be modified for a specific response.

1.4 Linear Waves in Discrete Media

Wave propagation in discrete particle media has been a topic of study for a long time. The classical book titled *Wave Propagation in Periodic Structures* by Brillouin (1946) covers the detailed review of waves in periodic structures. Newton (1729) first worked on one-dimensional lattice while he was trying to derive a formula for the velocity of sound in air. In his work, he considered the simple case of a one-dimensional lattice system as an equally spaced point mass (m) system connected to the neighboring points, with elastic spring constant C placed uniformly at d distance apart (Figure 1.4). The particle at the location s is affected by the displacement of the particle at location $s + p$, such that the force on the particle at location s is proportional to the relative displacements of the two particles $u_{s+p} - u_s$. For simplicity, only the first-order approximation up to the interaction of nearest-neighbor point is considered, i.e., $s \pm 1$. Using this approach, Newton derived the force experienced by the particle at location s as

$$F = U'(u_{s+1} - u_s) - U'(u_s - u_{s-1}) \quad (1.2)$$

where U is the interaction potential and F is the force experienced by the particle at location s . Using this relationship, the theoretical elastic wave velocity obtained by Newton was $V = d\sqrt{C/m}$ in the air. Although, the theoretical wave speed calculated from this formula was lower than the experimental values, because sound waves in the air propagate under the adiabatic process, which was pointed out by Laplace in 1822, the wave velocity from Newton's formula under adiabatic assumptions is in excellent agreement with the experiments.

In the year 1727, John Bernoulli and his son, Daniel Bernoulli, showed that the system

with N point masses has exactly N independent modes of vibration. Due to the discreteness of the system, the infinitesimal waves of arbitrary spatial frequencies cannot propagate, and therefore there is a corresponding upper bound on the temporal frequencies that the chain can support. This property allows nonlinear oscillations to avoid resonances with small-amplitude waves, and localized oscillations can persist without radiating energy. Later in 1753, Daniel Bernoulli proved the principle of superposition of normal modes in a discrete point mass system, which is a special case of Fourier series. In the nineteenth century, several researchers including Cauchy, Baden-Powell, Kelvin, Einstein, and von Karman adopted Newton's model to study various optical wave phenomenon, such as dispersion, cutoff frequency, mechanical filter, etc. In their model, they assumed that the coordinate of the particle at the location s can be written as

$$u_s = sd + \psi_s \quad (1.3)$$

where ψ_s is the displacement of the particle at s from its equilibrium position. Assuming harmonic traveling waves in the discrete system, $\psi_s = Ae^{i(\omega t - ks)}$, where ω , k , and A are the wave frequency, wave number, and wave amplitude, respectively. The wave equation has the solution given by

$$\omega^2 \cong \frac{4C}{m} \sin^2 \left(\frac{1}{2}ka \right). \quad (1.4)$$

Thus, a periodic discrete particle system supports only the unique solutions, which are periodic in k , with the limitation that the shortest wave length is twice the distance d between particles, and therefore the system has a natural critical, or cutoff, characteristic frequency.



Figure 1.4: Schematic representation of discrete particle point mass system

1.5 Nonlinear Waves in a One-Dimensional Chain of Granular Particles

Nesterenko (1983) considered a one-dimensional chain composed of spherical granular particles, governed by Hertz's contact interaction Equation (1.1) between neighboring particles (Figure 1.5) and discovered the formation and propagation of highly nonlinear solitary waves in the chain. A system of equation describing the motion of each particle in a one-dimensional chain of identical particles, where the spring constant is given by Eq. (1.1), is

$$\ddot{u}_s = A(\delta_0 - u_s + u_{s-1})^{3/2} - A(\delta_0 - u_{s+1} + u_s)^{3/2} \quad (1.5)$$

where u is the displacement of the particle at location s from its static displacement because of the imposed force, and $A = k/m = \frac{E\sqrt{2R}}{3m(1-\nu^2)}$ is a factor based on the particle's properties. Equation (1.5) is an example of a Fermi-Pasta-Ulam (FPU) (Fermi et al., 1965) system, which is an important class of system of coupled oscillators. These systems have been extensively studied in nonlinear science for their intriguing wave propagation behavior and connections to solitons. Nesterenko considered the chain under an initial static compressive force F_0 , which leads to an initial overlap of δ_0 between any two particles. This equation supports two different dynamic wave propagation regimes based on initial strain of the system (Nesterenko, 2001). In the first regime, when the chain is under a large static compressive load (large with respect to the amplitude of the dynamic excitations $F_{static} \gg F_{dynamic}$), which results in $\frac{|u_{s+1} - u_s|}{\delta_0} \ll 1$, the system acts as a linear or weakly nonlinear wave medium. In the long wavelength anharmonic approximations, Eq. (1.5) can be simplified into the nonlinear Korteweg-de Vries equation (Korteweg and Vries, 1895).

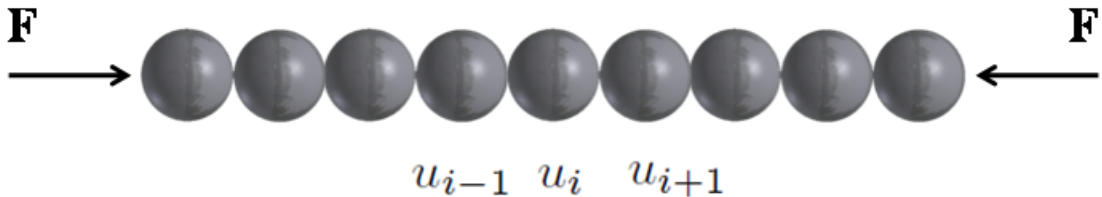


Figure 1.5: Chain of spherical particles, with point contact between neighboring particles

In the second regime, when the chain is uncompressed or very weakly precompressed ($F_{static} \lesssim F_{dynamic}$, resulting in $\frac{|u_{s+1}-u_s|}{\delta_0} \gtrsim 1$), the system presents a highly nonlinear wave dynamic behavior. In this regime, the initial compression δ_0 can be neglected as compared to the displacement of neighboring particles under the dynamic excitations. Using the long-wavelength approximations, the displacement at the neighboring particles can be written in power series about the center point s

$$\begin{aligned} u_{s-1} &= u - u_x(2R) + 1/2u_{xx}(2R)^2 - 1/6u_{xxx}(2R)^3 + 1/24u_{xxxx}(2R)^4 + \dots \\ u_{s+1} &= u + u_x(2R) + 1/2u_{xx}(2R)^2 - 1/6u_{xxx}(2R)^3 + 1/24u_{xxxx}(2R)^4 + \dots \end{aligned} \quad (1.6)$$

Substituting these values into Eq. (1.5), after simplification an analytical approximation is obtained, which is given by

$$u_{tt} = -c^2 \left\{ (-u_x)^{3/2} + \frac{a^2}{10} [(-u_x)^{1/4} ((-u_x)^{5/4})_{xx}] \right\}_x, \quad (1.7)$$

where u is the displacement, $a = 2R$ is the particle's diameter, the subscripts indicate the derivatives, and the strain is $\xi = -u_x$, such that $\xi \equiv -u_x > 0$, c is a material's constant given by $c^2 = \frac{2E}{\pi\rho_0(1-\nu^2)}$, and ρ_0 is the density of the particles. By looking for stationary solution of the form $u(x - Vt)$, Eq. (1.7) has an exact solution, a highly nonlinear solitary wave (HNSW) solution, given by (Nesterenko, 1983 2001):

$$\xi = \left(\frac{5V_s^2}{4c^2} \right)^2 \cos^4 \left(\frac{\sqrt{10}}{5a} (x - V_s t) \right), \quad (1.8)$$

where V_s is the HNSW's velocity in the chain, which is expressed as a function of the ratio of static and dynamic force $f_r = F_d/F_0$ (Daraio et al., 2006b)

$$V_s = 0.9314 \left(\frac{4E^2 F_0}{a^2 \rho^3 (1-\nu^2)^2} \right)^{1/6} \frac{1}{(f_r^{2/3} - 1)} \left\{ \frac{4}{15} [3 + 2f_r^{5/3} - 5f_r^{2/3}] \right\}^{1/2}. \quad (1.9)$$

When the chain is uncompressed, Eq. (1.9) reduces to (Daraio et al., 2006b; Nesterenko, 2001):

$$V_s = 0.6802 \left(\frac{2E}{a\rho^{3/2}(1-\nu^2)} \right)^{1/3} F_d^{1/6}. \quad (1.10)$$

From this analysis, we see that in highly nonlinear regimes the combination of discreteness and nonlinearity in the chain of particles supports the formation and propagation of HNSWs. These nonlinear waves are supersonic in nature, since the characteristic sound speed in the system is zero (Nesterenko, 2001). The waves also have finite spatial width of approximately five particle diameters, which is independent of any system parameter or wave amplitude. From Eq. (1.10), we see that the solitary wave speed V_s is a nonlinear function of the maximum dynamic contact force F_d . The propagation properties of these waves can therefore be tuned by modifying the particle's dimension and material properties (Coste et al., 1997; Daraio et al., 2006b; Nesterenko, 2001). These solitary waves can also be considered as solitons in a physically reasonable approximation (Nesterenko, 1983 2001), though small amplitude secondary solitary waves were observed in numerical calculations after collision of two identical solitary waves (Manciu et al., 2000; Sen et al., 2008). The ratio of the largest amplitude of the secondary wave to the amplitude of the original wave is about 0.02 (Manciu et al., 2000).

After the initial work of Nesterenko on the nonlinear waves in the chain of spherical particles in 1983, he and Lazaridi (Lazaridi and Nesterenko, 1985) showed the first experimental evidence of solitary waves in the chain of spherical particles. Nesterenko's original work on the solitary wave propagation is based on the continuum limit of a discrete particle chain under the Hertzian contact with neighboring particles, which assumes the characteristic time of the problem is much longer than the oscillation period of the basic shape of the elastic spherical particle. Friesecke and Wattis (1994) derived a theorem showing the existence of the solitary wave solution of the form $u_n(t) = f(n - ct)$ for a discrete chain having a general type of contact force between neighboring particles, where the contact potential energy has to satisfy their theorem. Using the theorem, MacKay (1999) proved the solitary wave solution for the chain of spherical particles interacting via Eq. (1.1). This work was extended by Ji and Hong (1999) for the general case of arbitrary power-law-type contact force $F \propto \delta^n$ and gave the criteria of $n > 1$ for the existence of the solitary waves in this system.

In the highly nonlinear regime, the traditional linear and weakly nonlinear continuum approach based on the Korteweg-de Vries equation is invalid. Many researchers have

pursued the work numerically and experimentally and verified various wave phenomena in these systems (Chatterjee, 1999; Coste and Gilles, 1999; Coste et al., 1997; Daraio et al., 2005 2006ab; Job et al., 2005 2009; Manciu et al., 2000; Porter et al., 2008 2009; Rosas and Lindenberg, 2003; Rosas et al., 2007 2008; Sen and Manciu, 1999; Sinkovits and Sen, 1995). The unique character of asymmetric potential, tunability, and nonlinearity in the HNSW's propagation presented many interesting new phenomena of wave formation and propagation. When the granular particles are assembled in a linear or network-shaped arrangement, the dual nonlinearity of the system and the heterogeneity of the scales place them in a special class of highly nonlinear behavior.

Chapter 2

Experimental Setup

The first experimental study describing the observation and excellent agreement with numerics for the formation and propagation of HNSWs in the uniform one-dimensional chain composed of spherical beads is reported by [Lazaridi and Nesterenko \(1985\)](#). [Zhu et al. \(1996\)](#) used the optical dynamics of photoelasticity to study the entire field image of wave propagation in several different assemblies. They used particles made of Homalite-100, a photoelastic material, and a high speed camera in their experimental study, which was good in getting the whole field image of the wave propagation, but imposed limitation on the material properties of the particle that could be used in the experiments. Also, direct force information for this setup is not available. [Coste et al. \(1997\)](#), and [Coste and Gilles \(1999\)](#) used force sensors on the chain, perpendicular to the axis of the chain. These sensors were able to measure transverse deformation of the particles and were thus able to calculate the flight time of the wave, but they were not able to determine wave shape. The experimental setup used to study nonlinear waves in granular particles has improved since the first successful experiment reported for nonlinear waves in granular particles. [Daraio et al.](#) and other researchers ([Daraio and Nesterenko, 2006](#); [Daraio et al., 2005](#) [2006b](#); [Job et al., 2005](#)) in recent times have reported successful experimental observation of HNSWs' propagation in the chain of spherical particles and used their setup to study various properties of wave propagation in these chains.

This chapter describes the experimental setups designed during the course of my PhD to study the wave propagation in the one-dimensional chain of granular particles and the

coupling of granular media with the linear elastic media.

2.1 Granular Particles Used in Experiments

We used uniform spherical particles (Figure 2.1a) of $R = [2.38, 4.76, 9.53] \pm 0.01$ mm obtained from McMaster Carr for different sets of experiments. Table 2.1 shows the material properties of the stainless steel (316 type and 440C type), PTFE, and brass beads used in this research (Bauccio, 1993; Efundu Inc., 2011).

In our study, we explored the effects of the particle's geometry and orientation on the formation and propagation of highly nonlinear solitary waves. We tested uniform chains composed of ellipsoidal particles, cylindrical particles, and hollow spherical particles, respectively. Figure 2.1 shows pictures of different types of granular particles used in the course of this research to study wave propagation properties in granular media and their applications. The ellipsoidal particles used in this study (Figure 2.1b) were stainless steel 316 type supplied by Kramer Industries, and they had mass $m_e = 0.925 \pm 0.001$ g, the minor axis $D = 4.72 \pm 0.01$ mm long and the major axis $L = 10.16 \pm 0.01$ mm. The cylindrical particles (Figure 2.1c) were stainless steel 316 type supplied by McMaster Carr, with the mass $m_c = 0.68$ g, radius $R = 2.38$ mm, and length $L = 4.76$ mm. The aluminum hollow spherical particles used in the experiments had mass $m_h = 2.38$ g, diameter of $D = 19.05$ mm, and wall thickness $e_w = 0.87$ mm, giving the outer radius R_0 and the inner radius R_i of the particle as 9.53 mm and 8.66 mm, respectively.

2.2 Instrumented Sensor Particles

We used M different instrumented (sensor) particles ($M = 2$, unless otherwise specified) within the granular chain, to record the wave propagation. These instrumented particles were fabricated in our laboratory by placing a piezoelectric (lead zirconate titanate) disc ($RC \sim 10^3 \mu s$, Piezo Systems, Inc.) with custom micro-miniature wiring (supplied by Piezo Systems, Inc.), between two cut halves of a particle, carved to accommodate the

sensor wires, and joined using a stiff epoxy adhesive in a manner similar to [Daraio et al. \(2005 2006b\)](#). The piezo elements were electrically insulated by Kapton film (McMaster, low-static polyimide with $66.0 \mu\text{m}$ thickness) to prevent discharge to the neighboring elements or to the ground through setup. They were further fabricated such that their total mass was approximately equal to the mass of the other particles in the chain. The resonant frequency of the assembled instrumented particle was in much higher range compared to the working frequency of wave propagation in the chain. We placed these instrumented particles in the chain at the selected locations and connected them with Tektronix oscilloscopes to monitor the force-time responses of the traveling excitations.

All sensor particles were pre-calibrated by us, using the conservation of momentum principle. The calibration factor helps in converting the acquired voltage data into the cor-

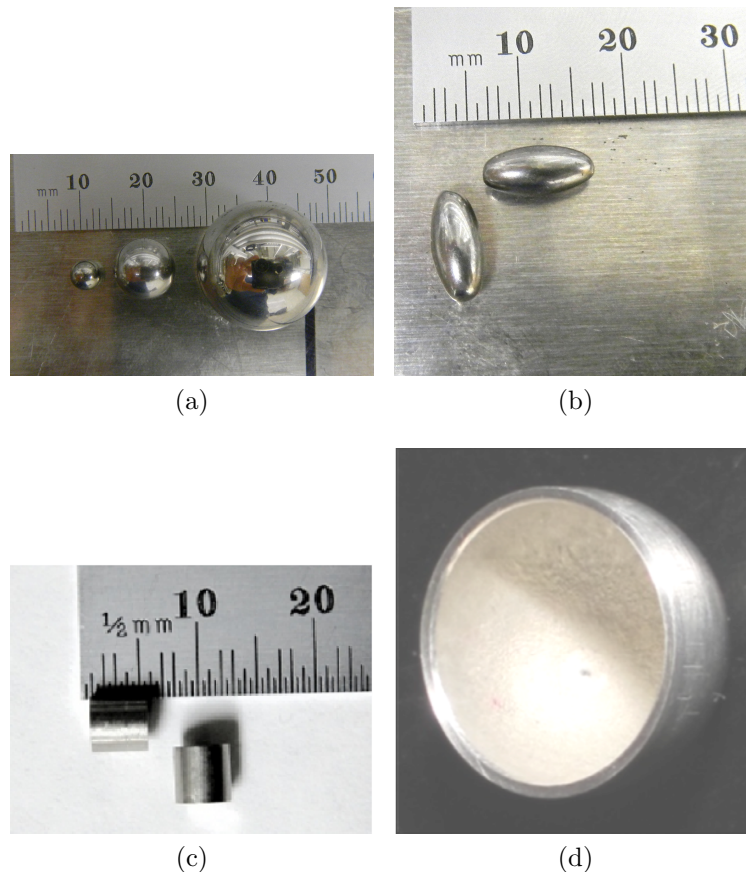


Figure 2.1: The four different types of granular particles used in the course of this research to study wave propagation properties in granular media and their applications: (a) spherical particles, (b) ellipsoidal particles, (c) cylindrical particles, and (d) hollow sphere

Material	ρ (kg/m ³)	E (GPa)	ν
Stainless steel AISI type 316	8000	193	0.30
Stainless steel AISI type 440C	7800	200	0.28
Copper	8960	115	0.35
Brass (360)	8550	103	0.34
Aluminum 6061-T6	2693	68.9	0.33
Nylon (Polyamide)	1140	6.52	0.40
Acrylic (Polymethylmethacrylate)	1186	4.75	0.35
Polycarbonate	1196	3.75	0.35
PTFE (Polytetrafluoroethylene)	2151	1.53	0.46

Table 2.1: Material properties of different types of particles and specimens used in the experiments. The reported values are standard specifications (Efund Inc., 2011) except Young’s moduli of polymers, which were extrapolated from Hugoniot relationship (Carter and Marsh, 1995).

responding force response of sensor particle (Daraio et al., 2005). The piezoelectric discs used for fabricating the instrumented particles were considered to measure the voltage proportional to the load applied, which is an excellent approximation in the working range of our setup, as the resonant frequencies of these piezoelectric discs are much higher. Therefore, we can write $F(t) = \kappa V(t)$, where $F(t)$ is the applied force on the particle and $V(t)$ is the voltage-time response of the sensor particle obtained from the oscilloscope. The sensor particle was excited by an impact from a striker particle of known mass and velocity, i.e., of known initial linear momentum. During total contact time with the striker particle, the sensor particle undergoes compression in time t_{compress} , followed by a restitution period $t_{\text{restitution}}$. We calculated momentum of the sensor particle by measuring the area under the curve of voltage-time series from the beginning of the impact to the maximum value of the voltage, which is when the compression period t_{compress} ends. The momentum calculated from the voltage-time curve was equated with the initial linear momentum of the striker. The boundary conditions selected for the striker were as follows: $v_i(t = 0) = U \equiv \sqrt{2gh}$, where h was the drop height of the striker and U was the impact velocity. When the striker particle comes to rest at the end of the compression period, we have $v_f(t = t_{\text{compress}}) = 0$. Using the linear momentum equation, we get

$$\kappa = \frac{m\sqrt{2gh}}{\int_0^{t_{\text{compress}}} V(t)dt}. \quad (2.1)$$

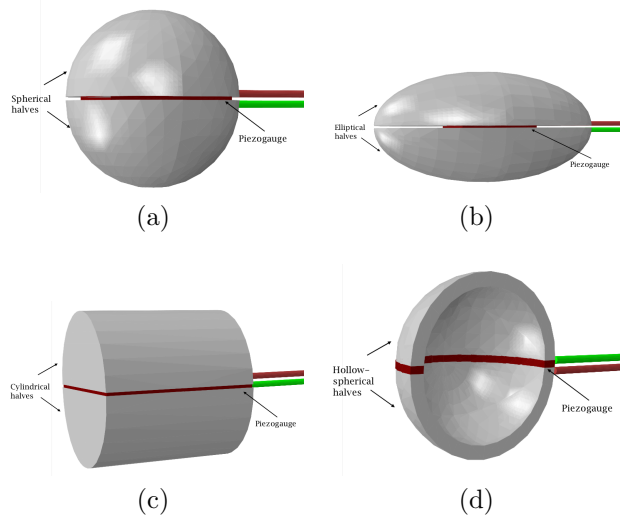


Figure 2.2: Schematic diagram representing the assembly of the piezogauges embedded inside selected (a) spherical particles, (b) ellipsoidal particles, (c) cylindrical particles, and (d) hollow-spherical particles, respectively

The instrumented sensors for the hollow spherical particles' assembly were custom fabricated by sandwiching a piezoelectric ring sensor (provided by Steiner & Martins, Inc., with an outer diameter of 19 mm, an inner diameter of 12 mm, and a thickness of 0.75 mm) between two halves of a hollow sphere and joining them together using epoxy adhesive (Figure 2.2d).

2.3 Chain of Granular Particles

Figure 2.3 shows the vertically aligned experimental setup primarily used in this study, which had a uniform one-dimensional chain composed of N granular particles ($N = 20$, unless otherwise specified). The particles were supported by four guided rods, which constrained the particles' motion along the axis of the chain. These guided steel rods were coated with Teflon tape to reduce the friction between them and the spherical particles. The chain was arranged with no static precompression load, which implies that the particles were in point contact in the initial state, before the dynamic excitation.

We also built a horizontal setup with similar settings. As the wave travels horizontally in the chain and the gravity acts vertically, or perpendicular to the chain, we can neglect the gravitational field in the wave propagation direction. Nevertheless, we provided a small

inclination of 3° to the setup to prevent any initial gap opening in the chain.

A single propagating pulse in the chain is excited using an impact from a striker particle, which is identical to the other particles composing the chain (Nesterenko, 2001). To accurately repeat the initial impact conditions for different specimens, the striker was released using a DC-powered linear solenoid, which allowed us to obtain highly reproducible impacts with only 0.45% standard deviation in the impact velocity distribution. We also used a high-speed Vision Research Phantom V12 camera to measure the actual impact and rebound velocity of the striker, thereby being able to characterize the energy losses. For the horizontal setup, we used a Delrin ramp in the shape of a quarter-circular arc to release the striker. We obtained the force time response of the traveling pulse from the instrumented sensor particles placed at selected known locations in the chains. The average wave velocity (V_s) of the traveling pulses in the chain was calculated by dividing the distance between the centers of two sensor particles by the transit time measured for the wave to propagate between them. The average dynamic force amplitude (F_d) of the propagating pulse was calculated by averaging the force amplitude measured at the two sensor particles.

Figure 2.4 shows the wave propagation detected in the horizontal experimental setup, which consisted of a one-dimensional chain of $N = 70$ stainless steel 316 type spherical particles. In this case, the sensor particles were placed at location numbers 9, 16, 24, 31, 40, 50, 56, and 63 in the chain from the impacted end. The wave was generated using an identical striker with an impact velocity of $v_{\text{imp}} = 1.77$ m/s. As mentioned by Zhu et al. (1996), we found stable formation of solitary wave after the first 5–7 particles. More details about experimental results and comparisons with the numerical models are presented in the following chapters.

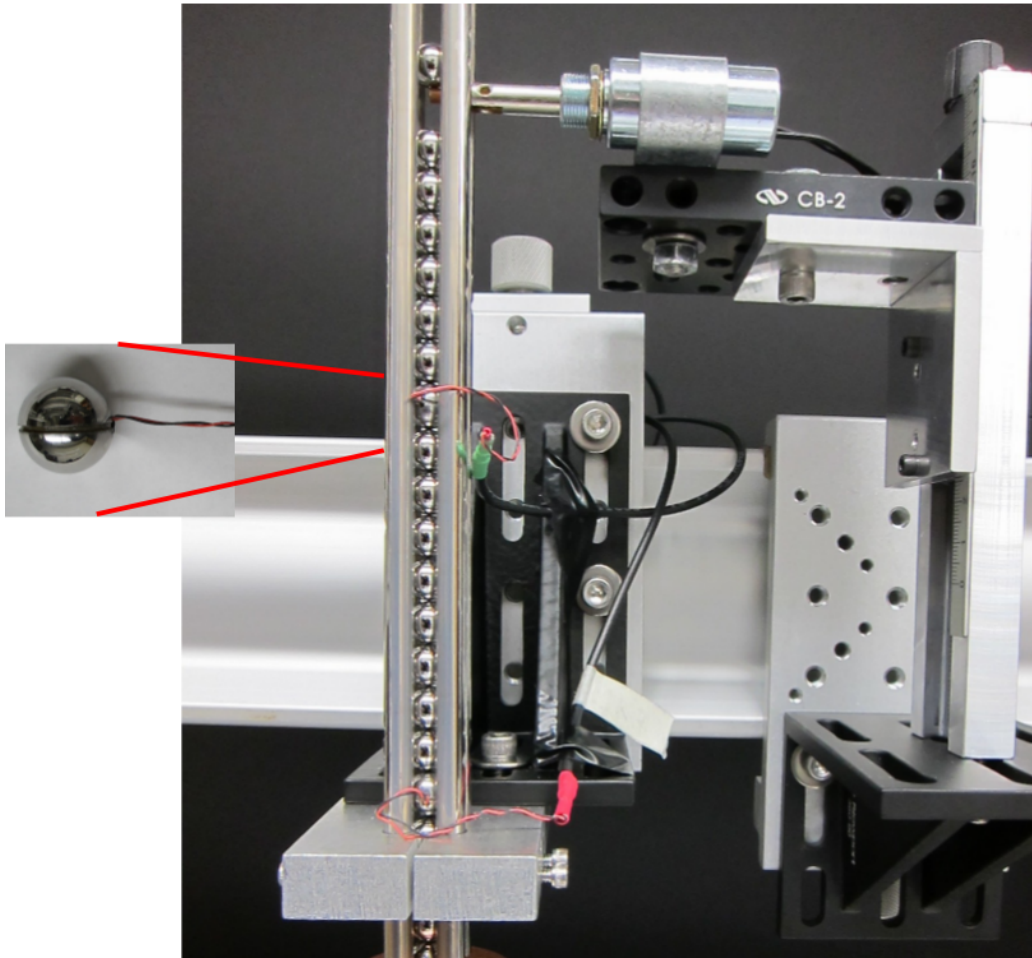


Figure 2.3: Experimental setup for the vertically aligned, one-dimensional chain of spherical beads. Four supporting rods were used to constrain the motion of particles in one direction, along the axis of the chain. Instrumented particles, shown in the inset, were used at the selected location in the chain to extract the experimental data. These instrumented particles were fabricated using a piezoelectric sheet between the two cut halves of the beads. The instrumented particles were connected with Tektronix oscilloscopes, which recorded the signal information. An identical particle, similar to particles composing the chain, was used as striker for exciting a single pulse in the chain. The striker was released from a known height using a controlled-release mechanism

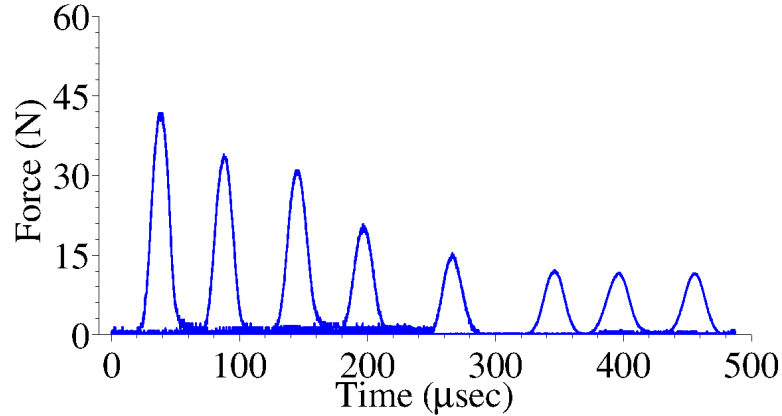


Figure 2.4: Experimental results showing the solitary wave propagation in the chain of 70 stainless steel 316 type particles, when the wave is excited using an identical striker particle with impact velocity = 1.77 m/s . The sensor particles in this case were placed at location numbers 9, 16, 24, 31, 40, 50, 56, and 63 in the chain

2.4 Coupling of Nonlinear Media with Linear Elastic Media–Cylindrical Rods

To understand wave reflection, scattering, and localization at the interface of granular media and the linear elastic media, we performed a theoretically and numerically detailed study (discrete and finite element models) and verified them with experiments. The experimental setup (Figure 2.5) for this testing was composed of a vertically aligned, one-dimensional chain of $N = 20$ stainless steel 440C type particles of radius $R = 4.76 \text{ mm}$ (obtained from McMaster Carr), constrained by four steel guides, as described above. Two instrumented particles ($M = 2$) were used at particle location numbers 7 and 16. An identical bead particle was used as a striker to excite a single solitary wave in the chain, with a drop height of $h_{\text{imp}} = 1 \text{ cm}$ for each specimen. The drop height of 1 cm was selected to minimize the possible onset of plasticity at or around the contact region (Johnson, 1987).

Various cylindrical samples of single and double layers consisting of different heights and materials were used as specimens. These specimens were placed adjacent to nonlinear media at the bottom end of the chain, such that they could interact with granular media. We assumed that under the prescribed excitation conditions, these specimens behave as linear elastic media. We clamped these cylindrical specimens using a massive V-block to

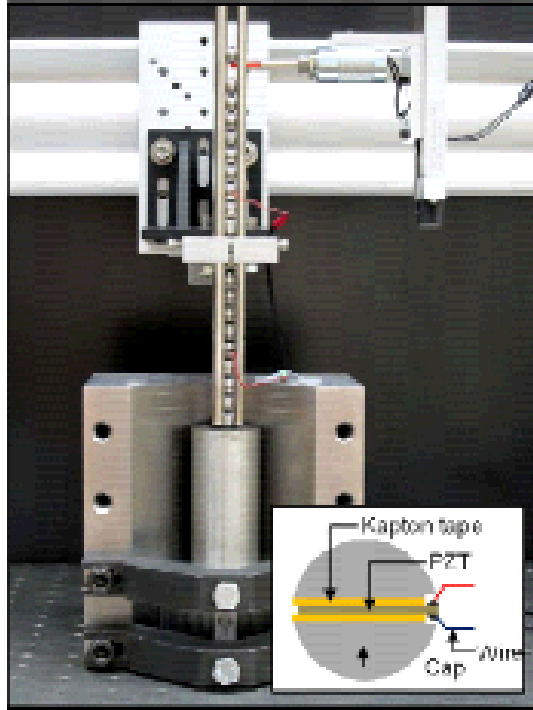


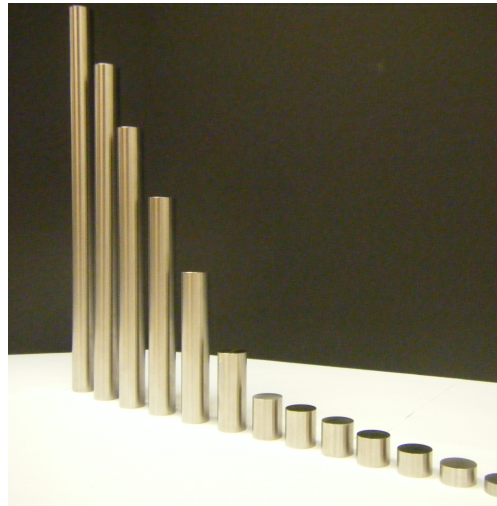
Figure 2.5: Experimental setup showing the one-dimensional, vertically aligned chain composed of 20 stainless steel spherical particles placed on top of a cylindrical sample. The bottom of the sample was under fixed boundary conditions using a V-block mount. The striker particle was control released from a known height using the solenoid

apply fixed boundary conditions on the far end. Figure 2.5 shows the experimental setup as described above for the chain of spherical particles coupled with cylindrical samples. All the samples used in this testing were axisymmetric, and their centerlines were aligned with the axis of the granular particles chain. This alignment of samples to the chain prevents the generation of flexural waves along the cylindrical linear members, which allows us to consider the wave treatment analyses in numerical and theoretical studies as one-dimensional analysis with linear elastic assumptions.

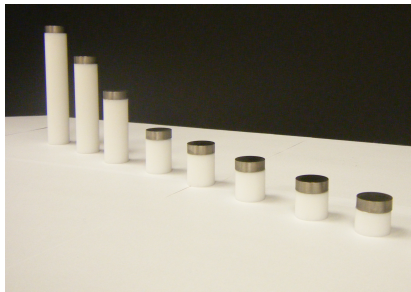
The tested samples used in this study were categorized in 4 different sets to simulate various states of linear media. The first set of samples tested were uniform cylinders of a single layer made of various different materials, ranging from hard metals to soft polymers, so as to assess the effects of their mechanical properties on the reflection of the incident solitary waves (Figure 2.6a). Table 2.1 provides the material properties for the different metallic and polymer specimens. The standard specifications of the metallic specimens were obtained from [Efundu Inc. \(2011\)](#), and for the polymer specimens, Young's moduli values were extrapolated using Hugoniot relationship ([Carter and Marsh, 1995](#)). The



(a)



(b)



(c)



(d)

Figure 2.6: Various specimens used in the experimental study for interaction of granular media with adjacent linear elastic media. Single-layered uniform cylindrical specimen for variation of: (a) elastic modulus; and (b) geometrical length. Double-layered composite cylindrical specimen with stainless steel layer in the top and PTFE layer in the bottom for the variation: (c) inertia of upper layer H_{upper} and (d) stiffness of lower layer H_{lower}

cylindrical samples were 76.2 mm tall with radius 19.1 mm, i.e., ~ 4 times larger than the radius of the chain-composing spheres. The larger cross-sectional area of specimens was selected to neglect the axial movement of the cylinders, thereby reducing the wall displacement condition of samples as half-space, semi-infinite wall, in theoretical and numerical models (Goldsmith, 2001; Ripperger, 1953).

The second set of cylindrical samples was used to understand the effect of the cylinder's geometry on the interface dynamics between nonlinear and linear media. All of the samples tested in this set were stainless steel 440C type cylinders (Table 2.1) with a radius of 9.53 mm, twice the bead radius in the granular chain. In this set, we tested 14 different samples of various heights ranging from 6.35 mm to 610 mm (Figure 2.6b).

Sets 3 and 4 were used to investigate the effect of adjacent layered composite media. The samples in these two sets were double-layered composite media, with stainless steel 440C type cylinders glued on top of polytetrafluoroethylene (PTFE) cylinders using epoxy adhesive. The radii of both the stainless steel and PTFE cylinders were 9.525 mm. Figure 2.6c shows the specimen used in Set 3, where we observed the effects of variation of the upper layer's inertia on the interface by varying the stainless steel cylinder heights from 6.35 mm to 101.6 mm, while keeping the height of the lower layer PTFE, 25.4 mm, constant. Similarly, in Set 4 (Figure 2.6d), we analyzed the effects of the lower layer's material stiffness on the interaction of nonlinear media with adjacent-layered media. In this case, the upper-layer stainless steel cylinder had a constant height of 6.35 mm and the PTFE cylinder height was varied from 9.52 mm to 152.4 mm.

2.5 Coupling of Nonlinear Media with Linear Elastic Media–Plates

We also studied the interaction of nonlinear granular media with adjacent thin plate structures. We first analyzed the effect of geometric configurations by varying the size of granular particles and plate thickness. We further studied the effect of plate boundary condition on the interface dynamics of granular media and plate. The experimental

setup for this testing consisted of three sets of vertically aligned, one-dimensional uniform chains of $N = 20$ stainless steel 440C type spherical particles, with particle diameters $D = 4.76, 9.53, \text{ and } 19.1$ mm, respectively, and three thin aluminum panels (Alloy 6061, dimensions = 914×914 mm) of different thicknesses $t = 2.29, 3.18, \text{ and } 4.83$ mm, respectively. The material properties of spherical particles and aluminum plates are as described in Table 2.1. The two instrumented particle sensors were placed at location numbers 7 and 16. Each aluminum plate was positioned horizontally, or perpendicular to the axis of granular chain, and at the far end of the chain in contact with the bottom end of the 20th particle. A single solitary wave in each set of granular chain was excited with the impact from a respective identical striker, having impact velocity $v_{\text{imp}} = 0.31$ m/s for each case. Two of the plate edges in one direction were applied with fixed boundary condition by clamping them with the fixed support system, and the other two edges in other direction were free. To investigate the thickness effects and boundary effects on the interface dynamics, we varied the position of each granular chain set on respective plates along their centerline in the direction of a fixed boundary condition with a spatial interval of granular chain on the plate from 10 mm up to a 200 mm distance from the fixed support, which was increased by 20 mm afterwards up to the center of the panel. The signal output from the instrumented particles was recorded using a data acquisition device and was transferred to a computer. The testing was repeated five times at each location to obtain a statistical distribution of measurement results.

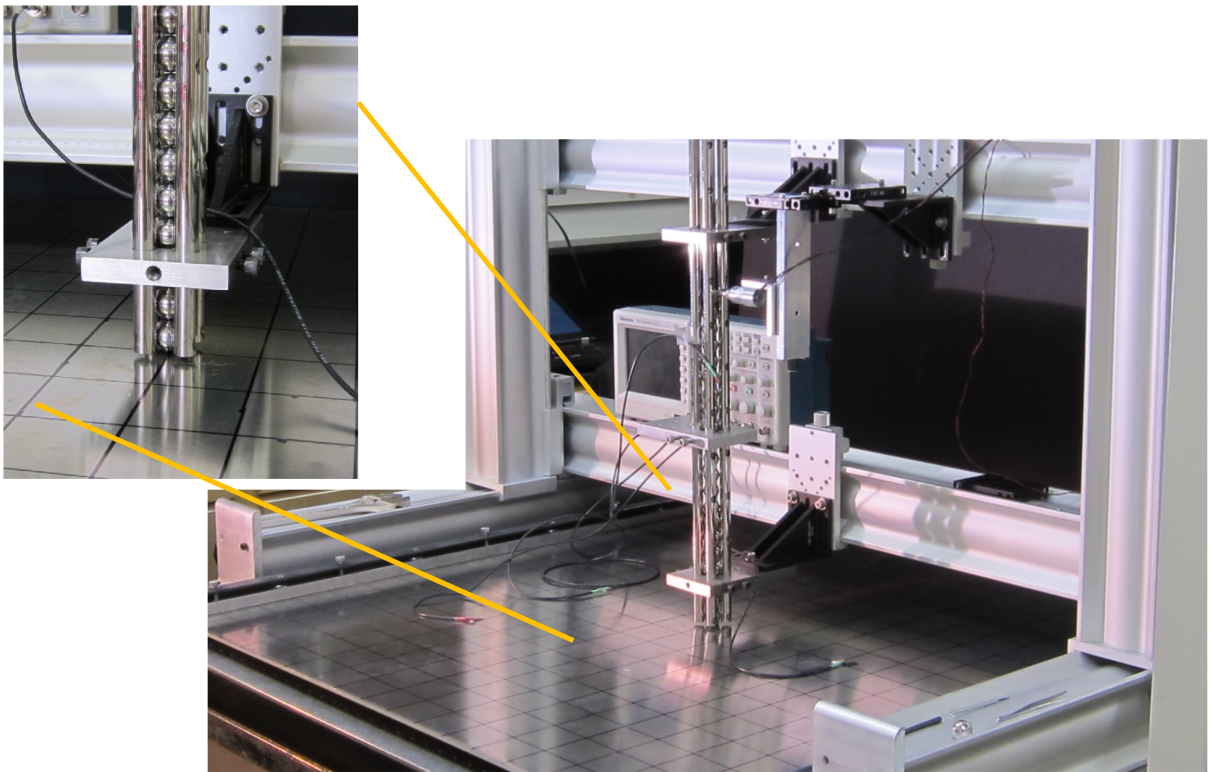


Figure 2.7: A granular media composed of stainless steel spherical particles aligned vertically along the dotted central line of an aluminum plate

Chapter 3

Numerical Modeling of a One-Dimensional Chain of Spherical Particles

3.1 Discrete Particle Model (DPM)

The discrete particle element model (DPM) is similar to molecular dynamics and is frequently used for granular particles dynamics. Cundall and Strack ([Cundall and Strack, 1979](#)) developed the discrete element method for granular particles in 1979 to study rock mechanics. The model was successful in describing many phenomenons of rock mechanics and found attraction among researchers. The model determines the behavior of an idealized granular material by calculating the motion of individual particles as they interact with each other and with the boundaries. It is primarily based on the impulse-momentum law and assumes each particle as a single point mass connected by a spring (linear/nonlinear) with a neighboring particle, thus imposing a single degree of freedom.

Recently, discrete particle models have been used to describe the dynamics of a one-dimensional chain of granular particles. The model considers the chain of N granular particles as point masses connected by nonlinear springs with the adjacent particles in a one-dimensional system, where the nonlinear spring works according to Hertz contact law (Equation (1.1)) in compression and it applies zero force in tension. Nesterenko used this model to describe his analytical discovery of HNSWs in the chain of granular particles

(Nesterenko, 1983). In recent years, this model has been used extensively to study various properties of nonlinear waves in granular structures (Brunhuber et al., 2006; Carretero et al., 2009; Chatterjee, 1999; Coste et al., 1997; Daraio et al., 2006b; Harbola et al., 2009; Herbold and Nesterenko, 2007; Job et al., 2009; Nesterenko, 2001; Nesterenko et al., 2005; Porter et al., 2008 2009; Rosas et al., 2007; Sen et al., 1998 2008; Vergara, 2006).

The equation of motion of i^{th} particle in our DPM can be written as

$$\ddot{u}_i = \frac{(k_e)_{i-1,i}}{m_i} [u_{i-1} - u_i]_+^{3/2} - \frac{(k_e)_{i,i+1}}{m_i} [u_i - u_{i+1}]_+^{3/2} + g \quad (3.1)$$

where u_i is the displacement of the i^{th} particle ($i \in [1, \dots, N]$), $(k_e)_{i,j}$ represents the contact stiffness between i^{th} particle and j^{th} particle, m_i is the mass of i^{th} particle, g is gravitational acceleration, and $[x]_+$ denotes the positive part of x . The particle $i = 0$ is the striker, and $i = (N + 1)^{\text{th}}$ particle represents the rigid wall (the wall displacement was fixed and its principal radii of curvatures at the point of contact with N^{th} granular particle were set as infinity). For the vertically aligned system, the model includes the gravitational force effect, i.e., $g = 9.81 \text{ m/s}^2$, and for the horizontally aligned system, the gravitational force was absent in the direction of the chain, therefore, $g = 0$. For the sake of simplicity, the basic DPM neglects the effect of dissipation in the shorter chain of granular particles ($N = 20$). The equation was solved in the time domain using the fourth-order Runge-Kutta method.

As described in Section 2.2, the instrumented particles in our experiments detect the force measurements at the center of granular particles, whereas, the force value measured in the DPM was the Hertzian contact force. In order to compare the experimental results with the DPM, a coefficient β , as in (Daraio et al., 2005), was calculated. The β value was defined as a ratio of the maximum dynamic force on the particle contacts $F_{d,n}$ to the maximum average of the dynamic forces acting on the two contacts of the given particle $F_{m,n}$ as $\beta = F_{d,n}/F_{m,n}$. It is to be noted that, both $F_{d,e}$ and $F_{m,n}$ were obtained in discrete particle simulations. The maximum contact force F_m between particles, used in the analytical formulation (Eq. (1.10)), can be expressed as (Daraio et al., 2005):

$$F_m = \beta F_{m,e} + F_0, \quad (3.2)$$

where $F_{m,e}$ is the experimentally measured force in the instrumented particles and F_0 is the initial precompression (caused by gravitational loading in our experimental setup). In our analysis, F_0 was selected as a constant value equal to the gravitational compressive force at the midpoint between the two sensors in the chain. The results thus obtained with DPM were compared with the experimental findings by assuming the sensor-particles as rigid bodies, and by calculating the forces at the central section. This was done by averaging the contact forces on the two sides of the corresponding particle (Daraio et al., 2005).

Although results obtained with DPMs have been shown to provide good agreement with experimental measurements, they fail to capture the full three-dimensional physical response of the systems. For example, DPMs cannot predict the local stress concentrations at the point of contact, they do not account for the presence of elastic waves propagating within the particles, and they do not capture dynamic responses deriving from complex contact geometries and the effects of nonlinearities in the materials' constitutive response.

3.2 Finite Element Model (FEM)

We developed finite element model (FEM) of chains composed of granular particles by considering the particles as three-dimensional deformable bodies of revolution, such that their dynamic response was characterized by accounting for multibody interactions between particles and local contact deformation. The model is thus capable of taking into account the local deformation of the particles at the contact point, the corresponding changes of the contact area, and the vibrational energy within the particles. A commercially available FE software, Abaqus, was used for all our simulations (Simulia, 2008). This section explains the integration scheme, the contact model, and the particle discretization method used.

3.2.1 Integration Schemes

The equation of motion, which captures the dynamic response of the system in our FEM is defined by

$$[M]^t \ddot{U} + [C]^t \dot{U} + [K]^t U^t = R_{ext}^t, \quad (3.3)$$

where $[M]^t, [C]^t, [K]^t$ are mass, damping, and stiffness matrices; $U^t, \dot{U}^t, \ddot{U}^t$ are the displacement, velocity, and acceleration vectors at time t ; and, R_{ext}^t is the external load vector.

Eq. (3.3) was integrated by Abaqus-Explicit using the stable central-difference operator. The central difference rule used in the explicit scheme calculates the solution for the time step $(t + \delta t)$ directly from the known solution at time step (t) . To preserve conditional stability of the scheme, the time step (δt) should be smaller than a critical value δt_{cr} , given by:

$$\delta t \leq \delta t_{cr} = \frac{2}{\omega_{max}} (\sqrt{1 + \xi_{max}^2} - \xi), \quad (3.4)$$

where ω_{max} is the highest frequency of the system with n degrees of freedom, and ξ_{max} is the fraction of the critical damping of the highest mode. An approximation to the stability limit is often written as the smallest transit time of a dilatational wave speed across any of the elements in the mesh as:

$$\delta t_{cr} \approx \frac{L_{min}}{c_d} (\sqrt{1 + \xi_{max}^2} - \xi), \quad (3.5)$$

$$c_d = \sqrt{\frac{(\lambda + 2\mu)}{\rho}}, \quad (3.6)$$

where c_d is the dilatational wave speed expressed in terms of the effective Lamè's material constants, λ and $G = 2\mu$. L_{min} is the dimension of the smallest element in the mesh. The time increment (δt) used for the analysis must be smaller than the stability limit of the central-difference operator (δt_{cr}) . Failure to use a small enough time increment may result in an unstable solution.

The total cost of the analysis is inversely proportional to the magnitude of the time step. From Eq. (3.5), the stable time increment (δt_{cr}) is directly proportional to the

minimum element length (L_{min}). Refining the mesh in the domain reduces the time increment step, while gaining accuracy of the solution. However, the use of very small time increments results in the increase of the total computational cost of the analysis, and can also cause spurious oscillations in the solution (Gibbs' phenomena). Thus, an optimum time increment is needed to obtain the desired result with efficient computational costs.

3.2.2 Contact Model in Abaqus

When the chain of particles is excited by an impact, the system is subject to multiple contact interactions between adjacent particles, all of which need to be characterized simultaneously. The discretization of the continuum surface by a finite number of points creates a fundamental discontinuity of forces at the contact, applied only at the nodes. These discontinuities can lead to convergence problems in the FEM, particularly in the dynamic setting of interest.

These issues were overcome by defining the contact problem using the "contact pair" mechanism in Abaqus-Explicit. The approach required a detailed definition of each contact pair, defining the contact properties in the normal and tangential directions and specifying the exact surface of the two particles that were involved in the contact pair. In the "contact pair" mechanism, the model tracks the approach between a primary (master) surface, corresponding to particle 1 in the contact pairs, and the secondary (slave) surface, corresponding to particle 2 in the contact pair, using the surface-to-surface method. In this method, the normal projections of the two surfaces were traced to determine the extent of the particles' interpenetration. The surface-to-surface method calculates the average force value in the discretized elements by area integration. This average force has a continuous distribution over the elements in the contact surface, ensuring stability and convergence of the problem.

The contact pair tracking method in Abaqus-Explicit is also affected by the selection of the specific contact enforcement algorithm. The contact pair technique has two different contact enforcement algorithms: the kinematic and the penalty algorithm. We selected the

kinematic algorithm in our model, in which the solver first advances the kinematic state of the model at each time increment into a predicted configuration without considering the contact conditions, and then it determines which slave nodes penetrate the master surfaces. The resisting force required to oppose the penetration was calculated from the physical pressure-overclosure relationship, which depends on the depth of each slave node's penetration and the mass associated with them.

We used hard contact pressure over-closure in the normal direction, and for simplicity, no friction in the tangential direction. The hard contact pressure over-closure mode does not allow the transfer of tensile stress across the interface when the two surfaces move apart, while producing an adequate amount of push-back force to avoid over-closure or penetration within the set limits of error tolerance.

3.2.3 Particles' Modeling

The discretization of the particles in space was done using volumetric solid (continuum) elements with different degrees of mesh refinement (more refined at the impact zones). We selected tetrahedral elements of second order, specifically modified 10-node C3D10M. The axis-symmetric bodies were discretized in space using triangular six-noded modified quadratic axis-symmetric elements (CAX6M).

Since, most materials used in our simulation are assumed to be made with incompressible properties, this lead to severe straining of the structures in the contact zone and may result in spurious pressure stresses. The spurious pressure stresses may generate unstable modes in the structure by making it too stiff and influencing its bending behaviour. This phenomenon is called volumetric locking. Similarly, in shear locking results in rise in parasitic stresses in the structure. The modified elements provide a robust solution during large deformation and contact analyses, and they exhibit minimal volumetric- and shear-locking. The advantage of using tetrahedral and triangular element in three dimensional and two dimensional bodies respectively, is that they provide the convenience of meshing the complicate geometries and also provide the ease of transistion from a refined mesh in the contact zone to a coarse mesh away from the zone area.

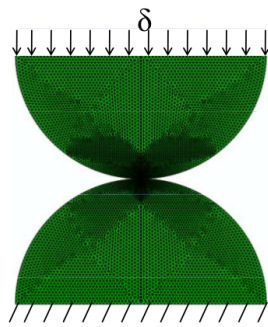
The modified elements also use lumped mass method formulation for generation of mass matrix. In the lumped mass formulation, the mass of the element is assumed split equally or lumped on the integration points only, which provide the advantage of having a diagonal mass matrix. Since the inverse of a diagonal matrix is also diagonal and the diagonal matrix can be stored easily in a vector, it provide significant computational advantages, which are suitable for explicit dynamics. The lumped mass matrix has its downside, that in some cases it can result in singular mass matrix, which become computationally cumbersome.

3.3 Numerical Validation

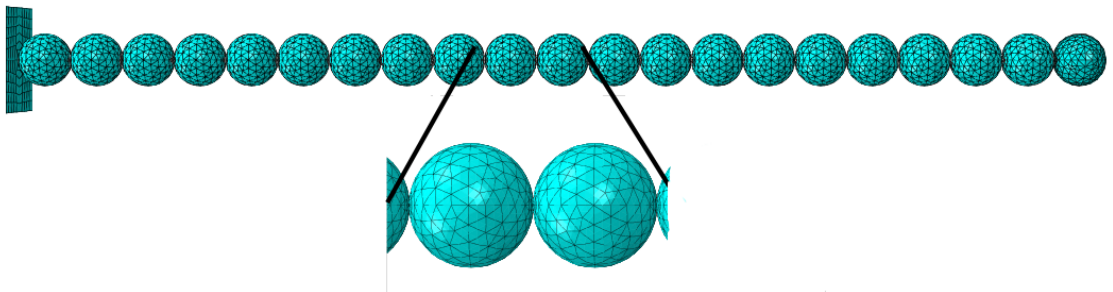
3.3.1 Quasi-Static Validation

The quasi-static regime of our model was validated by tracking the displacement of two hemi-spherical particles in contact under compressive loading, and we compared the FEM results with the values obtained with the Hertz contact law (Eq. (1.1)). The model consisting of two hemi-spherical particles was generated in Abaqus-CAE with $\sim 12,000$ tetrahedral elements (Section 3.2). We assigned a fixed boundary condition to the diametric plane of the lower particle, and uniform vertical downward displacement to the diametric plane of the upper particle (Figure 3.1a).

The simulation of the compressive loading was performed in Abaqus-Explicit. To enforce quasi-static deformation, the loading rate was artificially decreased to maintain the maximum velocity of any nodal point to less than 1% of the dilatational wave speed of the sound in the material (Eq. (3.6)). We used a “smooth step” loading rate to provide a smooth increase and decrease of the acceleration, with no abrupt changes. The loading rate was prescribed by a fifth-order polynomial, and has first- and second-order time derivatives equal to zero at the beginning and end of the transition to simulate the quasi-static assumptions. The smooth step loading rate reduces the dynamic effects of the system without reducing the stable time increments.

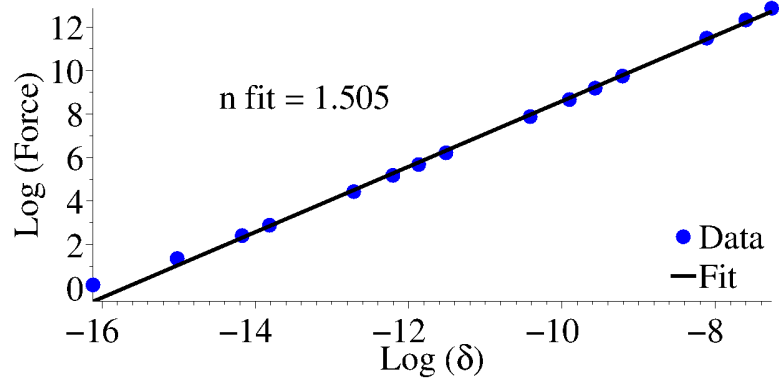


(a)

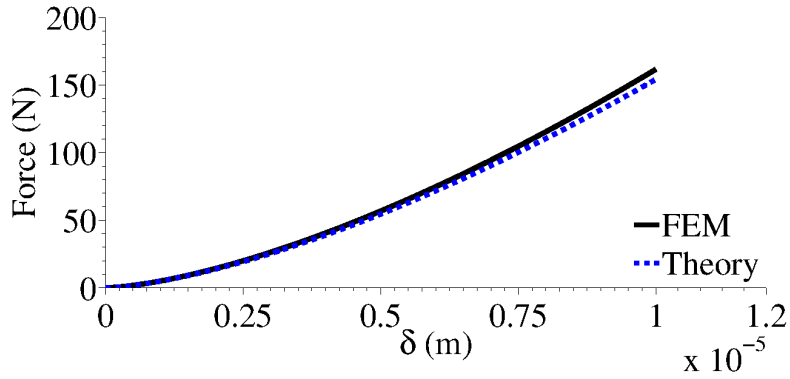


(b)

Figure 3.1: (a) FEM consisting of two hemi-spherical particles in contact. (b) FEM showing the one-dimensional chain of 21 spherical particles in contact with each other. The first particle on the right was used as striker particle



(a)



(b)

Figure 3.2: Quasi-static validation of our model. (a) Logarithmic fitting of the calculated contact force as a function of the applied displacement δ . The solid dots correspond to numerically obtained contact forces at given displacements, and the solid line is the linear fit. (b) Comparison of the force-displacement relation obtained from simulations (solid (black) curve), and the Hertz contact law (Eq. (1.1), dashed (blue) curve)

The displacement δ was applied on the top particle over a time t_1 . This displacement corresponds to the relative approach of the centers of two particles, as the lower particle's center was fixed. After the maximum displacement value was attained, the value was maintained constant for additional time t_2 , so that the velocities of all the nodal points approach zero. This maintains the kinetic energy of the system below 1% of the potential energy, reaching values less than 0.01% during t_2 .

Simulations were run for different values of displacement δ_i ($i = 1, 2, \dots, N$), such that the δ_i was always much smaller than the particle's radius (to maintain the small displacement assumptions of the Hertz's contact theory (Johnson, 1987)). Fitting the numerical results with a power-law force-displacement ($F - \delta$) function, an exponent equal to $n \sim 1.505$ was obtained (Figure 3.2a), similar to the force-displacement relationship obtained by the

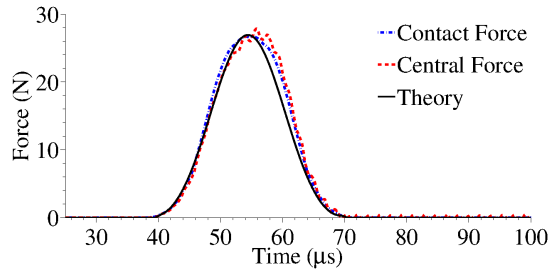


Figure 3.3: Dynamic validation of our model. Force profile of the solitary wave at particle number 10. The dash (blue) curve corresponds to the force obtained with our FEM averaging the forces measured at the contacts. The solid (red) curve corresponds to the force obtained with our FEM at the central section of particle 10. The solid (black) curve with star markers was obtained from the HNSW theory (Eq. (1.8))

Hertz’s contact law (Figure 3.2b).

3.3.2 Dynamic Validation

We validated the dynamic response of our FEM by comparing the FEM results with the values obtained with a DPM (Section 3.1), with the results obtained using the highly non-linear wave theory (Section 1.5), and also with the experimental measurements (Chapter 2). We compared two characteristics: (i) the shape of the propagating wave at a selected location in the chain (in terms of evolution of the force profile in time), and (ii) the scaling of the wave velocity as a function of the dynamic force amplitude.

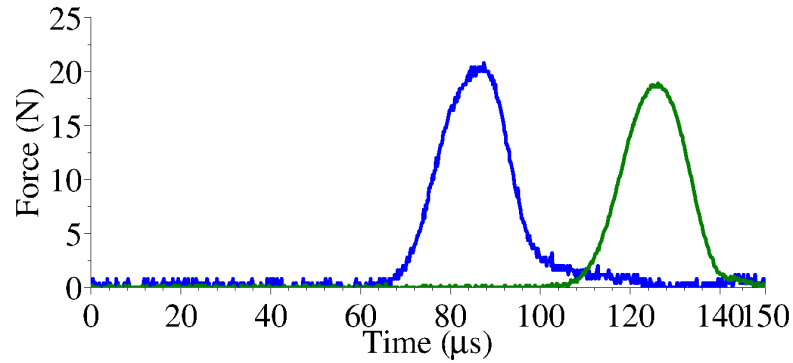
Using the integration scheme described in Section 3.2, an assembly of $N = 21$ uniform stainless-steel 316-type spherical particles (Section 2.1) was generated in Abaqus-CAE with $\sim 120,000$ tetrahedral elements (Section 3.2, Figure 3.1b). The first particle was used as a striker, and a fixed wall boundary condition was enforced at the opposite end of the chain by modeling the boundary as a perfectly rigid plate in contact with the last particle in the chain. We assigned a predefined velocity (determined from experiments) to the striker particle.

As mentioned in Section 3.1, the force value calculated in conventional DPMs is at the contact between two particles, while the sensor-particle used in experiments detects the force at its central plane (i.e., on the diametric surface perpendicular to the axis of the chain). In our FEM, we followed two different approaches to calculate the force-time

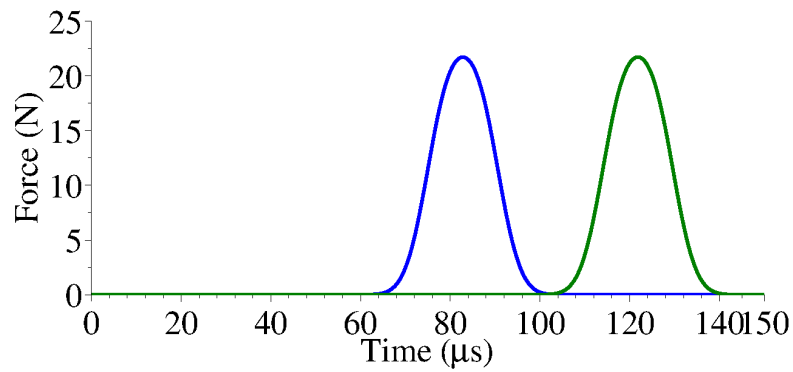
response of individual particles: In the first approach, the contact force values were averaged similarly to the process followed in the DPM (Section 3.1). In the second approach, a surface normal to the chain's axis was generated on the central section of the sensor particle, and the force transmitted through the surface was calculated by integrating the stress over the surface area. The theoretical force value was determined using Eq. (1.8), where the solitary wave speed V_s was obtained from the FEM simulation results. Figure 3.3 shows a comparison of the calculated force at the particle's central surface using the two approaches in the FEM described here and the theoretical Hertzian value. The small oscillations noticeable in the force profile calculated at the central section of the particle were related to the propagation of elastic waves in the bulk.

The wave propagation was compared at two locations in the chain (10th and 15th particles in the chain, Figure 3.4). The striker impact velocity used for the experiment in this case was $v_{imp} = 0.63$ m/s and the HNSW's speeds obtained from the FEM, the DPM, and the experiments were 641 m/s, 635 m/s, and 610 m/s, respectively. Figure 3.4a shows the force-time response measured by the sensor particles in the experiments. Figure 3.4b and Figure 3.4c show the same data obtained through the DPM and the FEM, respectively. It is evident that all methods are in very good agreement. Figure 3.5 shows the comparison of the variation of HNSW's speed V_s as a function of the maximum dynamic contact force F_d , obtained from theory (Eq. (1.10)), FEM, and DPM simulations.

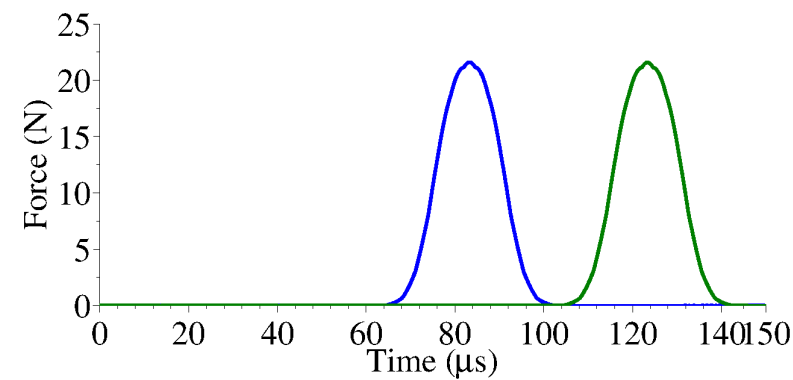
With the static and the dynamic validation, we showed that the FEM is capable of describing interactions between granular particles, and it is also able to capture the formation and propagation of HNSW in a chain of spherical particles. The model describes the HNSW qualitatively and quantitatively in terms of shape, length, amplitude, and speed. The results obtained with the one-dimensional discrete particles model and the three-dimensional FE model are in excellent agreement with each other confirming the validity of the point mass approximation to study one-dimensional chains of spherical particle dynamics.



(a)



(b)



(c)

Figure 3.4: Wave propagation detected at particles 10 (blue) and 15 (green) from the impacted end of the chain. (a) Experiments, (b) DPM, and (c) FEM results obtained with the contact force averaging method (first approach described above). The wave was generated with a striker having an impact velocity of 0.63 m/s.

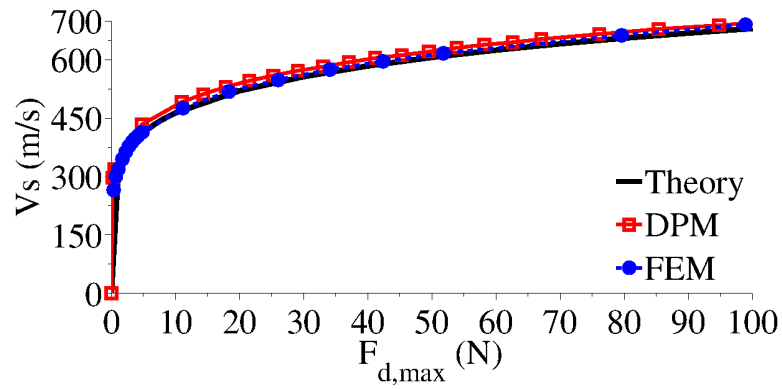


Figure 3.5: Comparison of the variation of HNSW's velocity as a function of wave amplitude, obtained from FEM, DPM, and theory. The solid (black) curve represents the values obtained from theory (Eq. (1.10)). The solid (red) curve with square markers represent the results obtained from DPM, and the dashed (blue) curve with circular markers represent the results obtained from FEM.

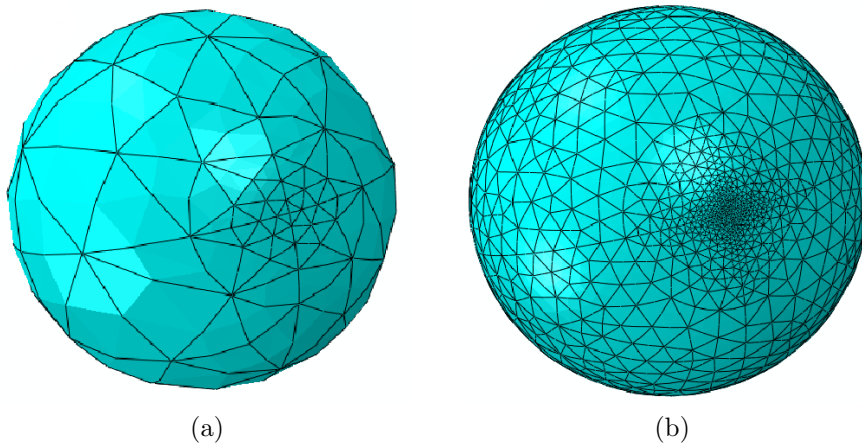


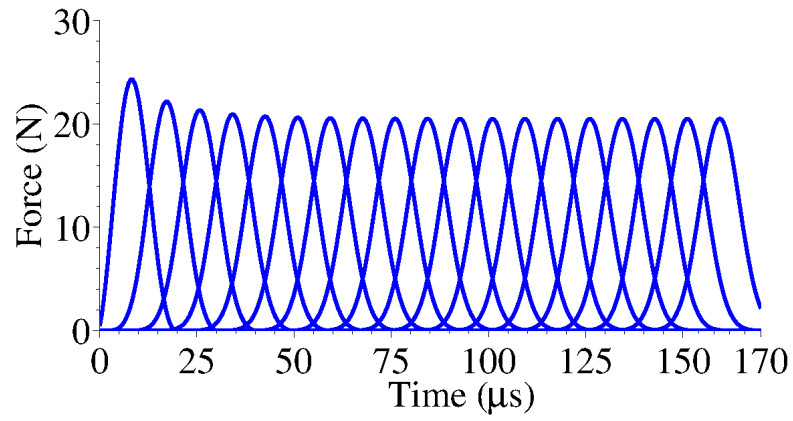
Figure 3.6: FEM meshes for an individual particle in the two extreme cases tested: (a) a particle with the least refined mesh density, and (b) a particle with the most refined mesh density. The particles were discretized in space using tetrahedral elements of second order for all the FEM sets.

3.4 Mesh Convergence

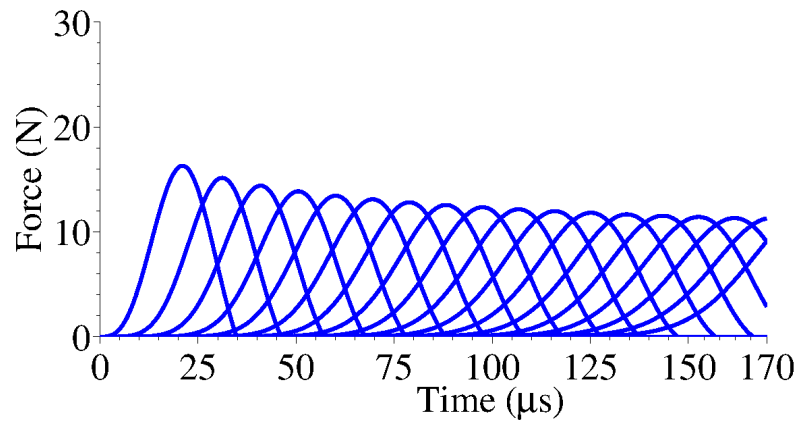
A mesh convergence study was performed to avoid numerical errors and to optimize computational costs. We used the h-refinement technique, in which the mesh density is increased while keeping the element type the same (Reddy, 1993). An acceptable solution is achieved when the degree of freedom of the system (“N”) tends to infinity $N \rightarrow \infty$, and the solution converges to a value independent of the discretization choice.

For the mesh convergence study, we modeled the dynamics of a chain of particles excited by an identical striker with an impact velocity of 0.5 m/s. Different assembly sets were generated with the FEM in increasing order of mesh density. Figure 3.6 shows the meshes generated for an individual particle in the uniform chain for the two extreme sets, the least refined mesh (Set 1, Figure 3.6a) and the most refined mesh (Set 11, Figure 3.6b). The total number of elements used for modeling the $N = 21$ spherical particles were 12070 in Set 1, and 431195 in Set 11. When analyzed on the same computational processing unit (CPU), the time taken by the system to simulate Set 1 was 0:7:02 hours and to simulate Set 11 was 19:11:02 hours. From Eq. (3.5) the stable time increment δt for a given element size decreases with the mesh refinement, thereby increasing the computational cost. Figure 3.7 compares the evolution of the force-time profile of the traveling pulses through all the contacts in the chain obtained with the DPM, and with the FEM for the least and most refined mesh sets.

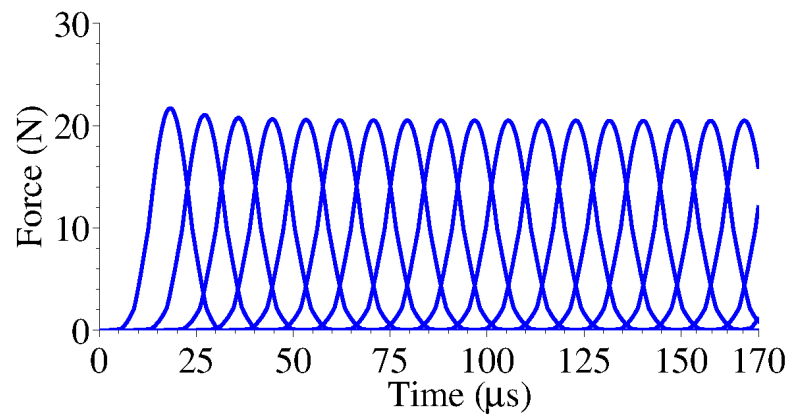
The convergence of the model to the limit solution is shown in Figure 3.8. The evolution of the maximum contact force, calculated between particle number 15 and 16 in the chain, is shown in Figure 3.8a as a function of the FEM sets in increasing order of mesh refinement. Similarly, the computed wave velocity is shown in Figure 3.8b. Both panels of Figure 3.8 also compare the FEM results with the results obtained with the DPM. The comparison shows that the wave profile obtained from the chain of particles with the least refined mesh deviates significantly from the one obtained with the DPM. On the contrary, results obtained with the most refined mesh were in excellent agreement with the DPM. The wave amplitude and wave speed obtained with the DPM were 20.5 N and 560 m/s, respectively, and the same values obtained with the converged set (most refined) in the



(a)

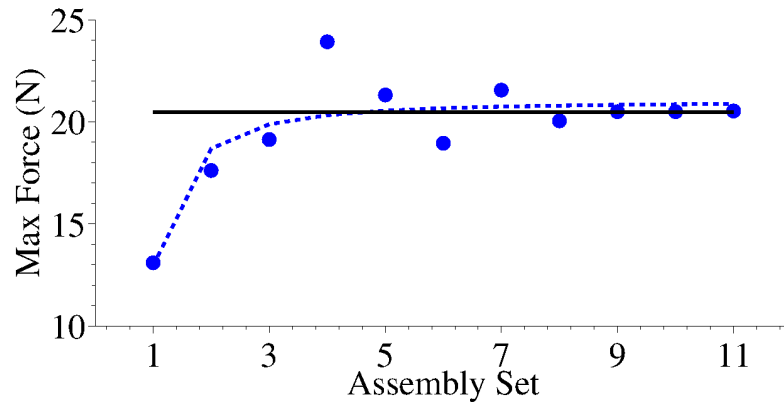


(b)

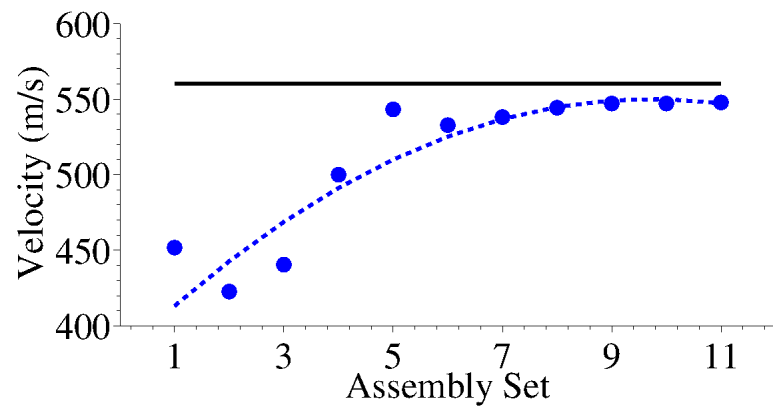


(c)

Figure 3.7: Comparison of the results obtained from (a) DPM, (b) FEM set with the least refined mesh, and (c) FEM set with the most refined mesh, for the HNSW traveling in a uniform chain of 20 stainless steel spherical particles excited by a striker, with an impact velocity of 0.5 m/s



(a)



(b)

Figure 3.8: (a) HNSW's force amplitude obtained from FEM in increasing order of mesh refinement. The y-axis represents the maximum contact force (N) between particles at location number 15 and 16. (b) HNSW's velocity obtained from FEM in increasing order of mesh refinement. The x-axis for both the figures represents the assembly sets used in increasing mesh density. The solid (black) curve is the force amplitude calculated from the DPM. The dotted (blue) markers and the dashed (blue) curve are the HNSW's force amplitude and fitting calculated from the FEM. In both panels we observe that as the mesh was refined the force amplitudes and the wave speeds converge to the value calculated from the DPM.

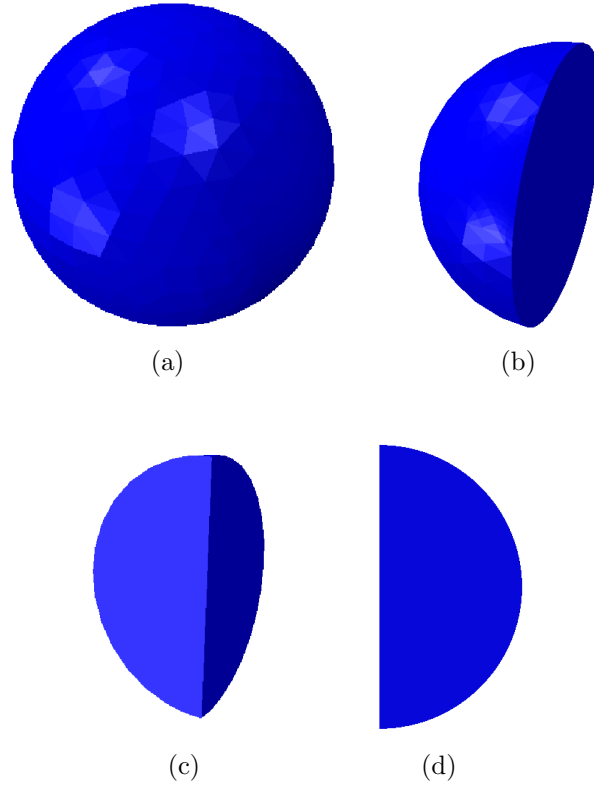


Figure 3.9: Symmetric study of particle in the chain. For this study, we generated the three different types of particles, each having a symmetric property, and compared the solitary wave propagation results with the chain of full spherical particle. (a) Full three-dimensional spherical particle, (b) hemi-spherical particle having symmetric property along one plane, (c) quarter-spherical particle for model having symmetricity in two different planes along transverse direction, (d) axis-symmetric two-dimensional spherical particle

FEM were 20.53 N and 552.8 m/s.

3.5 Symmetric Boundary Condition on Beads

A three-dimensional finite element model (Figure 3.9a) has the advantage of analyzing true geometry effect without any simplifications or assumptions in the boundary and loading conditions. Systems used in many practical applications have symmetric boundary and loading conditions, such that the full model geometry is not needed for analysis. The simplified model used for the analysis will save computational time and resources. We now compare four different models of chain of spherical particles having geometric and loading symmetric, “full-sphere”, “hemi-sphere”, “quarter-sphere”, and “axis-symmetric”. Fig-

ure 3.9a shows the full three-dimensional body used for HNSW in the chain of spherical particles. For the system with symmetric reflection in one of the transverse directions, a hemispherical body of particles (Figure 3.9b) can be used to model the HNSW. Similarly, quarter-spherical (Figure 3.9c) and axis-symmetric bodies (Figure 3.9d) can be used for systems with two reflection symmetric planes and rotational symmetry, respectively.

Figure 3.10 shows the wave propagation in the four different models described above. The first (blue) and second (red) curves represent the signal output obtained from the instrumented particle at location numbers 7 and 16 in the chain, respectively. The magnitude of the signal obtained from the chain of the “hemi-sphere” model was provided with a gain of factor two, and for the “quarter-sphere” model the force profile was provided with a gain of factor four. A good comparison of wave amplitude, shape, and speed for all the models confirmed that the symmetric models of particles, with the appropriate boundary and loading conditions, were able to determine the results qualitatively and quantitatively when compared with full three-dimensional spherical particle model of HNSW.

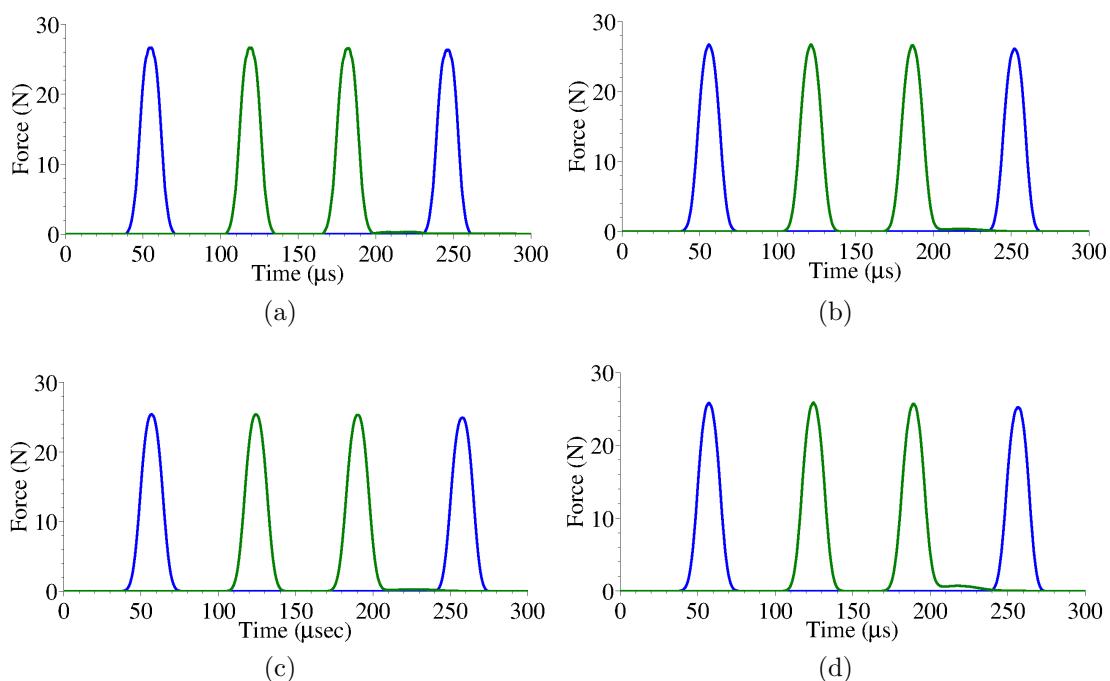


Figure 3.10: Wave velocity study for four different models for the homogeneous chain of 20 particles. Each model has different symmetric condition in transverse direction. The y-axis and x-axis is force (N) and time (μs), respectively. (a) For the chain composed of full three-dimensional spherical particles. (b) For the model having symmetry loading and boundary property in one transverse plane, each particle was constructed using hemispherical and symmetric property in the respective plane. (c) For the model having two transverse plane symmetry, we used quarter spherical particles. (d) For the model having axis symmetric properties, we used two-dimensional axis symmetric particles for the chain. In the wave plots, the first solid curve (blue) and second curve (red) represent the force observed at the center of the 7th and 16th particle, respectively, in the chain. The third curve (red) and fourth curve (blue) are the reflected waves from rigid wall at particles number 16 and 7.

Chapter 4

Dissipation in a One-Dimensional Chain of Spherical Particles

4.1 Introduction

Dissipation plays an important role in the dynamics of the physical systems. In an ideal infinite long system consisting of chain of spherical particles under no initial compression or very weakly precompressed, the magnitude of highly nonlinear solitary wave propagating in them will remain constant. Because of energy dissipation, experimental results have shown a characteristic decrease of the force amplitude during the propagation of HNSWs through the chain of spherical particles (Brunhuber et al., 2006; Carretero et al., 2009; Herbold and Nesterenko, 2007; Herbold et al., 2006; Rosas et al., 2007). Since the thermal fluctuations were neglected in the granular materials, the characteristic losses in the dynamics of the system comes from the mechanical energy dissipation. Dissipation in this system is usually assumed to be viscous or proportional to velocity. E. Falcon et al. (1998a) did the experimental study of one inelastic ball bouncing off the ground, in which they found that a dissipative model based on a viscoelastic mechanism leads to an evolution of the restitution coefficient identical to the experimental results. For most of the materials, the critical impact velocity which causes a plastic deformation of the surfaces is very small, on the order of $v_{\text{critical}} \approx 0.1$ m/s (page 366 of Johnson (1987)). Therefore, the plastic indentation on the particles' surface is also another cause of dissipation in the system.

Manciu et al. (2001) studied the wave propagation in the chain of spherical particles having inelastic material behavior. They used the restitution coefficient to determine the unloading forces using $F_{\text{unloading}}/F_{\text{loading}} = 1 - w$. In their numerical study, they found that, even though the HNSW's amplitude attenuates during the propagation in the chain, the impulse propagates without any dispersion. Rosas and Lindenberg (2003) and Rosas et al. (2007) did analytical and numerical study on the chain of particles assuming friction as the primary cause of dissipation and found that the energy decreases exponentially due to friction as the wave propagates, and also that there was small amount of backscattered waves present in the chain. Later, Rosas et al. (2008) updated their model for the chain of particles with a damping factor included such that the damping in the chain was proportional to relative velocity of the particles. In their particular numerical model, they observed generation of secondary pulse and decay of primary pulse proportional to the viscosity. For low viscosity values and for higher viscosity values, they observe a spatially lengthening excitation of a monotonic front. Herbold et al. (2006) even investigated the wave propagation in the chain of particles immersed in viscous fluids, by immersing the experimental setup of the chain in various fluids of different viscosity; a decrease in wave velocity was observed as the viscosity of the fluid was increased.

The above mentioned models were not able to capture the cumulative effects of all the different parameters, both qualitative and quantitative, on the decay of a wave, as observed in experimental studies. From the previous studies and understanding, we know that the energy losses in the one-dimensional chain of spherical particles is caused by a number of factors at the local scale alone which contribute to the dissipation during the binary collisions between the particles (for example, due to inherent material properties (Job et al., 2005), plasticity (Pane and Blank, 2006), or friction (Wang and Zhu, 2009)), or due to the global state of the system (for example, disorderness (Manciu et al., 2001) in the system, fragmentation of the chain (Hinch and Saint-Jean, 1999), or arrangement of the particles in the confined walls of experimental setup).

The FEM is useful in studying the HNSW dynamics in arbitrary shape particles, and for studying interface dynamics and coupling with adjacent media, whereas the DPM model based on a single degree of freedom is useful in several optimization schemes, and to study

other wave propagation behavior under proper circumstances with minimal computational resources. Thus, both the numerical approaches require an effective dissipation model to predict the exact change in incident and reflected signals for practical applications, such as NDE/SHM. Adding a damping factor in the equation of motion is a convenient way of including the cumulative effect of dissipation, without modeling each effects in detail. In our study, we developed an analytical model describing the effective dissipation using the form of a discrete Laplacian in the velocities with uniform exponent and a material-dependent prefactor. For systematic modeling and analysis of system, we included linear Rayleigh damping parameters in the FEM and verified them with experiments.

4.2 Simulation

4.2.1 Discrete Empirical Model

We considered a one-dimensional horizontal chain of $N = 70$ spherical particles described in Section 2.3. In a nondissipative system, the equation of motion describing particles' displacement was given by Eq. (1.5) (Nesterenko, 2001). To model the dissipative effects of the physical system, we included a nonlinear viscous drag model, based on the relative velocities between the particles. The equation of motion for the dissipative model in our system was given by

$$\ddot{y}_n = A \left(\delta_n^{3/2} - \delta_{n+1}^{3/2} \right) + \gamma s \left| \dot{\delta}_n - \dot{\delta}_{n+1} \right|^\alpha, \quad (4.1)$$

where $s \equiv \text{sgn}(\dot{\delta}_n - \dot{\delta}_{n+1})$, $A \equiv E\sqrt{2R}/[3m(1-\nu^2)]$, $n \in \{1, \dots, N\}$, y_n was the coordinate of the center of the n -th bead, $\delta_n \equiv \max\{y_{n-1} - y_n, 0\}$ for $n \in \{2, \dots, N\}$, $\delta_1 \equiv 0$, $\delta_{N+1} \equiv \max\{y_N, 0\}$, E and ν were the particles' elastic modulus and Poisson's ratio, respectively, and m and R correspond to the particle's mass and R , respectively. The particle $n = 0$ represents the striker particle, $\gamma < 0$ the friction coefficient, and α the power law for the dissipation. Both α and γ were determined by optimizing the numerical results with experimental findings by minimizing the following two differences between

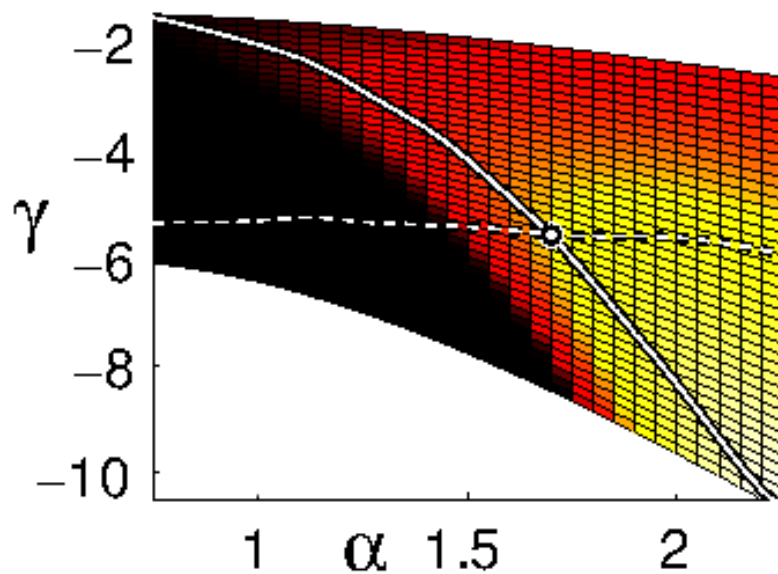
numeric and each particular experiment

$$D(\alpha, \gamma) = \frac{1}{N} \sum_{n=1}^N \frac{|F_m^{\text{exp}}(n) - F_m^{\text{num}}(n)|}{\overline{F_m^{\text{exp}}}}, \quad (4.2)$$

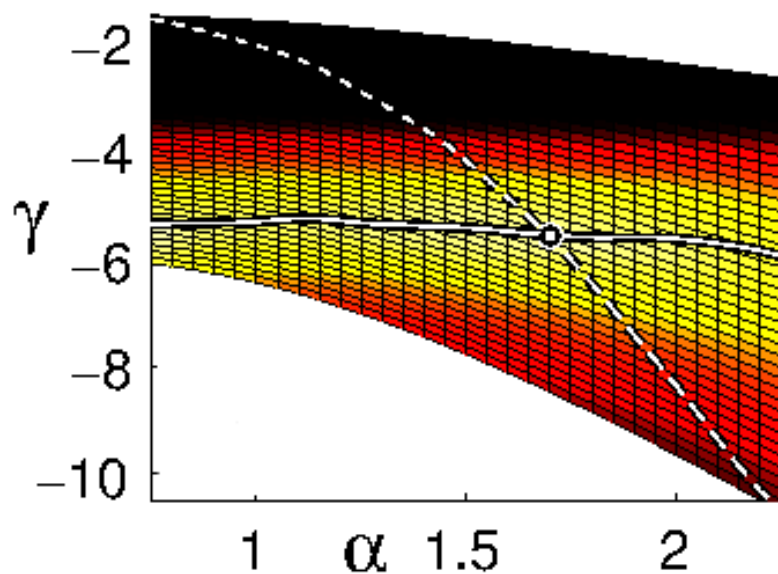
$$\Delta_n(\alpha, \gamma) = \frac{1}{T} \int_{t_i}^{t_f} \frac{|F^{\text{exp}}(t; n) - F^{\text{num}}(t; n)|}{\overline{F^{\text{exp}}(n)}} dt, \quad (4.3)$$

where $\overline{F^{\text{exp}}} \equiv (1/N) \sum_{n=1}^N F_m^{\text{exp}}(n)$, $F^{\text{exp}}(n) = \int_{t_i}^{t_f} F^{\text{exp}}(t; n) dt$, $F(t; n)$ was the force data obtained from the n^{th} sensor, and $F_m(n) = \max_t \{F(t; n)\}$ was the maximum force observed by the n^{th} sensor over the time span of wave propagation $t \in [t_i, t_f = t_i + T]$. The superscripts “exp” and “num” denote the experimental and numerical data. The function $D(\alpha, \gamma)$ measures the “difference” between the numeric and the experiment using the *maxima* of the forces through all sensors of the experiment. The function $\Delta_n(\alpha, \gamma)$ measures the difference between experimental and numerical pulses at the n^{th} sensor. To compare the numerical and experimental wave forms and to avoid biasing $\Delta_n(\alpha, \gamma)$ with the difference in force magnitude, we rescaled the experimental results such that the experimental maxima match the numerical maximum value. That is, $F^{\text{exp}}(t; n) \rightarrow F^{\text{exp}}(t; n) \times F_m^{\text{num}}(n)/F_m^{\text{exp}}(n)$.

Figure 4.1a and Figure 4.1b show the differences $D(\alpha, \gamma)$ and $\Delta_n(\alpha, \gamma)$, respectively, for a particular range of (α, γ) in the chain of steel particles using a sensor placed towards the end of the chain. From these two figures, we concluded that to determine the complete effect of the dissipation on the wave propagation we need the combined effect of pulse shape and pulse amplitude. An optimized parameter (α_j, γ_j) was determined for experiment j with the corresponding impact velocity v_j by finding the intersection between the minima of both the differences (force maxima and pulse shape) over the four different sensors, and by finding the average over them. The global optimal average dissipation parameters were determined by taking the average over all the experiments $(\alpha, \gamma) = \frac{1}{N} \sum_{j=1}^{N_e} (\alpha_j, \gamma_j)$, where $N_e = 10$ different experiments.



(a)



(b)

Figure 4.1: Optimization of the dissipation coefficients (α, γ) for a chain of 70 steel particles. (a) Difference $D(\alpha, \gamma)$, as defined in Eq. (4.2), between the force maxima observed in the experiment and our model. (b) Difference $\Delta_n(\alpha, \gamma)$, as defined in Eq. (4.3), in wave forms between the experiment and our model for a sensor placed at location $n = 56$. The solid and dashed curves in panel (a) correspond to the minima obtained from panels (a) and (b), respectively.

4.2.2 Finite Element Model

In the FEM, the energy loss in a dissipative physical system (Eq. (3.3)) was controlled by the damping matrix $[C]^t$. The mass and stiffness matrices in the governing equations were computed from physical parameters. However, the calculation of the damping matrix is an abstract concept since it has no physical analog for the cumulative losses. Damping is usually assumed to be viscous or proportional to velocity. In our FEM simulations, the damping matrix was modeled using a linear Rayleigh damping form, a special case of Caughey series (Caughey, 1960), where the damping matrix is assumed to be a linear combination of the mass C_M and the stiffness matrices C_K , given by Hughes and Cliffs (1987):

$$C = C_M + C_K = \alpha_1 M + \alpha_2 K. \quad (4.4)$$

(Here α_1 and α_2 are constant values.) This Rayleigh damping model damps the lower frequency signals using the mass proportional damping α_1 and the higher frequency signals using the stiffness proportional damping α_2 . The stiffness proportional damping can be interpreted to capture the energy losses arising due to the deformation of particles, whereas the mass proportional can be related to air or other viscous drag on the system. Although, these assumptions has no rigorous physical basis to the actual dissipative effects and they do not provide natural justification to physical basis. But as will be shown in this section that this linear Rayleigh model, which due to its simplicity is easy to model and yet able to capture the wave dynamics behavior and provide us with useful information of cumulative losses in the system.

The advantage of using Rayleigh wave damping model is that the eigenvectors of the damped system in this case are the same as the eigenvectors of the undamped system. The other advantage of the linear model is that because of the matrix orthogonality properties, the resulting damping matrix C is also diagonal in nature. Which is highly computationally advantageous. Therefore, for mode i the damping ratio (fraction of the critical damping) η_i was written as

$$\eta_i = \frac{\alpha_1}{2\omega_i} + \frac{\alpha_2\omega_i}{2}, \quad (4.5)$$

where ω_i is the natural frequency of the mode i . The spacial wave width of the HNSW propagating in the chain of granular particles depends on the diameter of the particles (Eq. (1.8)). The systems considered in this study have particle diameters in the macroscopic range, thus the inverse of the temporal wave width was on the lower side of the energy spectrum. Also, since the chain of particles, especially metallic particles, do not suffer significant large scale deformation during wave propagation and as mentioned above, the stiffness proportional damping do not contribute significantly to overall energy losses. This implies that the dominating factor for the damping of the propagating waves was α_1 (mass proportional damping).

For our simulations, the value of α_1 , which is constant for the given chain configuration and impact condition, was determined by an optimization process involving minimization of the residual differences between numerical and experimental data by calculating the root mean square deviation ($RMSD(\alpha_1)$) between the values predicted by the FEM and the results obtained from the experiments.

$$RMSD(\alpha_1) = \frac{1}{N} \sum_{n=1}^N \frac{|F_m^{\text{exp}}(n) - F_m^{\text{fem}}(n)|}{\bar{F}_m^{\text{exp}}}, \quad (4.6)$$

where $\bar{F}_m^{\text{exp}} \equiv 1/N \sum_{n=1}^N F_m^{\text{exp}}$, $F(t; n)$ was the data series of the force through the n^{th} sensor, and $F_m(n) = \max_t F(t; n)$ was the maximum value of the force for the incoming wave recorded at the n^{th} sensor. The superscripts “exp” and “fem” denote the experimental and finite element data.

4.3 Results and Discussion

Table 4.1 summarizes our result for three different sets of experiments using stainless steel 316 type, teflon (polytetrafluoroethylene; PTFE), and brass particles each of radius $R = 2.38$ mm, in the last two columns. We found that the dissipation prefactor was material-dependent and a common exponent. This allowed us to augment the standard DPM (Section 3.1) based on Hertzian forces to encompass this dissipation effect in (optimal) quantitative agreement with our experiments.

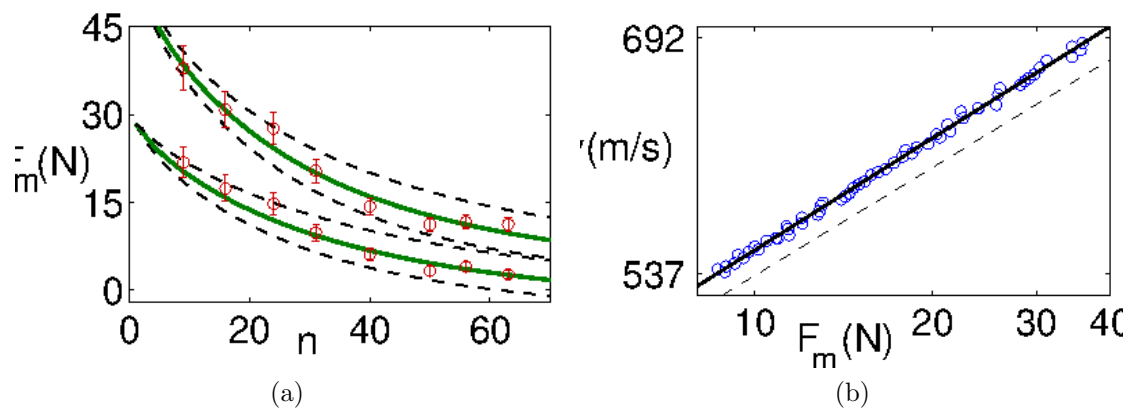


Figure 4.2: (a) Maximum force $F_m(n)$ for experiments with impact velocities v_3 (top curves) and v_8 (bottom curves, displaced by 5 units for clarity). The (red) circles with error bars correspond to the experiment, and the (green) thick curves give the numerical best fit (see the main text) with $(\alpha, \gamma) = (1.81 \pm 0.25, -5.58 \pm 1.30)$. The dashed curves correspond to the extreme cases using the standard deviation found in the optimal parameters. (b) Velocity of traveling front versus the maximum force (in a log-log plot). The solid curves represent the best linear fit, which gives $v \propto F_m^{0.17}$; we also show a dashed line with slope $1/6 \approx .167$.

Material	m (g)	E (GPa)	ν	α	γ
Stainless Steel (316 type)	0.45	193	0.30	1.81 ± 0.25	-5.58 ± 1.30
PTFE	0.123	1.46	0.46	1.78 ± 0.14	-0.582 ± 0.087
Brass	0.48	103	0.34	1.85 ± 0.13	-6.84 ± 0.66

Table 4.1: Material properties (mass m , elastic modulus E , and Poisson ratio ν) for stainless steel, PTFE, and brass. The last two columns present our best estimates, together with their standard deviation, of the dissipation coefficients (α, γ) .

Figure 4.3a shows the wave propagation measured by all the 8 instrumented sensor-particles placed in the chain (solid (blue) curves), the results obtained with a DPM (solid (red) curve with triangle markers) (Carretero et al., 2009), and the results obtained with our FEM (dashed (black) curve with square markers) with the dissipation parameter included. The corresponding optimized value of α_1 for this particular case in the FEM was $\alpha_1 = 6900$ (Nsec/m).

We compare the numerical pulse shape with the experimental data from two selected sensor-particles: the first sensor-particle located in the front half of the chain ($n = 16$, Figure 4.3b), and the second sensor-particle located in the second half of the chain ($n = 56$, Figure 4.3c). The figures show the force profile obtained from the experimental results in the solid (blue) curve, from the DPM (Carretero et al., 2009) in the dashed (red) curve and from the FEM in the dash-dotted (black) curve, for the two sensor particles. Figure 4.3a shows small local differences between the results of our FEM and the wave amplitude obtained in experiments. This may be related to the fact that the linear Rayleigh damping model does not capture the complete dynamics of the system. However, the FEM is capable of capturing the trend of wave amplitude decay (Figure 4.3a), and it is able to describe the pulse shape and velocity within acceptable margins of error. Similar models, including different striker impact velocities and different bead diameters, found consistent results.

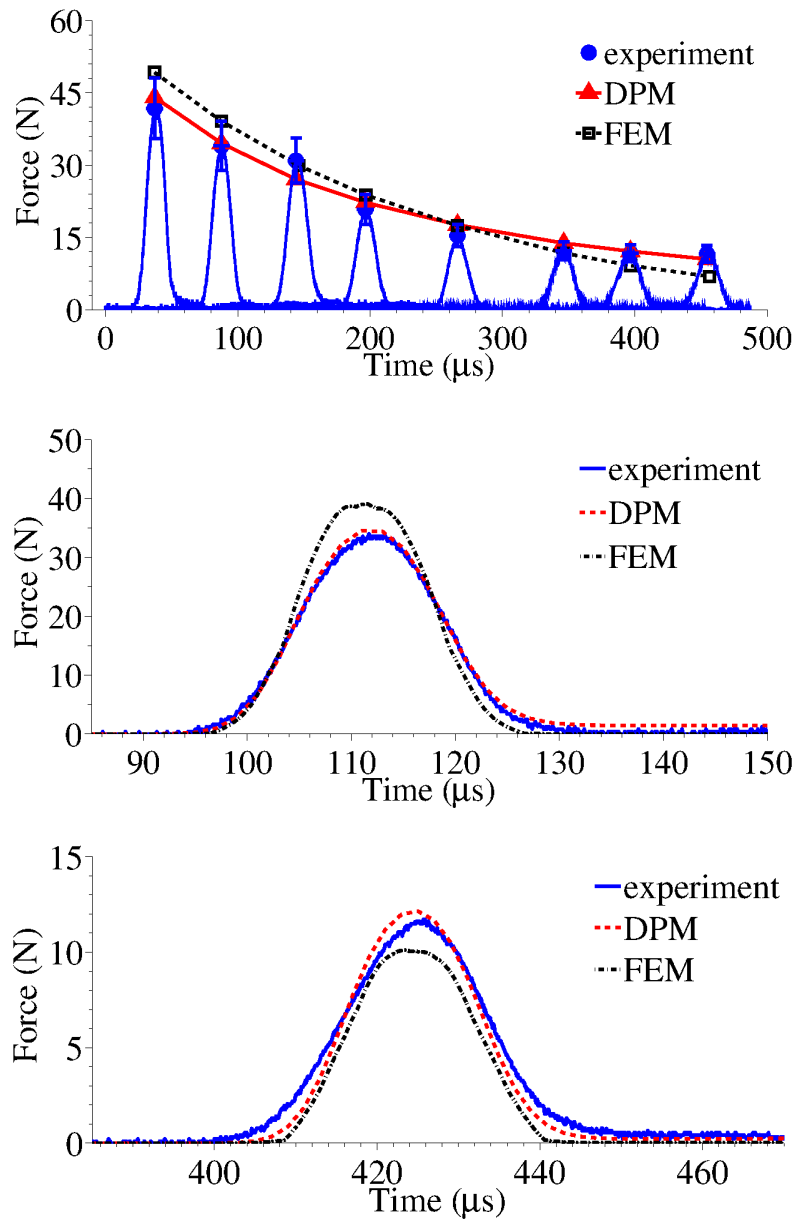


Figure 4.3: (a) Decay of solitary wave in the chain of 70 stainless steel particles for striker velocity = 1.77 m/s. The sensor-particles were placed at location numbers 9, 16, 24, 31, 40, 50, 56, and 63 in the chain. The solid (blue) curves correspond to force values measured in experiments. The solid (blue) curve with circular markers, the solid (red) curve with triangular markers, and the dashed (black) curve with squared markers represent the maximum values obtained from the experimental data, the DPM (Carretero et al., 2009) and the FEM for the best dissipation parameter, respectively. (b) and (c) Force versus time profile in the chain at the sensors positioned in particles number (b) $n = 16$ and (c) $n = 56$. The solid (blue) curve shows the experimental data, the dashed (red) curve represents results obtained with the DPM (Carretero et al., 2009), and the dashed-dot (black) curve corresponds to the results obtained with the FEM for the best dissipation parameters.

Chapter 5

Effect of Particle Geometry on the Dynamics of Granular Media

It has been demonstrated that—by changing the diameters of the particles, their material properties, and/or their periodicity—it is possible to change the solitary waves' amplitude and traveling speed (Daraio et al., 2005 2006b; Porter et al., 2008 2009).

As mentioned in previous chapters, one of the fundamental characteristics of highly nonlinear systems is their high degree of tunability in terms of control over the traveling pulse's width and speed, and the number of separated pulses that can be generated in the chain (Daraio et al., 2005 2006b; Job et al., 2005; Nesterenko, 2001; Porter et al., 2008 2009; Sen et al., 2008). The tunability of these systems is evident when the addition of static precompression on the chain of particles enables the system to change from the highly nonlinear to the weakly nonlinear, and then to the linear wave dynamics regime (Coste et al., 1997; Daraio et al., 2006b; Nesterenko, 2001; Sen et al., 2008). In this chapter, we explore the effects of the particle geometry and orientation on the formation and propagation of the highly nonlinear solitary wave. The role of particle geometry in the dynamic response of granular materials was studied earlier using elliptical disks of hysteretic photoelastic polymers (Shukla et al., 1993). Here, we experimentally test the chains composed of linear elastic uniform bodies of revolutions (ellipsoids, cylindrical particles, and hollow sphere) and compare the results with the theoretical predictions based on the long wavelength approximation for highly nonlinear wave propagation.

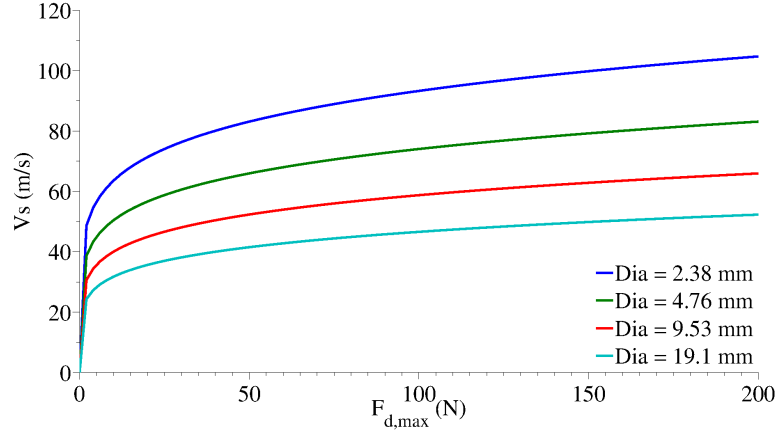


Figure 5.1: Analytical results (Eq. (1.10)) showing the variation of wave velocity with the variation of dynamic loading, in the uniform chain of stainless steel 440C type spherical beads for four different sets of particle diameters $D = [2.38, 4.76, 9.53, 19.1]$ mm

5.1 Particle Size

A remarkable feature of the nonlinear system composed of spherical particles is that the wave length and wave speed in the system can be tuned by selecting particles of appropriate size. By changing the diameters of the composing spherical particles, it is also possible to change the solitary wave's amplitude (Daraio et al., 2005 2006b; Porter et al., 2008 2009). Eq. (1.10) shows that the wave velocity in granular system is inversely proportional to $a^{1/3}$, where a is the diameter of the particles. Figure 5.1 shows the variation of wave velocity for four sets of one-dimensional chains with each set composed of stainless steel 440C-type spherical particles (Table 2.1) with diameter $D = 2.38, 4.76, 9.53,$ and 19.1 mm, respectively. Thus, by increasing the diameter of the particles composing the chain, we decrease the wave speed for the same dynamic force F_d .

5.2 Particle Shape

5.2.1 Contact Interaction between Non-Spherical Particles

When two nonspherical particles come in contact with each other under an applied compressive loading at point O , such that the angle of orientation between the principal axes

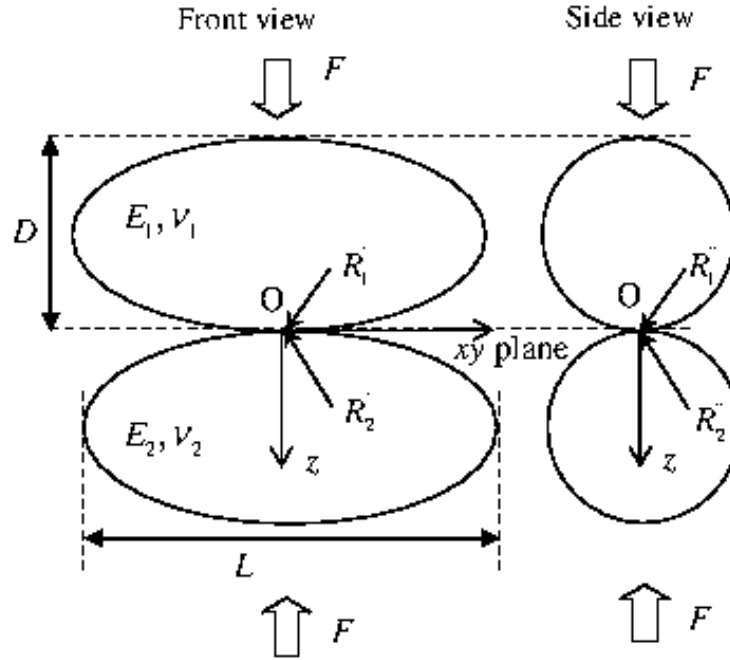


Figure 5.2: Schematic diagram showing the front and side views for the contact between two ellipsoidal particles, and the dimensions and the radii of the maximum and minimum principal of curvatures at the contact points between ellipsoidal particles

directions of each surface is α (as shown in Figure 5.2), then the contact interaction between them is governed by elliptical contact interaction.

In an elliptical contact interaction model (Johnson, 1987), the two particles are supposed to satisfy all of the Hertzian contact interaction assumptions (Hertz, 1882; Johnson, 1987), such that the contacting surfaces of both the particles are continuous, frictionless, and nonconforming. The strain values are assumed to be small in the material, and the problem is considered as elasto-static, i.e., the material response is purely elastic and both of the particles are in static equilibrium. Each particle is also considered as elastic half-space by assuming the contact area remains very small compared to the size of particles at all stages. We assign R_1' , R_1'' as the principal radii of curvatures, where R_1' is the maximum value and R_1'' is the minimum value of all cross sections of particle 1's surface at point O . Similarly, we denote R_2' , R_2'' as the principal radii of curvature of the surface of particle 2 at point O . The contact interaction force F during the compressive loading

between particles for elliptical contact area is given by (Johnson, 1987)

$$F = \frac{4}{3} \frac{\sqrt{R_e} E^*}{F_2^{3/2}} \delta^{3/2} = k_e \delta^{3/2}, \quad (5.1)$$

where δ is the relative approach between the distant points of two particles (as explained in Section 1.3.1); the equivalent radius R_e is defined as

$$R_e = \sqrt{(R'R'')}. \quad (5.2)$$

R' and R'' are the principal relative radii of curvature, and they are determined from the principal radii of curvatures of two particles' surfaces at point O by

$$\begin{aligned} R' &= \frac{1}{(A+B)-(B-A)}, \\ R'' &= \frac{1}{(A+B)+(B-A)}, \end{aligned} \quad (5.3)$$

where

$$\begin{aligned} A + B &= \frac{1}{2} \left(\frac{1}{R'_1} + \frac{1}{R''_1} + \frac{1}{R'_2} + \frac{1}{R''_2} \right), \\ B - A &= \frac{1}{2} \left[\left(\frac{1}{R'_1} - \frac{1}{R''_1} \right)^2 + \left(\frac{1}{R'_2} - \frac{1}{R''_2} \right)^2 + 2 \left(\frac{1}{R'_1} - \frac{1}{R''_1} \right) \left(\frac{1}{R'_2} - \frac{1}{R''_2} \right) \cos 2\alpha \right]^{1/2}. \end{aligned} \quad (5.4)$$

The effective contact modulus E^* is given by

$$\frac{1}{E^*} = \frac{1 - \nu_1^2}{E_1} + \frac{1 - \nu_2^2}{E_2}, \quad (5.5)$$

where E_1 , ν_1 and E_2 , ν_2 are the elastic moduli and Poisson ratios of the materials for particles 1 and 2, respectively. In the particular setup studied in this section, $E_1 = E_2$ and $\nu_1 = \nu_2$. The correction factor F_2 depends on the eccentricity of the elliptical contact area e by the following relation:

$$F_2 = \frac{2}{\pi} K(e) \left(\frac{4}{\pi e^2} \sqrt{[(a/b)^2 E(e) - K(e)][K(e) - E(e)]} \right)^{-1/3}, \quad (5.6)$$

where $K(e)$ and $E(e)$ are the complete elliptic integrals of the first and second kind. The eccentricity of the elliptical contact area is given by $e = [1 - (b/a)^2]^{1/2}$, where b and a are the semi-minor and semi-major axes of the elliptical contact area, respectively, and the

ratio b/a can be approximately determined by $b/a \sim (R'/R'')^{-2/3}$.

In the limits of $R'_1 = R''_1 = R_1$ and $R'_2 = R''_2 = R_2$ and $R_1 \equiv R_2$, the ellipsoidal particles become spherical particles, the ratio $b/a \rightarrow 1$, which implies that the contact area is now a circle, and the stiffness k_e in Eq. (5.1) degenerates to k_c in circular contact law Eq. (1.1). Thus, the contact interaction law described by Hertz's model for circular contact area is also a special case of elliptical contact area model (Johnson, 1987). It is important to note that the stiffness k_e in the elliptical contact law is a function of principal radii of curvatures of the particles, and that it also depends on the orientation angle α between the two particles, which is different than the contact interaction between two spherical particles.

For the special case of two identical cylindrical particles of radius R , Young's modulus E , and Poisson's ratio ν in contact with each other, with the angle of orientation between their axes equal to α , the equivalent radius $R_e = \frac{R}{\sin\alpha}$, the effective modulus $E^* = \frac{E}{2(1-\nu^2)}$, and $\frac{b}{a} \approx \left(\frac{1+\cos\alpha}{1-\cos\alpha}\right)^{-2/3}$, respectively. When the orientation between two identical cylindrical particles in contact with each other becomes parallel, the orientation angle $\alpha \rightarrow 0^\circ$ and the contact area reduces to a line. Thus, based on the orientation angle α , the cylindrical particles have three different regimes of contact interaction: (i) a circular contact area for $\alpha = 90^\circ$ governed by Hertzian interaction model for circular area (Eq. (1.1)); (ii) an elliptical contact area for $0^\circ < \alpha < 90^\circ$ described above; and (iii) a very thin rectangular contact area for $\alpha = 0^\circ$. For the third case, one of the assumptions of the elliptical contact interaction model that the semi-major axis is much smaller than the particle's radius, $a \ll R$, under which each particle being considered as an elastic half-space is no longer valid. In this case, the semi-major axis a becomes very large compared to semi-minor axis b , and a can also become larger than or equal to the radius R of the particle, thereby violating the small strains assumption. Therefore, in this case, Eq (5.1) cannot be used because both R_e and F_2 values become undefined. The two particles are required to be fixed at infinity, which leads to an infinite displacement (Puttock and Thwaite, 1969). In the classical book *Applied Elasticity* by Prescott (1946), this case is defined similarly to a load applied on a string which is infinitely long and fixed at one end, such that extension of any load produces an infinite extension. The relative compression δ of

two identical cylindrical particles of radius R under a compressive force F^* , where F^* is the force per unit length, is given by (Johnson, 1987)

$$\delta = 2F^* \frac{1 - \nu^2}{\pi E} \left[2 \ln \left(\frac{4R}{w} \right) - 1 \right], \quad (5.7)$$

where $w = \sqrt{\frac{4F^*R(1-\nu^2)}{\pi E}}$ is the semi-contact width, which also depends on F^* . Eq. (5.7) shows that the line contact interaction is not a linear relation between $F^* - \delta$. Using Lambert W (or omega) function, such that $x = W(y)$ is the solution of $xe^x = y$ (e is mathematical constant $e = 2.718$), the contact force between two parallel cylindrical particles can be represented in terms of the total displacement as:

$$F^* = \frac{\pi E}{1 - \nu^2} \left[\frac{\delta}{2} \frac{1}{W\left(\frac{-e\delta}{8R}\right)} \right]. \quad (5.8)$$

For the general case of power-law type of contact interaction relationship between the two nonconforming particles, the compressive force F for the applied relative displacement δ between particles is given by

$$F = k\delta^n \quad (5.9)$$

where spring constant k and exponent n stay constant during the analysis, and depends on the geometric configurations of the two particles and relative orientation between them

5.2.2 Wave Propagation in a Chain of Non-Spherical Particles with Elliptical Contact Interaction

Using long-wavelength approximations, Nesterenko (1983 2001) showed that, when the granular chains are excited by an impulsive loading—most prominently, when they are uncompressed or very weakly precompressed—they support the formation and propagation of highly nonlinear solitary waves (HNSWs). Using a similar approach, we describe the dynamic behavior of the uniform chains composed of particles, which follows elliptical contact interaction law between neighboring particles. As described above, the potential function of these particles under interaction is of similar nature for both the Hertzian in-

teraction model for circular contact area and for elliptical contact interaction. Therefore, an analogous analytical formulation of Nesterenko's approach for the chains of spherical particles (Section 1.5) also describes the formation and propagation of highly nonlinear solitary waves with identical wave properties in the chains of particles with elliptical contact interaction between neighboring particles, with an equivalent (Eq. (1.9)) nonlinear relation between solitary wave speed V_s and normalized force $f_r = F_m/F_0$.

$$V_s = D \sqrt{\frac{4 k_e^{2/3}}{5 m} F_0^{1/6} \frac{1}{f_r^{2/3} - 1} \left[\frac{3}{2} + f_r^{5/3} - \frac{5}{2} f_r^{2/3} \right]^{1/2}} \quad (5.10)$$

When the chain is uncompressed, Eq. (5.10) reduces to

$$V_s = D \sqrt{\frac{4 k_e^{2/3}}{5 m} F_m^{1/6}}. \quad (5.11)$$

Here D is the particle's size in the direction of the chain. As the power-law relationship $n = 1.5$ for the chain of particles with Hertzian elliptical contact interaction is similar to the chain of spherical particles, the width of the traveling pulse is expected to be ~ 5 times the particles' size.

For the special case of the chain of parallel cylindrical particles such that their axis is perpendicular to the chain and the orientation angle $\alpha = 0^\circ$, the contact interaction law (Eq. (5.8)) is not a power-law formulation; hence, a procedure similar to the Nesterenko's approach for the chain of spherical particles cannot be adopted. For very small values of orientation angle α , the exponent n depends on α , and it can deviate from the value $n = 1.5$. This case will be discussed in the following sections using numerical simulations.

For a general case of chains of granular particles, with the contact interaction given by Eq. (5.9) between adjacent particles, the relation between the wave speed in the system and normalized force is given by (Nesterenko, 2001)

$$V_s = \sqrt{\frac{2}{n+1}} D \left(\frac{k^{1/n}}{m} \right) F_d^{\frac{n-1}{2n}} \quad (5.12)$$

where D and m are the particle's size and mass, respectively, as described above. The

width of the wave traveling in this general power-law interaction system depends on the exponent n as (Nesterenko, 2001)

$$L = \frac{\pi D}{n-1} \sqrt{\frac{n(n+1)}{6}}. \quad (5.13)$$

5.3 Results and Discussions

5.3.1 Chain of Ellipsoidal Particles

The first nonspherical particles considered for the tunability of nonlinear waves by varying the geometrical shape of granular materials were ellipsoidal particles, described in Section 2.1. The tunability of the system and its effects on the wave propagation were analyzed by varying the particle's orientation using the theoretical and numerical approaches. Figure 5.4 shows the FEM of a uniform chain of stainless steel (316 type, Table 2.1) ellipsoidal particles considered, with the orientation angle between the adjacent particles as $\alpha \approx 0^\circ$. The principal radii of curvatures for the surfaces of all the particles can be calculated from the geometry of the individual particles as $R'_1 = R'_2 = (L/2)^2 / (D/2)^2 = 10.93$ mm and $R''_1 = R''_2 = D/2 = 2.36$ mm. We generated the FE model (as described in Chapter 3) of ellipsoidal particles to verify the static and dynamic effects of elliptical interaction on the wave propagation.

To understand the static effects of elliptical contact interaction (Eq. (5.1)), we considered three different cases (Figure 5.3a): (i) two ellipsoidal particles in contact at the tip of their minor axis, such that the orientation angle $\alpha = 0^\circ$ (similar to experimental setup); (ii) two ellipsoidal particles in contact at the tip of their major axis; and (iii) two equivalent spherical particles, i.e., two spheres having the same mass as the ellipsoidal particles and the radius $r = \left[\frac{m_{\text{ellipsoidal particles}}}{\frac{4}{3}\pi\rho} \right]^{1/3}$, in contact with each other. In these simulations, the lower particle was held firm by applying fixed boundary conditions, and the upper particle was given a displacement boundary condition. The displacement applied to the upper particle was small enough (less than 1% of characteristic dimension in each case) to ensure the validity of the small displacements assumption in Hertz's theory. In the

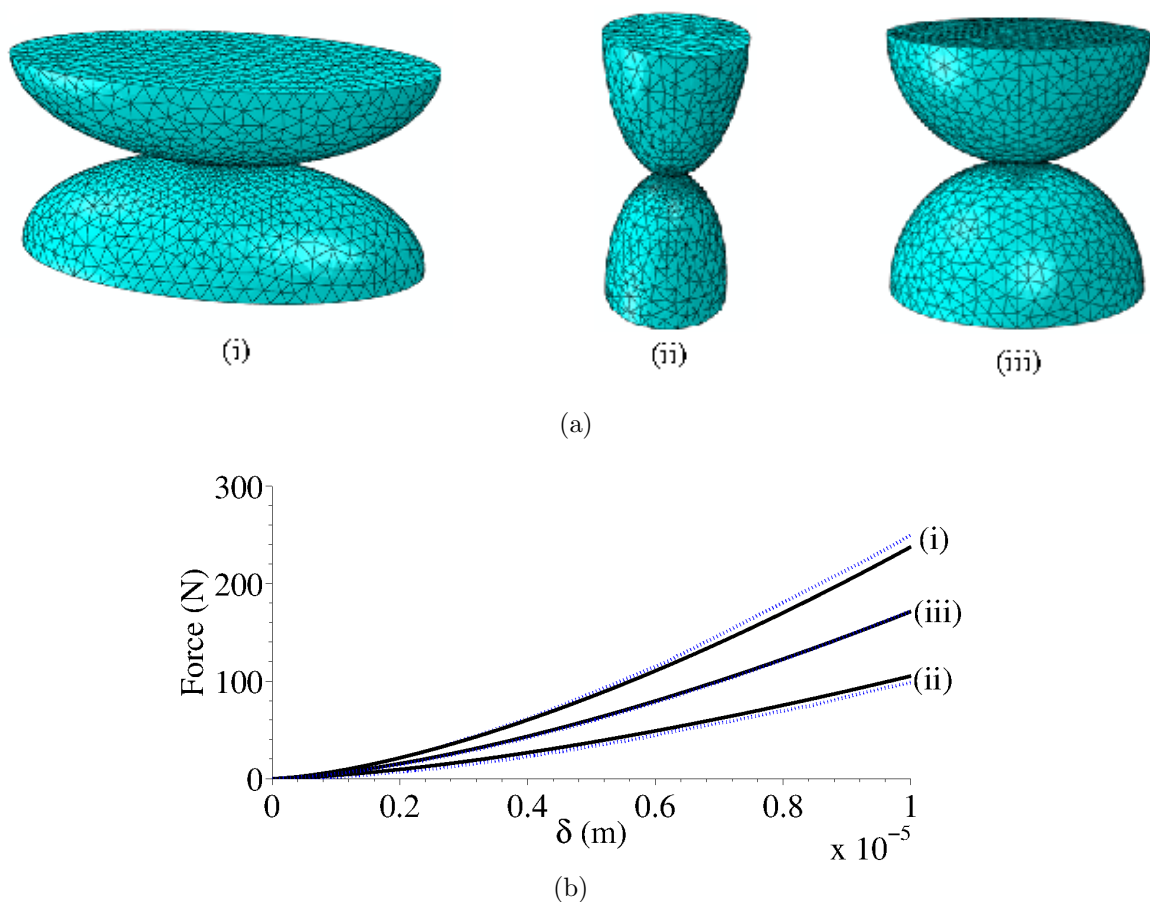


Figure 5.3: (a) Finite element mesh of: (i) two adjacent ellipsoidal particles arranged in the minor axis direction; (ii) two adjacent ellipsoidal particles arranged in the major axis direction; and (iii) two adjacent equivalent spherical particles. (b) Comparison of the contact force-displacement relations between two ellipsoidal particles arranged in minor (curve group (i)) and major (curve group (ii)) axis direction, and also between two equivalent spherical particles (curve group (iii)) obtained from both finite element simulations (dotted (blue) curves) and Hertzian elliptical contact law (solid (black) curves)

range of forces considered in the experiments described in this work, the contact force-displacement relations obtained from FE simulations were in good agreement with the theoretical predictions using the Hertzian elliptical contact law (see Figure 5.3b), and it was found that the force-displacement relationship can be easily tuned over a wide range in the ellipsoidal particles by simply rotating the particles. The theoretical stiffness constant k_e was calculated using Eq. (5.1) and Eqs. (5.2) to (5.6) and found to be for particles aligned along their major and minor axis directions as $3.31 \times 10^9 \text{ N/m}^{3/2}$ and $7.48 \times 10^9 \text{ N/m}^{3/2}$, respectively.

To understand the dynamic effects of Hertzian elliptical contact law on the wave propagation in the chain of ellipsoidal particles, we analyzed two different chains of ellipsoidal particles, with the particles arranged along their major and minor axes, respectively, and compared the obtained results with the chain of equivalent spherical particles (spherical particles having mass equal to ellipsoidal particles). The experimental setup for the chain of ellipsoidal particles was described in Section 2.3. We developed FEM for the chain of particles for the three cases (similar to the model described in Chapter 3) and also solved the problem with DPM, where the particles in the chain were considered as rigid bodies of point masses connected by nonlinear springs, defined by the Hertzian elliptical contact law and a zero tensile response. The spring constant for the two cases of ellipsoidal particles was obtained from the theoretical analysis for both the configurations mentioned above. We performed experiments for a chain of ellipsoids arranged along their minor axis (Figure 5.4b) and measured the force-time response from the instrumented particles (Chapter 2). Figure 5.5a shows the comparison of results obtained from experiments, FEM and DPM, when a chain of ellipsoidal particles with particles arranged along their minor axis was excited with a 316-type stainless steel spherical striker (Dia = 2.38 mm) having an impact velocity of $v_{\text{imp}} = 0.626$ m/s. The results obtained from the three analyses were in good agreement with each other, with the exception of the presence of dissipation in experiments, which confirms that the chain supports the formation and propagation of highly nonlinear solitary waves. We measured the width of the pulse in the three analyses and found it to be ~ 5.5 times the particle's minor diameter, which was analogous to Nesterenko's theory for the chain of spherical particles. The solitary wave speed measured in experiments, DPM, and FEM were 490 m/s, 524 m/s, and 529 m/s, respectively. The small difference in the wave speed was due to the presence of dissipation effects in the experiments, which was evident by the wave amplitude decrease of the traveling solitary wave pulse, and from Eq. (5.10) we know the velocity of solitary wave decreases with the decrease in the wave amplitude.

To further confirm the nonlinear nature of the wave propagating in the chain of ellipsoidal particles, we studied the relationship between solitary wave velocity (V_s) and dynamic loading (F_m), using both the numerical method and theoretical model and verified the results with experiments. The results are in very good agreement with each other and

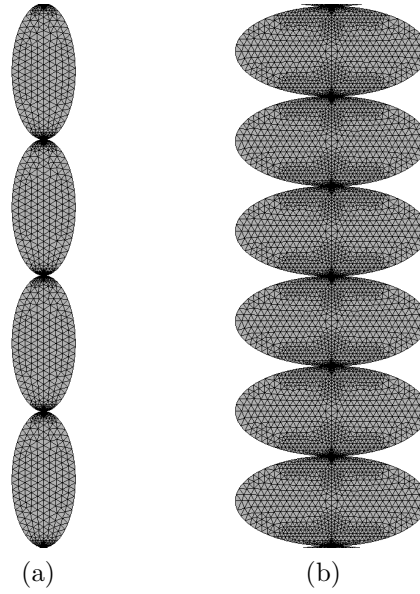


Figure 5.4: Finite element model showing the zoom-in view of a uniform chain of ellipsoidal particles, with the particles aligned along their (b) major axis and (c) minor axis, respectively

show the dependence of wave velocity V_s on loading force $F_m^{1/6}$, which was determined in Eq. (5.11). We also studied numerically the effect of orientation on the chain of ellipsoidal particles aligned along their major axis in the direction of the chain's axis using the theoretical model and both of the numerical methods, and then compared the results from the two cases of particles orientation with the chain of spherical particles with equivalent mass from Eq. (1.10). Figure 5.5b shows the comparison for the three cases. From the results we can conclude that the wave velocity in the chain of particles oriented along their minor axis was slower than the wave velocity in the chain of spherical particles with equivalent mass for the same dynamic loading. This is because the diameter of elliptical particles along their minor axis was smaller than the diameter of equivalent spheres. Similarly, for the chain with ellipsoidal particles oriented along their major axis, the wave speed was faster than that in the chain of equivalent spherical particles.

We also studied the dissipation effects in the ellipsoidal particles chain with particles oriented along their minor axis in the direction of the chain. The experimental setup consists of $N = 50$ particles with $M = 4$ instrumented sensor particles. The wave in the chain was excited using a stainless steel (316 type) spherical particle (Dia = 2.38 mm) with different impact velocities (0.37, 0.49, and 0.66 m/s). The instrumented particles were

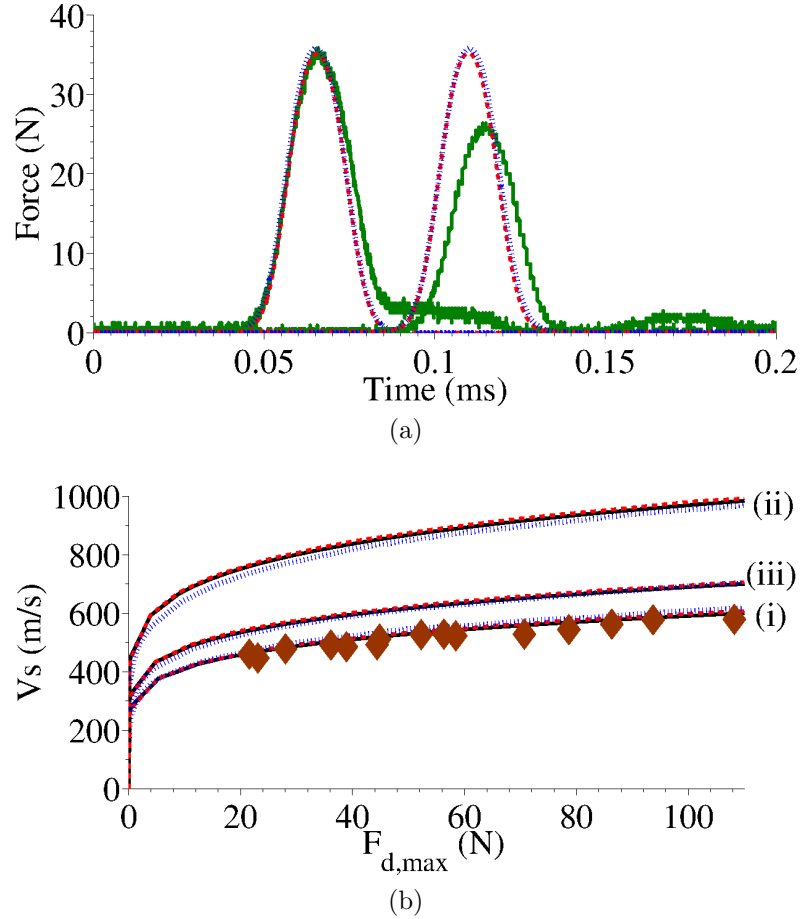


Figure 5.5: (a) Comparison of experiments and numerical results on the formation and propagation of a solitary wave in a chain of 20 stainless steel ellipsoidal particles excited by impacting a stainless steel spherical striker of mass $m = 0.925$ g with an initial velocity of 0.626 m/s. Curve group 1 shows the results for particle 7 in the chain from the top, and similarly, curve group 2 shows the results for particle 12 from the top. Experimental results are shown by solid (green) curves. (b) Dependence of the wave speed on the maximum contact dynamic force in the chains of ellipsoidal particles arranged in both minor (curve group (i)) and major (curve group (ii)) axis directions and in the chain of equivalent spherical particles (curve group (iii)) under gravitational loading. Experimental data for a chain of ellipsoidal particles arranged in minor axis direction are shown by solid (green) diamonds in curve group (iii). The solid (black) curves represent the theoretical predictions. In both panels the dashed (red) curves represent the discrete particle results and the dotted (blue) curves represent the finite element results.

placed at location numbers 8, 16, 28, and 41 in the chain. The modified discrete particle model (Eq. (3.1)) with linear damping γ included was used to study the wave decay. The relaxation coefficient γ for each striker particle velocity case was determined by minimizing the root mean square (RMS) difference between the experimental force amplitude $F_{m,e}$ at each sensor location and the corresponding numerical one. The optimized γ was found to vary from -15.55 to -3.18 in the range of impact velocities tested in experiments. Figure 5.6 shows the wave amplitude decay and pulse shape change as the wave propagates in the chain of ellipsoidal particles and the linear decay model captures the decay trend.

5.3.2 Chain of Cylindrical Particles

In this section, we study the formation and propagation of nonlinear waves in a weakly compressed chain composed of uniform cylindrical particles arranged with their axes perpendicular to the chain's axis. The particles' descriptions are provided in Section 2.1. The cylindrical particles in the chain were arranged such that the relative orientation angle between consecutive particles' axes was α . In Section 5.2.1, we described that the cylindrical particles provide an additional design parameter for controlling the dynamic response of the system, compared to chains of spherical particles or ellipsoidal particles.

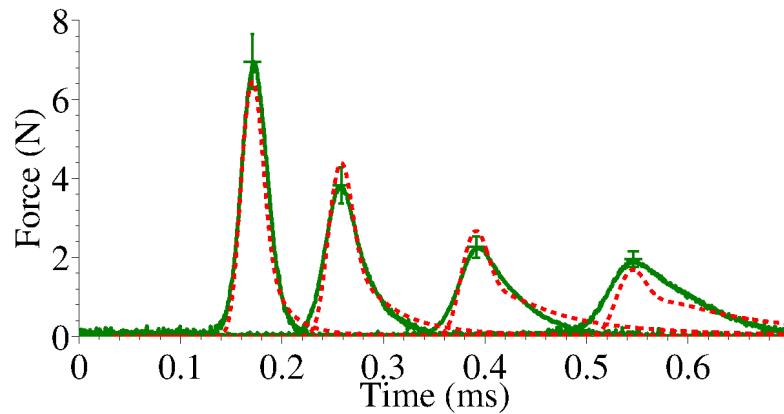


Figure 5.6: Results obtained in a chain composed of 50 ellipsoidal particles, excited by a spherical striker with an impact velocity $v = 0.37$ m/s. The (green) solid curves represent experimental force-time signals obtained from instrumented particles positioned in locations 8, 16, 28, and 41. The (red) dashed curves represent numerical results obtained from a modified discrete particle model with linear damping. γ was the relaxation coefficient and has a value of -11.67 .

In this case, the contact interaction between particles is a function of the relative orientation angle (α) between the particles' axes. Similar to the approach in Section 5.3.1, we used theoretical and finite element models to understand the static interaction between two cylindrical particles and its dependence on angle α . We also analyzed the effect of particles' shape and orientation on the formation and propagation of nonlinear waves in the chain of cylindrical particles using both of the numerical approaches (DPM and FEM), compared the obtained results with theoretical predictions, and verified them with experiments for the simplest case.

In the quasi-static analysis, as described in Section 5.2.1, the cylindrical particles have three different regimes, which are based on the orientation angle α . Figure 5.7a and Figure 5.7b show how the FEM model, consisting of two semi-cylindrical particles, was used for static analysis to understand the different regimes of interaction and to verify the limit of validity for the Hertzian elliptical contact interaction law (Section 5.2.1) when the orientation angle α was varied between two cylindrical particles and when the $\alpha \rightarrow 0^\circ$, respectively. As with the static analysis of spherical particles in Section 3.3.1, the contact process between two identical cylindrical particles were simulated at different relative orientation angles α , ($\alpha \in [0^\circ, \dots, 90^\circ]$). In the simulation, a displacement δ value was applied to the top surface of the upper cylindrical particle, while the lower surface of the bottom cylindrical particle was imposed with fixed boundary condition and, as in Section 3.3.1, the respective contact force obtained from the simulation was observed. The simulation was run for different values of displacement δ , such that in each case the δ applied was much smaller than the particle's diameter (to satisfy Hertz's small displacement assumption (Johnson, 1987)). This process was performed for cylindrical particles for the selected values of relative orientation angles α between the axes of two particles with the value of α in the range of $[0^\circ \leq \alpha \leq 90^\circ]$. Using the power-law fitting ($F = k_{\text{cyl}}(\alpha)\delta^{n(\alpha)}$), the interaction relation (k and n) was determined between the cylinders for the specific case of angle α .

Figure 5.7c shows the variation of contact force as a function of increased displacement between the two particles for different values of orientation angle α , represented by the dashed curves. We also calculated the theoretical responses for each respective regime,

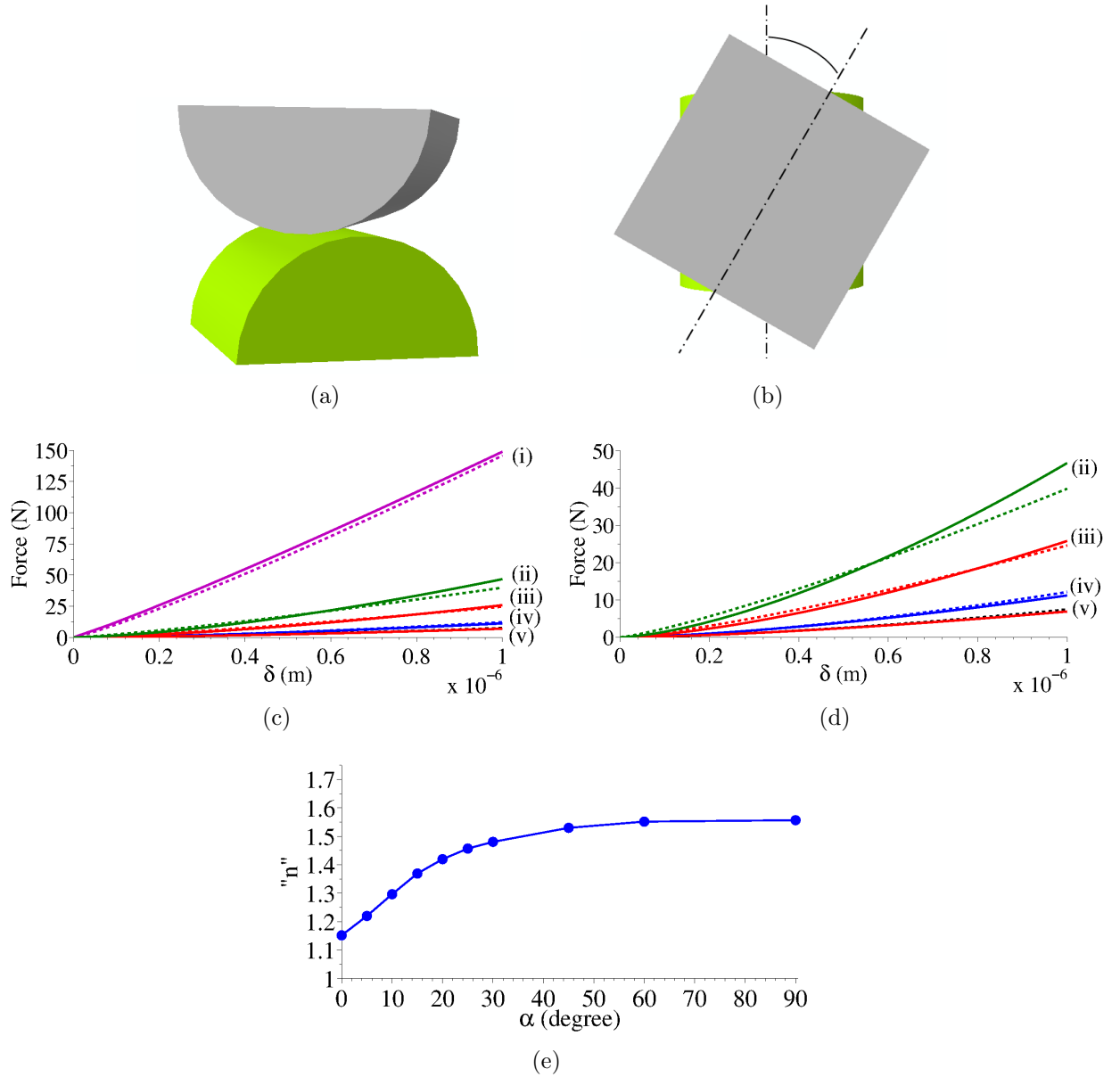


Figure 5.7: (a) Schematic diagram showing isometric view and (b) top view of two cylindrical particles in contact. (c) Comparison of the contact force-displacement relations obtained with the Hertzian contact model (solid curves), and with our finite element model (dashed curves). Results obtained for a contact between two cylindrical particles oriented at a relative angle $\alpha = 0^\circ$ (curve group (i)), $\alpha = 5^\circ$ (curve group (ii)), $\alpha = 10^\circ$ (curve group (iii)), $\alpha = 30^\circ$ (curve group (iv)), and $\alpha = 90^\circ$ (curve group (v)). (d) Detailed view of (c) for $\alpha = 5^\circ, 10^\circ, 30^\circ$, and 90° . (e) Dependence of the exponent n in a generic power-law type contact interaction between two cylindrical particles on the orientation angle α , obtained through finite element analysis

which are represented by the solid curves in the figure. For large orientation angles α , we observed good agreement between theory and numerical results. When the orientation angle α decreased, i.e., $\alpha \rightarrow 0^\circ$, the violation of assumptions used in the theoretical model lead to an evident discrepancy between the curves (see Figure 5.7c and Figure 5.7d). Figure 5.7e shows the value of the exponent n as a function of α obtained from the power-law fitting in FEM. For $\alpha > 30^\circ$, the value of n was close to 1.5, which was expected from the Hertzian contact theory, while for smaller angles $0^\circ < \alpha < 30^\circ$, the exponent n deviates from 1.5, and gradually decreases as the angle decreases. When $\alpha = 0^\circ$, we have a line contact between the two interacting cylinders. For this case, if the contact interaction was approximated by a power-law formulation, we obtained the power-law exponent value $n = 1.15$, which was close to the value 1.11 reported by Harris (2001).

For the dynamic analysis, we tested experimentally the dynamic response of a vertically aligned, one-dimensional chain composed of $N = 20$ uniform cylindrical particles with relative orientation angle $\alpha = 90^\circ$, excited by a stainless steel spherical striker of mass $m = 0.45$ g with an impact velocity $v = 0.5$ m/s (Figure 5.8b). The force profiles measured in time by the sensors positioned at particle numbers 7 and 13 are shown in Figure 5.9a. We compared the experimental data with numerical results obtained with the discrete particle model based on Hertzian contact interactions, and with the three-dimensional FE model, finding very good agreement between them (Figure 5.9a). The solitary wave speeds obtained from the finite element model, discrete particle model, and experiments were 539.2 m/s, 544 m/s, and 559 ± 28 m/s, respectively. The width of the propagating pulses was measured to be 6 particle diameters from experimental data, which was close to the solitary wave's width of 5 particle diameters reported in earlier studies for chains of spherical particles (Nesterenko, 1983 2001).

We studied the relation between wave speed and maximum dynamic contact force in Figure 5.9b. From Figure 5.9b, it is evident that the experimental and numerical results were in good agreement, demonstrating the formation and propagation of highly nonlinear solitary waves. Similar to what was reported for chains of spherical beads (Daraio et al., 2006b; Nesterenko, 2001; Sen et al., 2008), chains of cylindrical particles can be tuned by varying the radius and/or the material properties of the particles, the initial

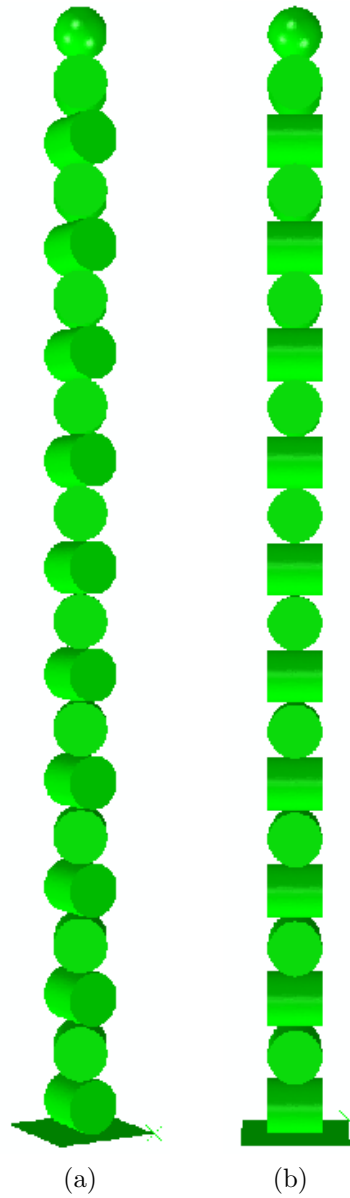


Figure 5.8: Schematic diagram of the cylindrical particles' chain. The chain was composed of 20 elements, stacked vertically. Piezoelectric sensors were embedded in particles at location numbers 7 and 13. The orientation angle α between two adjacent particles in the setup shown is (a) 30° and (b) 90° , respectively.

precompression, and the dynamic force applied to the system. However, the cylindrical geometry of the particles offers an additional parameter for tunability: the orientation angle between consecutive cylinders.

We studied numerically the effect of particle orientation on the wave propagation in the system. Figure 5.9b shows the variation of wave speed as a function of dynamic force for selected values of $\alpha = 30^\circ, 45^\circ,$ and 90° . For a particular orientation angle α , the dynamic force was varied by changing the striker impact velocity. As the α value decreases, the contact stiffness k_{cyl} increases (Eq. (5.1)), which results in higher wave speeds for the same dynamic load (Eq. (5.11)). For example, when the orientation angle between cylindrical particles was $\alpha = 90^\circ$, for the dynamic load of $F_m = 40$ N the wave speed was $V_s = 591.3$ m/s. When the orientation angle was lower than $\alpha = 90^\circ$, the wave speed increased. The speed was 9% higher for $\alpha = 45^\circ$ and 16% higher for $\alpha = 30^\circ$.

The case $\alpha = 0^\circ$ (Figure 5.10) presented unique features: The shape of the propagating waves was significantly different from the cases for which $\alpha > 0^\circ$. The width of these waves, for an impulse generated by a striker of mass $m = 0.45$ g with impact velocity $v_{\text{imp}} = 0.5$ m/s, was ~ 10 particle diameters (see Figure 5.10). The wave speed was ~ 4 times the value observed for other cases, and does not appear to change significantly in the range of dynamic force considered (see Figure 5.10b). This interesting behavior for $\alpha = 0^\circ$ originates from the fact that the contact interaction does not have a power-law type relation (see Section 5.2.1).

Using FEM, we studied the sensitivity of the system towards the small angle variation near $\alpha = 0^\circ$ (Figure 5.10b). From the FEM results, we found that the dynamic response of this system is very sensitive to the change in the orientation angle, i.e., the wave speed changes significantly with small changes in the value of α . Because of the imperfect nature of the experimental setup (e.g., the non-uniformity of the particles, especially the sensor particles, and the tolerances between the particles and the support system) the measurements of the wave propagation in a chain of cylinders with small α presented significant variability. From the FEM analysis and discrete particle simulations, we found that the wave speed in the chain of cylindrical particles increased dramatically as the orientation angle is decreased for a given dynamic force. The solid (blue) curve with star

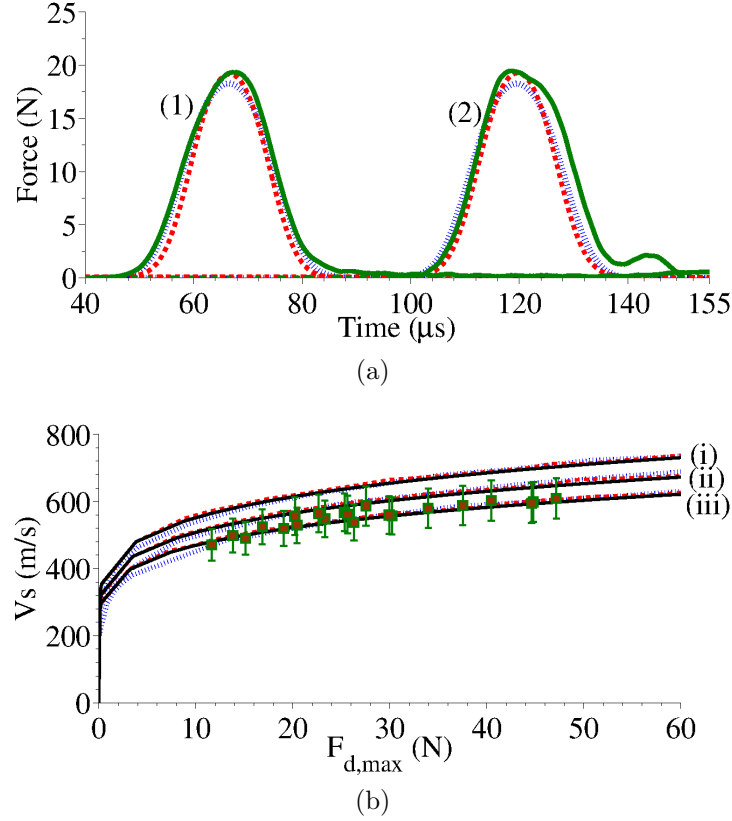


Figure 5.9: (a) Comparison of experimental and numerical results, obtained from the finite element and discrete particle models, for the wave propagation in a chain of cylindrical particles with orientation angle $\alpha = 90^\circ$. The results obtained from the instrumented particles placed at location numbers 7 and 13 from the top of the chain are represented by curve groups (1) and (2), respectively. The solid (green) curves represent experimental data. The dashed (red) curves are obtained from our discrete particle model, and the dotted (blue) curves from FEM. (b) Dependence of solitary wave speed on the maximum dynamic contact force in the chain of cylindrical particles when $\alpha = 30^\circ$ (curve group (i)), when $\alpha = 45^\circ$ (curve group (ii)), and when $\alpha = 90^\circ$ (curve group (iii)). Experimental data are reported only for $\alpha = 90^\circ$, and are shown by solid (green) squares. The theoretical results for all of the angles in each group are shown by solid (black) curves. The results obtained with our discrete particle model are represented by the dashed (red) curve, and the finite element results are represented by the dotted (blue) curves in each group.

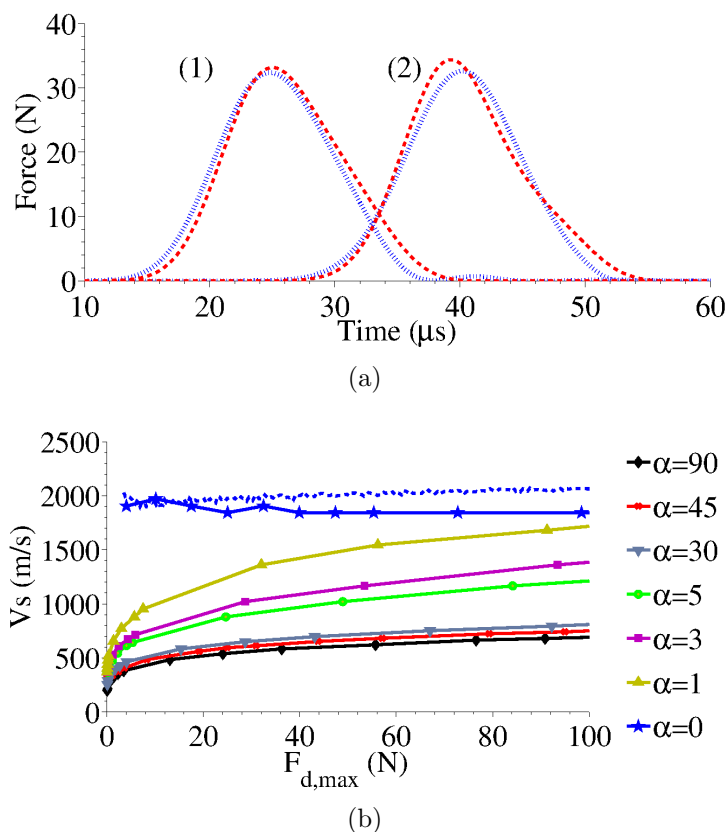


Figure 5.10: Numerical results showing the dynamic response of a chain composed of parallel cylinders ($\alpha = 0^\circ$). (a) Force profiles in time obtained for a wave traveling in a chain of parallel particles using our finite element model (dotted (blue) curves) and our discrete particle model (dashed (red) curves). Curve groups (1) and (2) represent results obtained for the waves traveling through the 7th and 13th particles from the top of the chain. (b) Dependence of wave speed on the maximum dynamic contact force. The solid lines represent results obtained with our FEM for different values of the relative orientation angle $\alpha = [0^\circ, 1^\circ, 3^\circ, 5^\circ, 30^\circ, 45^\circ, 90^\circ]$. The dotted line, shown for $\alpha = 0^\circ$, reports data obtained with the DPM.

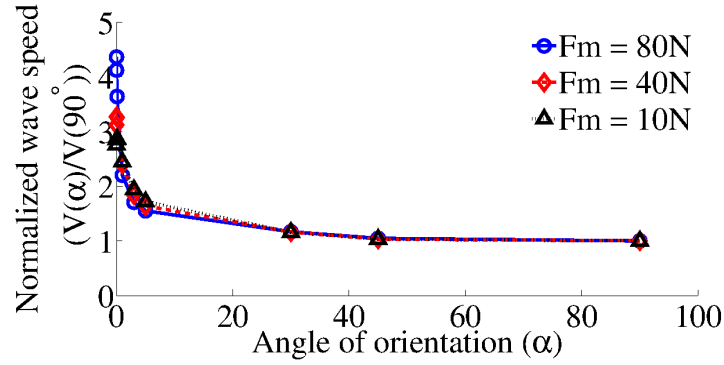


Figure 5.11: FEM results showing the dependence of the wave speed (normalized with respect to the wave speed in the case $\alpha = 90^\circ$) as a function of the orientation angle α . The three curves correspond to three different dynamic force values: the solid (blue) curve with circular markers is for $F_m = 80\text{ N}$; the dashed (red) curve with diamond markers corresponds to $F_m = 40\text{ N}$; and the dotted (black) curve with triangular markers is for $F_m = 10\text{ N}$.

markers and the dotted (blue) curve in Figure 5.10b represent results obtained with the FEM and the DPM, respectively. The angle of orientation has a significant effect on the solitary wave speed as $\alpha \rightarrow 0^\circ$. In Figure 5.11, we calculated the normalized solitary wave speed (with respect to the wave speed in case of $\alpha = 90^\circ$) as a function of α for selected values of dynamic force. From this figure it appears clear that in the range of small α ($0^\circ < \alpha < 10^\circ$), the wave speed changes significantly with small changes in α , while in the range of large values of α , the wave speed is not very sensitive to the changes in angle of orientation.

5.3.3 Chain of Hollow Spherical Particles

In this section, we explore the effects of the spherical particles' wall thickness on the formation and propagation of highly nonlinear solitary wave. (Updike and Kalnins, 1970 1972) theoretically studied coupling between a thin hollow hemi-sphere and a rigid plate. In their study, they used the semi-analytical approach to determine the compression force-displacement relation between hollow sphere and rigid plate. They also described the conditions for the buckling of the control region based on critical deformation of the flattened region, and found that the material can be assumed linearly elastic throughout the deformation until buckling. Pauchard et al. (1997) and Pauchard and Rica (1998)

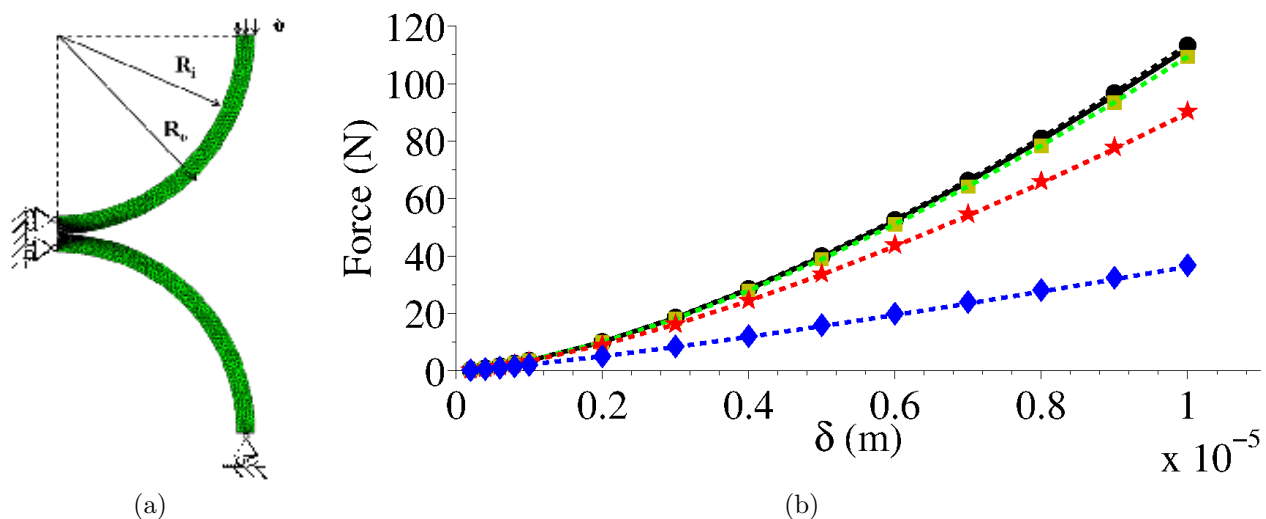


Figure 5.12: a) Schematic diagram showing the axial symmetric FEM of two hollow spheres in contact with symmetry and boundary conditions. (b) Contact interactions obtained from FE simulations for selected values of $R_i/R_o = 0$ (curve (i) in black), $= 0.5$ (curve (ii) in green), $= 0.75$ (curve (iii) in red), $= 0.91$ (curve (iv) in blue). The makers represent the FE results, the dashed curves are the power law fittings of the FE results. The solid black curve is obtained from the Hertzian contact interaction between two solid spheres of the same radius R_o .

studied the deformation of a thin elastic shell in different situations. They developed an analytical formulation to describe the effect of the restitution coefficient on the energy loss and related the elastic energy to the displacement. They also verified their work with experiments and found good agreement with their model. [Audoly and Pomeau \(2010\)](#) provide more detail on this problem. [Ruan et al. \(2006\)](#) did a detailed experimental and numerical study on thin-walled spheres and sphere arrays using ping-pong balls. They also studied the bifurcation phenomena for two ping-pong balls in compression and used load-deformation relation for predicting the crushing behavior of one- or two-dimensional arrays of ping-pong balls, then verified them with experiments. However, a general contact interaction model, similar to Hertz's model for spherical particles (Section 1.3.1), which can describe the deformation process of hollow spherical particles was not available. Thus, the contact interaction behavior was obtained by assuming a power-law-type relation $F = k\delta^n$ between the hollow spherical particles and by using the quasi-static FE simulations to determine the coefficients (k and n), with the assumption that the material stays in linear elastic range and there is no buckling. The interaction law thus obtained was used to study the wave propagation in the chain of hollow spherical particles for different shell thickness.

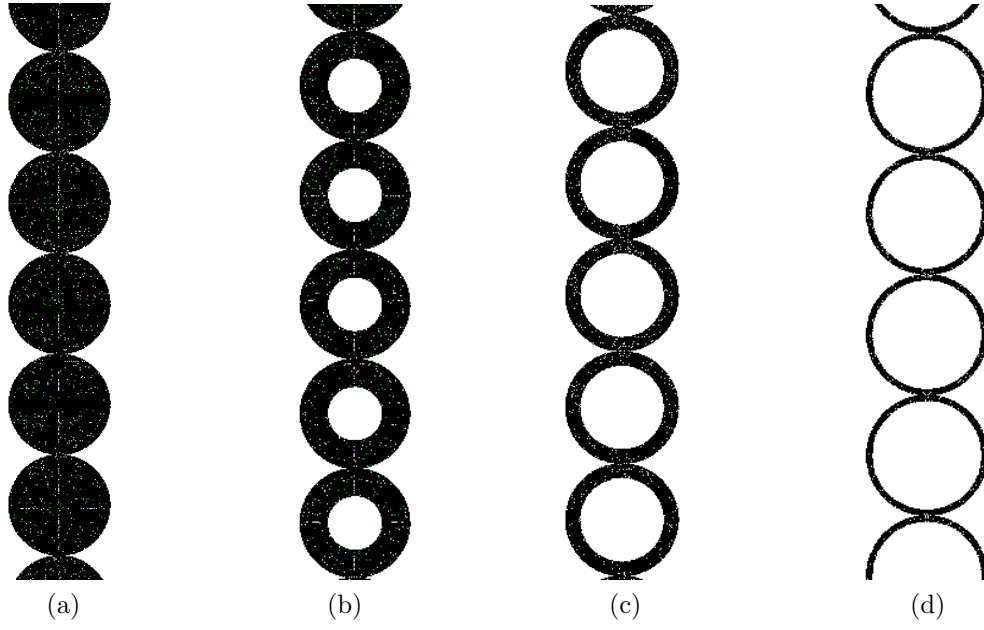


Figure 5.13: Schematic diagram of the chain composed of 20 hollow spherical particles, with piezoelectric sensors embedded in particles at location numbers 7 and 13. The radius ratios R_i/R_o for the chain considered were (a) 0, (b) 0.5, (c) 0.75, and (d) 0.908, respectively.

In our experiments, we selected uniform aluminum hollow spherical particles with outer radius $R_o = 9.525$ mm and $R_i/R_o = [0, 0.908]$, where R_o and R_i are the outer and inner radii of the particle, respectively. The description of the particle's geometry and material values is provided in Section 2.3. The quasi-static FEM (Figure 5.12a) was generated in Abaqus/CAE to obtain the contact interaction relationship as a function of wall thickness. Similar to the process described in Section 3.3.1, the model for hollow spherical particle interaction used in this study consisted of two axisymmetric hemi-spherical particles (Section 3.2.3) such that the lower surface of the bottom particle was imposed with fixed displacement boundary condition and the top surface of the upper particle was applied with known displacement δ . Using the logarithmic fitting for the obtained contact force between the two particles and the applied displacement, we obtained a generalized contact interaction relationship, i.e., contact stiffness k and exponent n , for two hollow spherical particles in contact. The analysis was performed for four different sets of hemi-spherical particles with $\frac{R_i}{R_o} = 0, 0.5, 0.75,$ and 0.908 , while keeping the outer radius fixed and equal to the particle's radius used in the experiments, $R_o = 9.525$ mm. Table 5.1 presents the value of coefficient obtained from FEM for the four cases. For the hollow

R_i/R_o	k	n
0	3.759E9	1.504
0.5	3.193E9	1.493
0.75	1.174E9	1.423
0.908	4.671E7	1.222

Table 5.1: The values of the contact stiffness k and the exponent n obtained from FE simulations for selected values of R_i/R_o

spherical particles selected in experiments $R_i/R_o = 0.908$, the exponent value obtained from FEM was $n = 1.22$, which is in excellent agreement with the value $n = 1.2$ provided by [Pauchard and Rica \(1998\)](#) for the case of contact interaction between a tennis ball (with the ratio $R_i/R_o = 0.9$) and a rigid plate.

Figure 5.12b shows the variation and dependence of contact interaction on the wall thickness. As the thickness of the particles decreases, i.e., the inner radius R_i becomes larger and the repelling force generated by the surface decreases for the same value of displacement δ applied. For the range of the force considered in our analysis, the power-law relationship provided a satisfactory approximation of contact interaction between hollow spherical particles.

Since the contact interaction was assumed to be a power-law relationship, and therefore to follow an argument similar to that explained above for the chain of ellipsoidal and cylindrical particles (Section 5.2.2), the chain of hollow spherical particles under dynamic excitation supports the formation and propagation of nonlinear waves. The experimental setup consisted of uniform $N = 29$ aluminum hollow spherical particles of $R_i/R_o = 0$ and 0.908, respectively, as explained in Section 2.3. Two respective instrumented particles ($M = 2$) were used at location numbers 12 and 19 in each chain and the wave in the system was excited with a particle identical to the other particles in the chain as striker. The wave analysis in the chain, using theory and DPM, was performed using the Hertzian interaction law, whereas for the hollow spherical particles $\frac{R_i}{R_o} = 0.5, 0.75, \text{ and } 0.908$, the theoretical analysis (Section 5.2.2) and discrete particle model (Section 3.1) were performed using the interaction relation obtained from FEM simulations (Table 5.1).

Figure 5.14a compares the wave profile of a traveling pulse in the chain with $R_i/R_o = 9.525$ mm through two instrumented particles for the striker impact velocity $v_{\text{imp}} = 0.32$

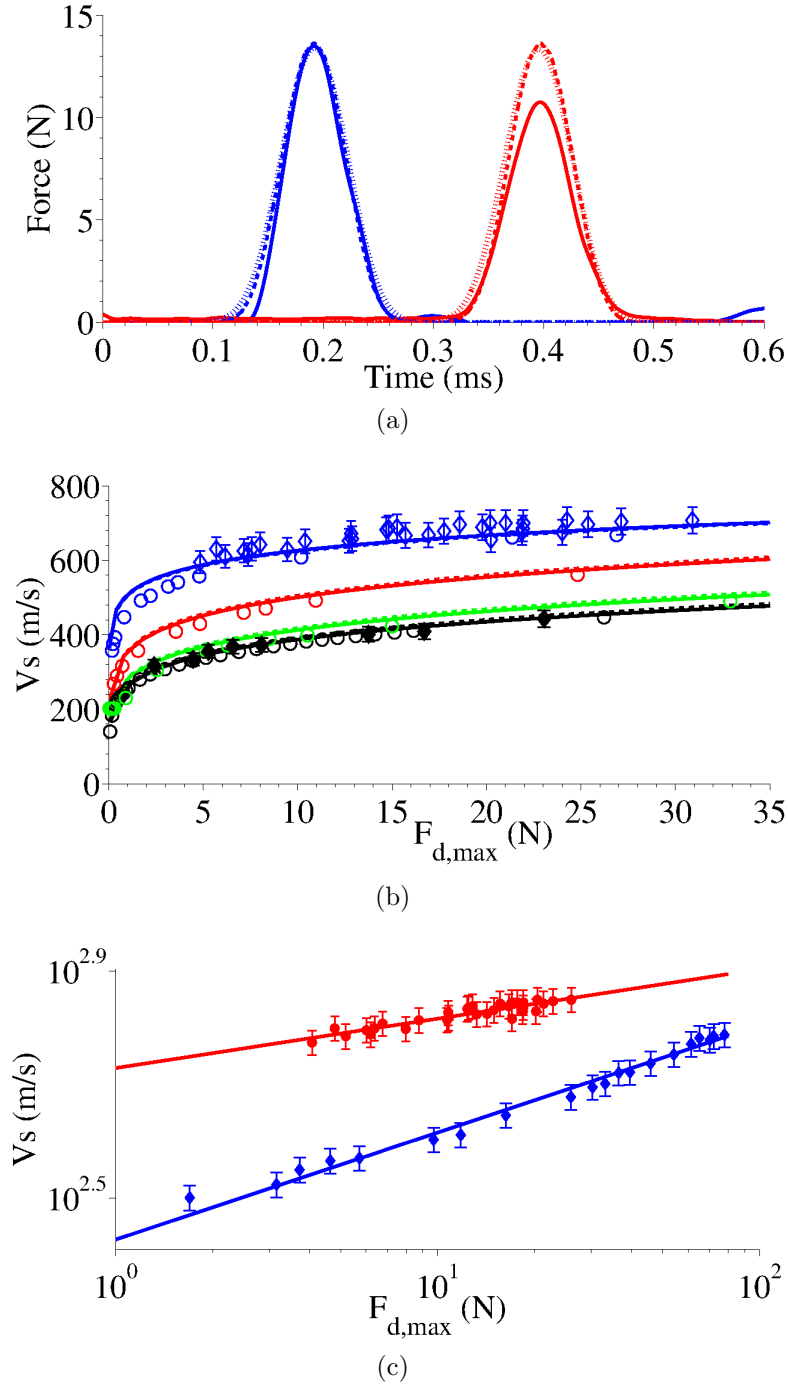


Figure 5.14: (a) Comparison of experimental and numerical results, obtained from discrete particle and FE simulations, for the wave propagation in a chain of hollow spheres with $R_i/R_o = 0.91$. The curve group (1) in blue represents the results obtained at particle 12, the curve group (2) in red represents the results obtained at particle 19. The solid curves represent experimental data. The dashed curves are obtained from FE simulations, and the dotted curves from DP simulations. (b) Dependence of solitary wave speed on the dynamic force amplitude in the chain of hollow spheres when $R_i/R_o = 0$ (curve group (i) in black), when $R_i/R_o = 0.5$ (curve group (ii) in green), when $R_i/R_o = 0.75$ (curve group (iii) in red), when $R_i/R_o = 0.91$ (curve group (iv) in blue). Experimental data are reported only for $R_i/R_o = 0.91$, and they are shown by solid diamonds. The theoretical results in each group are represented by solid curves. The results obtained with our discrete particle model are represented by dashed curves and the finite elements results are represented by circles. (c) Comparison of logarithmic scaling of wave velocity-force relation for the chain of hollow spherical particles, $R_i/R_o = 0.908$, with the chain of solid spherical particles, $R_i/R_o = 0.0$.

m/s. The wave speeds obtained from the three approaches (discrete particle model, finite element model, and experiments) were 648.5 m/s, 642.2 m/s, and 644.7 ± 32.2 m/s, respectively. From the theoretical analysis (Eq. (5.13)), the expected wave width for contact interaction relation with $n = 1.22$ (Table 5.1) was 7.5D, which is in close agreement with the value of 9.5D obtained from the experiments. To further confirm the nonlinear relationship (Eq. (5.12)) and wave support over a wide range of dynamic force, we compared the velocity-force scaling in Figure 5.14b. The results obtained from theory, DPM, and FEM were in excellent agreement with experimental findings, showing the formation and propagation of nonlinear waves in the chain of hollow spherical particles, and also confirmed our assumption of a power-law relationship for contact interaction between hollow spherical particles.

Figure 5.14c shows the comparison of logarithmic scaling of wave velocity-force relation for the chain of hollow spherical particles, $R_i/R_o = 0.908$, with the chain of solid spherical particles, $R_i/R_o = 0.0$. The chain of solid spherical particles supports the highly nonlinear solitary waves with the velocity-force relation given by $V_s \propto F_d^{1/6}$ (Eq. (1.10)), whereas the expected relationship for $n = 1.22$ in the chain of hollow spherical particles from Eq. (5.12) is $V_s \propto F_d^{1/12}$, which was confirmed by the experimental results.

Using numerical and theoretical approaches, we investigated the effect on the wave dynamics of variation in the wall thickness of the hollow spherical particles. From the above discussion of variation in contact interaction between two identical hollow spherical particles (Table 5.1), by changing the wall thickness of the particles we can predict the change in the wave behavior in the respective chains. These wave propagation phenomena were corroborated by the variation in the wave width (decreases with the increase in wall thickness) from Eq. (5.13), and the wave velocity from Figure 5.14b (increases with the increase in wall thickness), where we compared numerically and theoretically four different cases of wall thickness ($\frac{R_i}{R_o} = 0, 0.5, 0.75, \text{ and } 0.908$) and verified those results from experiments for the two extreme cases.

Chapter 6

Coupling of Nonlinear Media with Linear Media

One of the potential application of HNSWs proposed by our group is the use of nonlinear granular media as an actuator system for Non-Destructive Evaluation/Structural Health Monitoring (NDE/SHM) of structure (Daraio and Rizzo, 2008; Eggenpieler et al., 2008; Khatri et al., 2008 2009). In the conventional NDE/SHM work, several methods, such as electro-mechanical impedance (EMI), structural mechanical impedance (SMI), and impact-echo technique are used. The impact-echo technique (Nicholas, 2001) is one of the most commonly used methods in NDE/SHM. In this method, the stress waves are impacted in the system and the echo, or group of reflected waves, generated by the system is observed for defects, flaws, and other external surface parameters. The method is even approved by ASTM (ASTM Standard C 1383 - 04(2010)) for thickness measurements of concrete slabs and plates. Usually in this method, low-frequency stress waves (up to 80 kHz) are generated by tapping the system with a small steel spherical particle. The tapping produces the waves inside the specimen, and, because of the superposition of internal reflections, the local vibrational modes of specimen are excited. These modes are recorded by transducers mounted on surfaces. The dominant frequencies in the spectrum correspond to the natural frequencies of the specimen or the defects. In the EMI methods, a piezoelectric ceramic lead zirconate titanate (PZT) is used as a damage indicator. These methods use pattern recognition techniques, whereby the impedance signature is taken at various time intervals and compared. For identifying damage detections, signature

patterns are monitored for changes. Most of the conventional linear wave methods for NDE/SHM require an arbitrary function generator or other electronic equipment. They are susceptible to the response of piezoelectric crystals and other transduction mechanisms. On the contrary, as mentioned in previous chapters, the generation of HNSWs does not rely on bulky electronic equipment; they can be tuned over a wide range and adjusted for specific applications, and their high degree of reproducibility in experiments makes them an attractive potential substitute as a nonlinear actuation/receiver system in NDE/SHM.

A considerable amount of work has been done to understand the wave reflections and scattering at the interface of two granular media (Nesterenko et al., 2005; Vergara, 2005 2006). Hong and Xu (2002) found that the presence of impurities in a granular chain leads to the decomposition of incident solitary waves in the backscattered signals due to soliton confinement. They correlate the backscattered signal behavior on the nature of impurity present in the chain, i.e., light or heavy. Nesterenko et al. (2005) studied the reflection of waves from the interface of two granular media in a heterogeneous chain. They found that the reflection and transmission of energy at the interface of two nonlinear media also depend on the initial precompression and named the phenomenon “acoustic diode”. Reflection and localization of solitary waves with a rigid wall and elastic walls of various hardness has also been studied in the past (Job et al., 2005; Manciu and Sen, 2002). E. Falcon et al. (1998ab) studied experimentally and numerically the bouncing behavior of one bead and also of a column of N beads ($N \leq 40$) on a fixed wall. They studied the effect of restitution coefficient on the bouncing of a single bead and found that the value stays constant until the bead impact velocity decreases to zero. For the column of beads falling on the wall, they discovered that the force felt by the wall is independent of the number of beads N in the column for a rigid wall, whereas, for a soft wall, it depends on N . Job et al. (2005) studied the wave shape and wave localization at the interface between granular media and elastic wall media. They characterize the change in wave profile of reflected waves from the interface between granular chains and various elastic walls with different hardnesses. Nevertheless, the complete knowledge of coupling between nonlinear granular media with adjacent linear elastic media is still lacking, and because of this, combined with the fact that many of the potential test specimens can be

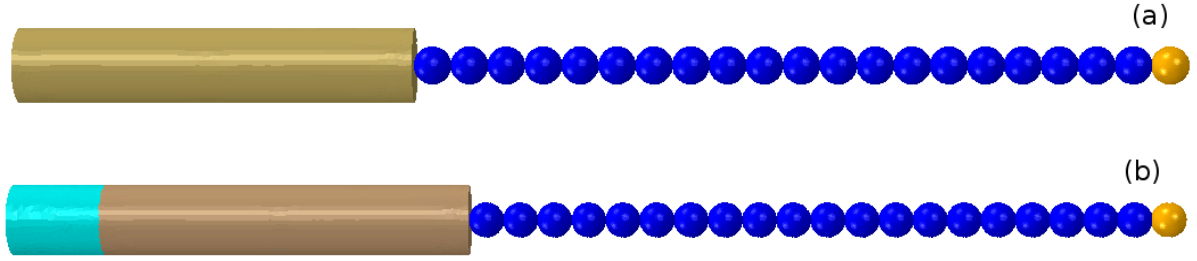


Figure 6.1: Finite element model for coupling of one-dimensional chain composed of 20 spherical particles with adjacent linear elastic media: (a) a uniform single-layer linear elastic media; and (b) a composite double-layer linear elastic media. The bottom of the linear media was under fixed boundary conditions

considered as linear elastic media, we were motivated to perform a comprehensive study of the interaction of highly nonlinear granular media with adjacent linear elastic media. We did a detailed study (theoretically, numerically, and experimentally) to understand the interface dynamics and found that the wave reflections, scattering, and localization at the interface of granular media and specimen are highly sensitive to the coupling of the two media (Yang et al., 2011b). This chapter explains the detailed analysis and reports the findings of this work.

6.1 Interaction of Highly Nonlinear Waves with an Adjacent One-Dimensional Linear Medium

The experimental setup and the material properties of the specimen tested in this study are explained in Section 2.4. The system had $N = 20$ uniform stainless steel 440C type particles of radius $R = 4.76$ mm arranged in a vertical column and placed on top of cylindrical samples. The effect of adjacent linear elastic media as a wall boundary condition to the granular media can be categorically understood using the one-dimensional wave propagation assumptions for four different cases:

1. Effects of the linear media:
 - (a) Effects of the linear medium stiffness.
 - (b) Effects of the linear medium geometry.

2. Effects of the layered (two-layer) composite media:

- (a) Effects of variable thickness of the top layer.
- (b) Effects of variable thickness of the lower layer.

The first two cases (1(a) and 1(b)) were helpful in understanding the basic effect of a single-layered adjacent wall media, where we systematically varied the material property and length of the cylindrical samples, respectively. We analyzed the effect of variation by monitoring the characteristics of the reflected and backscattered waves, which were formed at the interface of granular and linear media. The next two cases (2(a) and 2(b)) explain the effect of interaction between granular media and composite media. For simplicity, we considered composite media with two layers only, but the approach developed here can be extended to multi-layered structures using a similar understanding.

We extended Nesterenko's model (Section 1.5) for wave propagation in the chain of granular particles to include the interface dynamics of nonlinear media with linear elastic media. The model takes into account all of the assumptions of one-dimensional quasi-static analysis used for incident wave propagation in the chain of granular particles. To restrict the analysis to one dimension (the simplest case of coupling behavior between two media), we used cylindrical specimens as linear elastic media. When the axisymmetric cylindrical samples are placed adjacent to the granular chain such that the axis of the cylinder is in line with the axis of the chain, we can neglect the flexural deflections and use the one-dimensional wave propagation theory for the linear elastic media.

$$m\ddot{u}_n = (A_n\delta_n^{3/2} - A_{n+1}\delta_{n+1}^{3/2}) + (\gamma_n\dot{\delta}_n - \gamma_{n+1}\dot{\delta}_{n+1}) + F \quad (6.1)$$

$$A_n \equiv \begin{cases} A|_c = \frac{E\sqrt{2R}}{3(1-\nu^2)}, & n \in \{1, \dots, N\} \\ A|_w = \frac{4\sqrt{R}}{3} \left(\frac{1-\nu^2}{E} + \frac{1-\nu_w^2}{E_w} \right)^{-1}, & n = N+1 \end{cases} \quad (6.2)$$

$$\gamma_n \equiv \begin{cases} \gamma|_c, & n \in \{1, \dots, N\} \\ \gamma|_w, & n = N+1 \end{cases} \quad (6.3)$$

$$\delta_n \equiv \begin{cases} [u_{n-1} - u_n]_+ & n \in \{1, \dots, N+1\} \end{cases} \quad (6.4)$$

As described in Section 1.5, u_n is the displacement of the n^{th} particle's center from its equilibrium position, and R , E , and ν are the particle's radius, elastic modulus, and Poisson's ratio, respectively. The A_c and γ_c are the stiffness constant and the dissipation coefficient in the chain between particles, i.e. particle-particle interaction, respectively. F is the body force applied on the chain, i.e., gravity in our case. The bracket $[s]_+$ gives the value s if $s > 0$, and equal to 0 if $s < 0$.

The $n = N+1$ represents the wall coordinate at the interface and u_{N+1} is the displacement of the linear media at the interface. For a perfectly rigid wall, $u_{N+1} = 0$ and for a linear media adjacent to a granular chain, the value of u_{N+1} is determined from the equation of motion and boundary conditions. The subscripts $|_c$ and $|_w$ refer to the chain and wall, respectively. Thus, E_w and ν_w represent the mechanical properties of the wall. $A|_w$ represents the stiffness constant between the last particle in the chain and the adjacent wall media, and from Eq. (6.2) we can see that it is different than the contact stiffness between particle-particle interaction $A|_c$. Based on our study on wave dissipation in the granular chain (Chapter 4), we accounted for energy losses by modeling the effect of dissipation in the chain and the interaction of the last particle with the wall using the relative velocities between the nodes and restitutional losses, respectively. Since we used a shorter chain ($N = 20$ particles), the linear dissipative model was able to capture the energy losses during the wave propagation and interaction, which was verified with experimental results. The dissipation coefficient $\gamma|_c$ and the wall damping coefficient $\gamma|_w$ at the interface were extrapolated from experiments. Both $A|_w$ and $\gamma|_w$ depend strongly on the property of the last particle in the chain N and the wall media.

6.1.1 Effects of the Linear Media's Stiffness

We performed numerical simulations using one-dimensional assumptions in the discrete particle model and verified these assumptions with the three-dimensional finite element model, theoretical predictions, and experimental results. To understand the effect of linear media's stiffness on the interface dynamics, we varied the wall's (cylindrical specimen) elastic modulus over a wide range of two orders of magnitude from 1.53 GPa (PTFE) to 200 GPa (stainless steel). The striker impact velocity was kept identical for various specimens in all the different approaches (DPM, FEM, experiments), thereby generating an identical incident solitary wave for all of the cases. The experimental results showing the force profile obtained from the instrumented sensor particle placed at location number 7 in the chain for the two extreme cases of the cylindrical specimen's elastic modulus, "hard" (when the $E_{\text{particle}} \approx E_{\text{wall media}}$, here wall media was a stainless steel cylinder) and "soft" (when the $E_{\text{particle}} > E_{\text{wall media}}$, here wall media was a PTFE cylinder), are shown in Figure 6.2. The first pulse is the incident solitary wave and the remaining pulses are the reflected solitary waves generated from the interface of two media. From Figure 6.2, we can see that the responses of the granular media for the two cases of adjacent media are very different. In our analysis, we referred to the first reflected solitary wave for both hard and soft wall media as the primary solitary wave (PSW), and to the second reflected solitary wave as the secondary solitary wave (SSW). We used the particle dynamics to understand the change in granular media behavior during the interaction from single reflected wave for the hard wall to multiple reflected waves for the soft wall.

A 3D-FEM model was also generated to simulate the interaction between chain of particles with linear elastic wall boundary condition, in this case cylindrical specimen. The particles in the chain were modeled as described in Chapter 3, and the appropriate contact definition between them was applied. The cylindrical specimen were modeled with second order tetrahedral elements, modified 10-node C3D10M, in the vicinity of the contact with the particle N and with 8-node hexahedron hybrid stress element away from the contact zone. The hybrid stress element provides good result in the finite element analysis with coarse mesh. The simulations were performed for various sample of cylindrical specimen as used in the experiments and their material properties was used as per Section 2.1. An

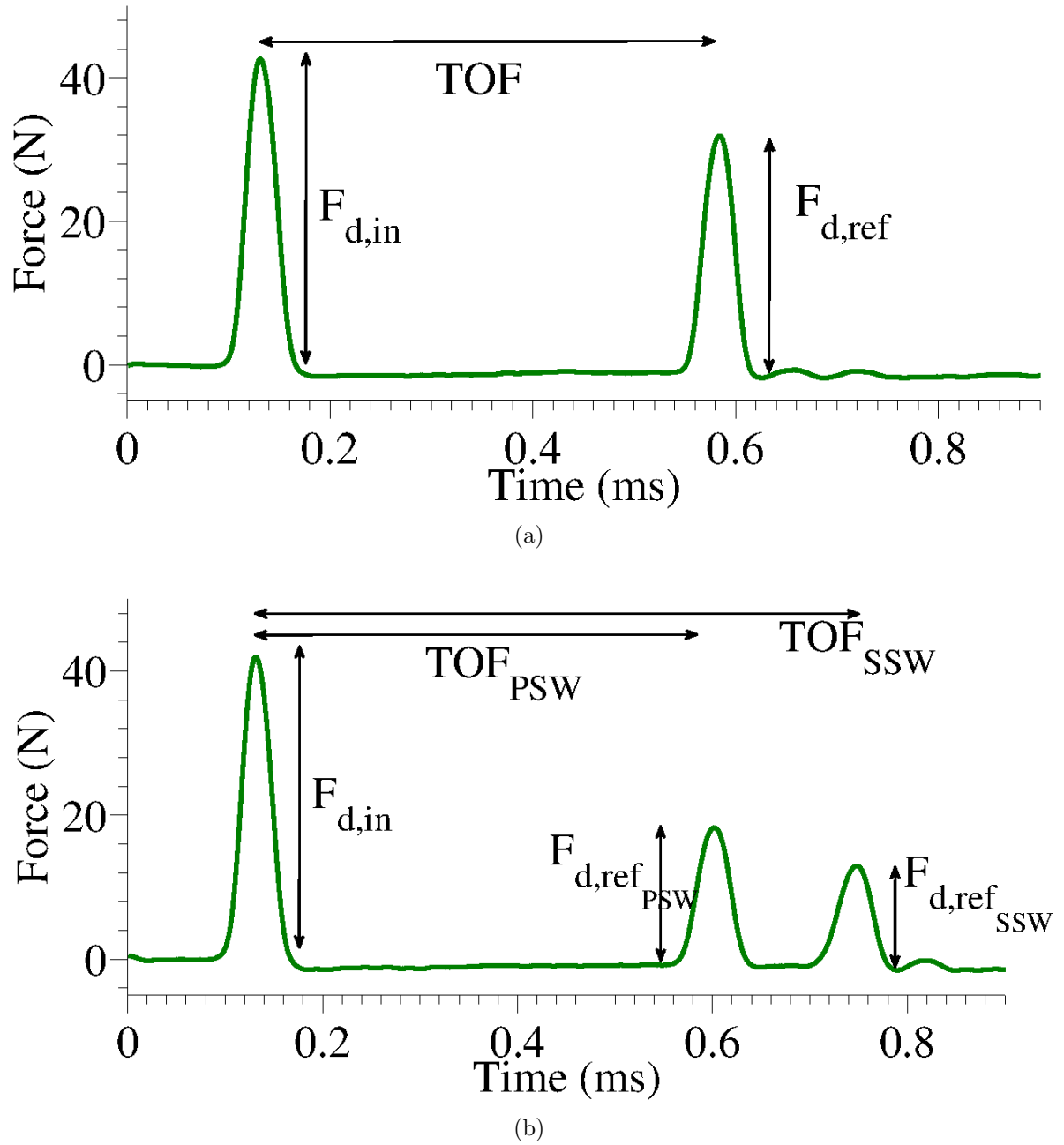


Figure 6.2: Solitary wave propagation measured from the 7th bead in the chain against (a) stainless steel wall and (b) PTFE wall. In (b) the arrival of the primary reflected wave (PSW) is significantly delayed and the generation of a secondary solitary wave (SSW) is clearly observed. The delay time between the incident and the reflected waves is represented by the time of flight (TOF), which is the transit time between the incident and the reflected solitary waves.

axisymmetric model was also generated to simulate a semi-infinite half space wall boundary condition. The goal was to avoid the effect of any reflected waves originating from the internal boundaries of the specimen. For this model, the particles were modeled as described in Section 3.2.3 using triangular six-noded modified quadratic axis-symmetric elements (CAX6M). Half space was also modeled with similar elements in the vicinity of contact zone and with an infinite boundary conditions on the far end to avoid the reflection of waves.

To understand the characteristics of the reflected waves for different values of elastic moduli of the bounding media (Figure 6.4), we measured amplitude ratio (AR) and time of flight (TOF) of the reflected waves. The AR of the reflected waves is defined as the ratio of reflected wave amplitude with respect to the incident wave amplitude at the instrumented particle, i.e., $(F_{d,ref}/F_{d,in})$, where F_d is the maximum dynamic force amplitude between the particles, and subscripts “in” and “ref” represent the incident and reflected solitary waves, respectively. The TOF is defined as the flight time taken by incident and reflected solitary waves to travel to and fro between the instrumented sensor particles and the interface of the two media, which is obtained by the summation of the wave traveling time T_t in the chain and the contact time T_c between the last particle and the adjacent media at the interface.

$$TOF = T_t + T_c \quad (6.5)$$

Determining TOF was relatively easier than determining the contact time for the last particle with the adjacent media, which is very small and difficult to determine in experiments.

Nesterenko (2001) showed that the energy carried by the solitary wave in the granular chain is equivalent to a lumped-form propagation, primarily limited to wave width of five particles' diameter in spherical chains. In our numerical analysis, we observed that during the impact of granular media with adjacent elastic media, the majority of the wave energy was recovered in the form of potential energy; for example, when the adjacent bounding media a was hard wall (stainless steel material) and a soft wall (PTFE material) almost $\sim 82.5\%$ and $\sim 91.7\%$, respectively, of the wave energy was converted to potential energy.

The higher amount of conversion obtained for the case of the soft wall was due to deeper penetration of the last particle in the soft wall during impact. The localization of the wave energy in the immediate vicinity of the interface is an interesting property of the highly nonlinear media, which is distinct from the characteristics of dispersive wave propagation in the linear media. Therefore, to the first-order assumptions, the interaction of nonlinear granular media with the adjacent linear elastic media can be approximated as the impact of a single particle, i.e., the last particle in the chain, against a half-spaced elastic media. Similar to some of the previous works (Goldsmith, 2001; Hunter, 1957; Maugis, 2010; Reed, 1985), we modeled the collision process as a fully elastic process, and by using the conservation of energy principle we can write the initial energy, i.e., the kinetic energy of the striker, as the summation of the Hertzian potential and kinetic energy of the last particle in the chain,

$$\frac{1}{2}mv_{\text{striker}}^2 \cong \frac{1}{2}m \left(\frac{du_N}{dt} \right)^2 + \frac{2}{5}A|_w u_N^{5/2} \quad (6.6)$$

where v_{striker} is the striker's velocity. Even though the HNSW's speed depends on its amplitude (Eq. (1.10)), and the wave amplitude decreases as the HNSW propagates in the chain, the relationship $V_s \propto F_d^{1/6}$ is extremely weak. Neglecting the effect of dissipation in the short $N = 20$ particle chain for the analytical calculation of TOF, Eq. (6.6) can be simplified as

$$dt = \frac{du_N}{\sqrt{v_{\text{striker}}^2 - 4A|_w u_N^{5/2}/5m}}. \quad (6.7)$$

As obtained by Tillett (1954), the total contact time T_c for compression and tension during a single particle drop on the half-space wall under fully elastic assumptions is calculated by integrating Eq. (6.7) over the period of compression and multiplying the result by two

$$T_c \approx 3.218m^{2/5}V_s^{-1/5}A|_w^{-2/5}. \quad (6.8)$$

The equation shows that the contact time of the last particle $N = 20$ with the adjacent media is a function of $A|_w$, which depends on particle $N = 20$'s and the cylinder's material properties. Hence, by changing the material of the adjacent linear media we expect a change in the contact time T_c .

The time taken by the wave to travel to and fro between the instrumented sensor particle

and wall media was determined by summation of the transit time of incident ($T_{t,\text{in}}$) and reflected ($T_{t,\text{ref}}$) waves, respectively,

$$T_t = T_{t,\text{in}} + T_{t,\text{ref}} \quad (6.9)$$

$$= \frac{d}{V_{\text{in}}} + \frac{d}{V_{\text{ref}}} \quad (6.10)$$

$$= T_{t,\text{in}} \left(1 + \frac{V_{\text{in}}}{V_{\text{ref}}} \right) \quad (6.11)$$

where V_{in} and V_{ref} are the incident and reflected solitary wave speeds, $d = N * (2R)$ is the distance between the center of the instrumented particle and the last particle in the chain, and N is the number of particles between the sensor particle and the wall.

From Nesterenko's (2001) long-wavelength approximation, the incident solitary wave speed V_{in} can be expressed in terms of particle velocity v_p as

$$V_{\text{in}} = \left(\frac{16}{25} \right)^{1/5} (2R) \left(\frac{v_p A |c|^2}{m^2} \right)^{1/5} \quad (6.12)$$

$$= 1.829R \left(\frac{v_p A |c|^2}{m^2} \right)^{1/5}. \quad (6.13)$$

Defining $e = \frac{v_{p,\text{ref}}}{v_{p,\text{in}}}$ as the coefficient of restitution between the particle N and the adjacent linear media, and $\frac{V_{\text{ref}}}{V_{\text{in}}} = \left(\frac{v_{p,\text{ref}}}{v_{p,\text{in}}} \right)^{1/5} = e^{1/5}$, Eq. (6.11) can be simplified as

$$T_t = T_{t,\text{in}} \left(1 + \frac{V_{\text{in}}}{V_{\text{ref}}} \right) \quad (6.14)$$

$$\frac{2NR}{V_{\text{in}}} (1 + e^{-1/5}). \quad (6.15)$$

Chatterjee (1999) showed that, for the uniform chain of spherical particles, when the wave is excited using a striker that is identical to the particles composing the chain, the velocity of a particle in the chain can be represented in terms of the striker's impact velocity (v_{striker}) as

$$v_p \approx 0.682v_{\text{striker}}. \quad (6.16)$$

From Eq. (6.15), Eq. (6.13), and Eq. (6.16) we obtained the transit time of the wave T_t

as

$$T_t = \frac{2NR}{V_{\text{in}}}(1 + e^{-1/5}) \approx 1.180(1 + e^{-1/5})Nm^{2/5}v_{\text{striker}}^{-1/5}A|_c^{2/5}. \quad (6.17)$$

Substituting the result from Eq. (6.8) and Eq. (6.17) into Eq. (6.5), we obtained

$$TOF \approx (3.218A|_w^{-2/5} + 1.180(1 + e^{-1/5})NA|_c^{-2/5}) \left(\frac{m^2}{v_{\text{striker}}} \right)^{1/5}. \quad (6.18)$$

For simplicity's sake, we assumed that the reflected solitary wave speed is equal to the incident solitary wave speed. Then, we can write $e = \left(\frac{V_{\text{ref}}}{V_{\text{in}}} \right)^{-1/5} \approx 1$, and after simplifications we obtained the transit time for the wave in the granular chain as

$$T_t = \frac{4NR}{V_{\text{in}}} \approx 2.361Nm^{2/5}v_{\text{striker}}^{-1/5}A|_c^{2/5} \quad (6.19)$$

and,

$$TOF \approx (3.218A|_w^{-2/5} + 2.361NA|_c^{-2/5}) \left(\frac{m^2}{v_{\text{striker}}} \right)^{1/5}. \quad (6.20)$$

We verified the assumed reflected solitary wave speed equal to the incident solitary wave speed by using the numerical simulation and found a difference of $< 5\%$ for the hard adjacent media (stainless steel). For the soft adjacent media, the difference between the incident and reflected wave speeds was not significant, and the primary contribution to the TOF came from the contact time T_c between the last particle and the adjacent soft media.

This analytical derivation is helpful in understanding the effect of adjacent linear media on the reflected waves. As the adjacent media becomes soft (relative to the particles' material), the contact time T_c increases, and thus the energy localization in the vicinity of the interface increases. This effect can be further understood by observing the particle dynamics and displacement of the particles' center during the interaction of granular media with adjacent linear media from the discrete particle model. Figure 6.3 shows the displacement of particles' center for two extreme cases of adjacent media; the first case is for hard wall (stainless steel) and the second case is for soft wall (PTFE), before and after the interaction on incident wave with the adjacent wall media. The difference in the displacement values of particle $N - 1$ and N for the two cases is evident. All the

particles in the first case were displaced equally and the particle N experienced a single strong collision during the rebound with the other particles in the chain. Also, particle N induced a small displacement ($4.39\mu\text{m}$) in the steel wall over a contact time ($T_c = 85\mu\text{s}$). In this case, a significant amount of energy was recovered in the reflected wave.

In the second case, we observed that because of low level of stiffness of the wall (the stainless steel material is 57% stiffer than the PTFE material), the particle N induced a large amount of push on the wall, resulting in a larger displacement of $16.66\mu\text{m}$. During this displacement, the particle N stayed in contact with the wall media until the wall media recovered its original shape. The contact time calculated in this case was $T_c = 241\mu\text{s}$, which is much longer than the contact time in the first case. This large displacement of the particle N , as compared to the other particles in the chain, results in separation of particle N from $N - 1$. After particle N reaches the maximum compression point (at time $450\mu\text{s}$), a repulsive force, due to the resistance of the wall media, starts pushing the particle back, which leads to the first impact of particle N with the rest of the chain, resulting in excitation of the PSW in the chain. After the impact, the particle N continues to stay in contact with the wall media while the rest of the particles move in another direction. After a short delay (in this example, ~ 0.1 ms), particle N undergoes a second impact with the rest of the chain, resulting in the excitation of the SSW in the granular media. Following the two big impacts, the particle N experiences minor collisions with the rest of the chain, resulting in small backscattered waves in the granular chain.

For the generation of SSWs, we assumed that the critical condition is the separation of the particle N from the rest of the chain, which is possible if the displacement of particle N is greater than the displacement of particle $N - 1$, i.e., the last particle penetrates the wall media and a gap is opened between particle $N - 1$ and N . For this to happen, the critical stiffness at which the displacement of particle N becomes identical to the maximum displacement of particle $N - 1$ is given by $A|_c = A|_w$. Therefore, the relative critical elastic modulus of the wall media (relative in comparison to the elastic modulus of the particles composing the uniform chain) for the generation of SSWs under this assumption can be derived from Eq. (6.2), and equating the chain contact stiffness $A|_c$

with the wall contact stiffness $A|w$

$$E_w|_{\text{critical}} = \frac{E}{2\sqrt{2}-1} \left(\frac{1-\nu_w^2}{1-\nu^2} \right). \quad (6.21)$$

Further, assuming that both the wall media and the chain's particle exhibit similar Poisson ratios, Eq. (6.21) can be simplified as

$$E_w|_{\text{critical}} \approx \frac{E}{2\sqrt{2}-1}. \quad (6.22)$$

Thus, the approximate relative critical elastic modulus of the wall is $\sim 55\%$ of the particle's elastic modulus; we verified this using a numerical solution and found that, at this critical elastic modulus of wall media, the SSWs are formed from the interface with the amplitude as $\sim 5\%$ of the incident solitary wave's amplitude.

Assuming negligible energy dissipation along the chain, we can write the velocity of particle N as v_p , and using Eq. (1.10) ($V_s \propto F_d^{1/6}$) and Eq. (6.13) we can write the amplitude ratio of the primary reflected solitary waves in terms of the particle velocity v_p as

$$AR \equiv \frac{F_{d,\text{ref}}}{F_{d,\text{in}}} = \left(\frac{V_{\text{ref}}}{V_{\text{in}}} \right)^6 = \left(\frac{v_{p,\text{ref}}}{v_{p,\text{in}}} \right)^{6/5} \quad (6.23)$$

$$AR \approx e^{6/5}. \quad (6.24)$$

The coefficient of restitution e depends on the material properties of the particle N and the adjacent media. From this relationship, we can see that, as the coefficient of restitution e decreases, the ARs of primary reflected solitary waves also decrease.

Figures 6.6a and 6.6b show the experimental results for the variation of AR for PSW and SSW, respectively, as a function of elastic modulus of the adjacent media. The analytical predictions and the numerical results confirmed the experimental findings. The amplitude of PSW decreases with the decrease in elastic modulus from 77% for the stainless steel wall to 42.1% for PTFE wall in experiments, whereas, as expected from the conservation of energy and momentum principle, the AR of SSW increases with the decrease in the elastic modulus. This implies that as the elastic modulus decreases, the particle N penetrates deeper into the wall media, and when it rebounds back the impact generated by the

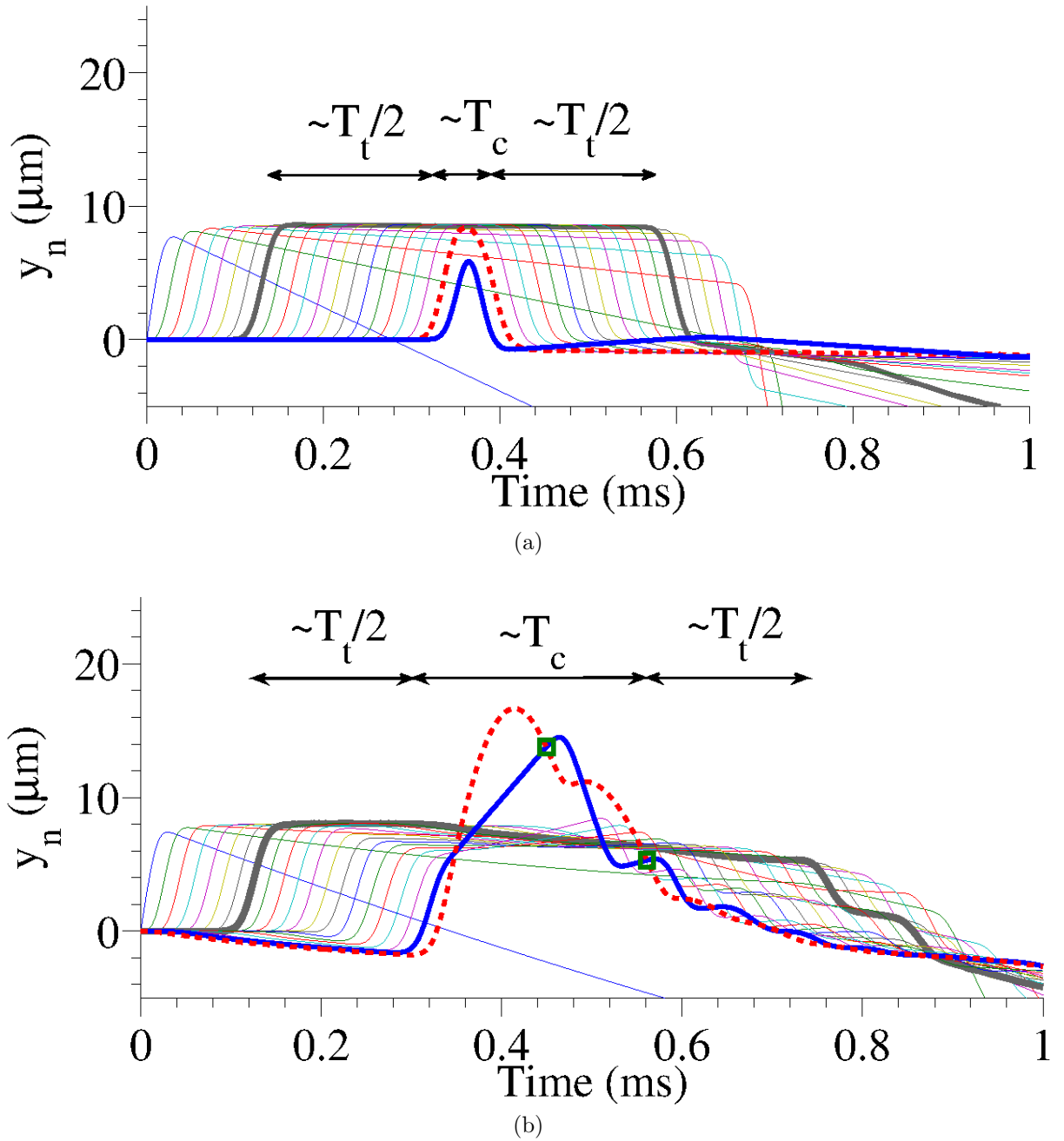


Figure 6.3: Numerical results showing the displacement profiles in the granular chain including the striker bead (first curve on the left) and 20 particles composing the chain. The displacement of the beads is increased under the incidence of the solitary wave. After interacting with the interface, the beads tend to return to their original positions with additional small oscillations, which are particularly evident in the case of wave interaction with the PTFE cylinder. The displacement profile of the 7th particle (thicker solid blue line indicated by y_7) shows distinct portions of solitary wave travelling time (T_t) and contact time (T_c) between stainless steel and PTFE media. (a) The stainless steel wall induces small displacement ($4.39\mu\text{m}$) and short contact time ($85\mu\text{s}$) of the last bead against the bounding wall (bold red line). (b) The PTFE wall allows for a larger displacement of the last bead ($16.66\mu\text{m}$) and as a result, a longer contact time ($241\mu\text{s}$) spent on rebounding. We observe multiple impacts between the last and its neighboring beads. The first and second collisions occur at $450\mu\text{s}$ and $561\mu\text{s}$ points, as marked by circle and square, respectively

collision of the last particle with the rest of the chain is stronger.

Because the wave speed depends on the wave amplitude, as the modulus value decreases the PSW's amplitude drops down, resulting in slower wave speed and increased TOF (Figure 6.4a, where the y-axis is the TOF and the x-axis is the elastic modulus). In the case of the hard (stainless steel) wall, an immediate repulsion of the last particle results in an arrival time of 0.483 ms for PSW, whereas a soft and deformable bounding (PTFE) wall induces considerable delay in the formation of the PSW, resulting in an arrival time of 0.616 ms, or 45% longer than the hard wall case.

Contrary to the behavior of ARs, the TOF behavior of both the PSW and SSW showed that they follow a similar trend, with the addition of constant 0.1 ms delay in the arrival time of SSW, as shown in Figure 6.4b. The primary cause of this effect comes from the particle dynamics in the vicinity of the interface. As explained above using the particle displacement profile for the two extreme cases (stainless steel wall and PTFE wall), this effect is due to the large particle displacement when the wall media becomes softer or when the elastic modulus value decreases resulting in a longer rebound time, and thereby increase in the contact time T_c , which leads to an increase in the TOF value (Eq. (6.5)).

The results obtained are more evident in the force intensity plot (Figure 6.5) performed over specimens with a wide range of Young's modulus. The y-axis and x-axis in the figure represent the Young's modulus and the time scale, respectively. The intensity of data represents the solitary wave amplitude of the traveling pulses at the instrumented particle during the entire process, starting from the wave excitation in the system by striker and including before and after the wave interacts with the wall media at the interface. The first band of intensity represents the incident solitary wave for all of the specimens, which was kept constant for all of the cases; the second and subsequent bands represent the primary reflected solitary wave and the secondary reflected solitary waves formed at the interface of two media, respectively. From the intensity of the signal, we concurred that when the adjacent media has high stiffness value ($E_{\text{particle}} \approx E_{\text{wall}}$), a considerable amount of energy is recovered in the PSW, and when the adjacent media has relatively low stiffness ($E_{\text{particle}} > E_{\text{wall}}$), the particles' dynamics at the interface become significant due to the increased amount of restitutional energy losses, which leads to the formation of SSWs.

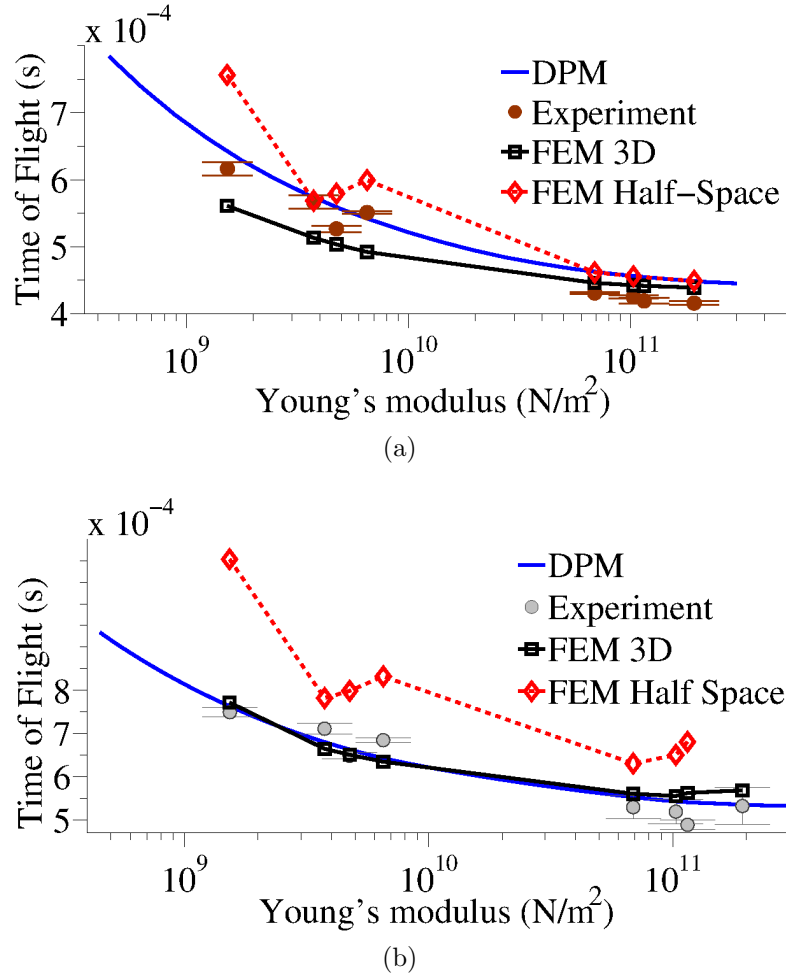


Figure 6.4: Comparison of experimental, theoretical, and numerical data for the time of flight (TOF) of the primary and secondary reflected solitary waves in the chain of spheres as a function of Young's modulus of the neighboring media. (a) Arrival time of the PSW in the instrumented particle (7th from top) as obtained by theoretical models (solid red line), discrete numerical calculations (dashed blue line), and experiments. (b) Arrival time of the SSW, in similar trend to the one of the PSW with an approximately 0.1 ms delay.

The amplitude of SSWs increases with the decrease in wall stiffness value. The formation of SSW is noticeable after a critical value of elastic modulus ($E \approx 100$ GPa, calculated from Eq. (6.22)). Also, as the stiffness of the contact is decreased the TOF of both the PSW and SSW increases.

Figure 6.4 also shows the results obtained from a FEM 3D model and a FEM axis-symmetric half-space model, which confirmed the phenomenon observed in the experiments. The discrepancy in the FEM model for soft materials (polymers) was due to the fact that they were modeled using a simple constitutive equation of pure elasticity and the effect of viscoelasticity was neglected in the model. The axis-symmetric half-space

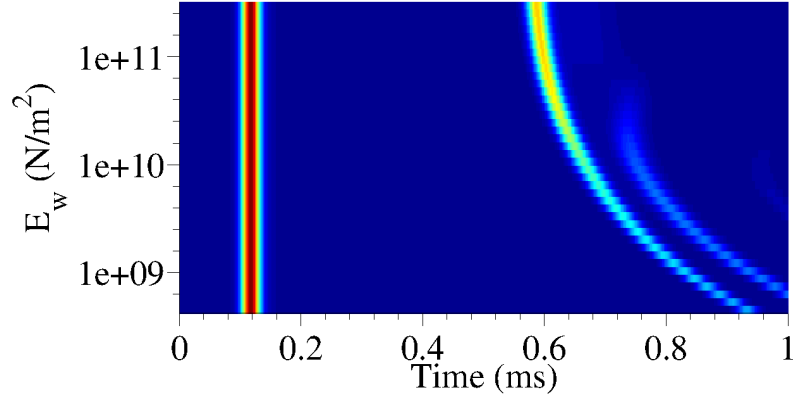


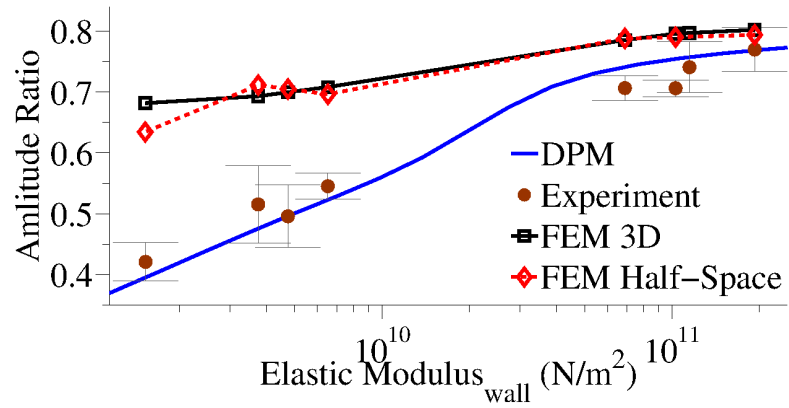
Figure 6.5: Surface plot obtained from numerical simulations showing the formation of primary and secondary solitary waves in the time domain. The y-axis reports a set of different values of elastic moduli of the linear media adjacent to the chain of spheres. As the stiffness of the contact is decreased, the TOF of the reflected wave increases. Here, the first vertical line evident at ~ 120 ms from the impact (Time = 0) represents the arrival of the incoming solitary wave. The generation of a reflected SSW is noticeable after a critical value of elastic modulus of the contact. These simulation results were based on the force profile measured from the 7th bead in the chain, and the color bar on the right denotes the amplitude of the force profiles in N.

model of FEM confirmed that in this case the cylindrical specimen can be treated with one-dimensional assumptions, and we can neglect the flexural and surface waves effect for specimens with diameter four times the diameter of particles composing the chain.

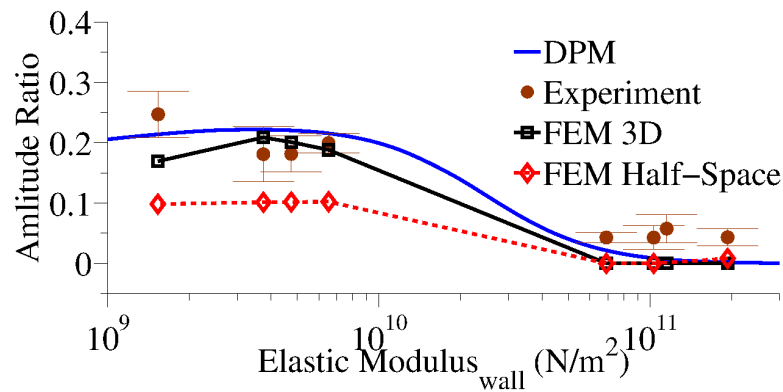
6.1.2 Effects of the Linear Media's Geometry

In this section, we relax the semi-infinite wall assumption on the specimen and examine the effect of geometry of the adjacent media on the wave interaction in the granular media. Since we already analyzed the effect of material's response on the interface dynamics, in this section we analyzed effect of adjacent linear media geometry by using only slender stainless steel cylinders in wide range of heights, varying from 6.35 mm to 609.6 mm. Numerical simulations were performed using a one-dimensional discrete particle model and a three-dimensional finite element model of the exact dimensions of structures as used in experiments. We also created an axis-symmetric FEM for this analysis, where the radial dimensions were made infinite to avoid any wave reflections from the side wall.

Similar to the previous case, Figure 6.7 shows the force intensity plot of the traveling pulse in the chain as measured at the instrumented particle (particle 7 in the chain).



(a)



(b)

Figure 6.6: Comparison of experimental, theoretical, and numerical data for the amplitude ratio of the primary and secondary reflected solitary waves in the chain of spheres as a function of Young's modulus of the neighboring media. (a) Arrival time of the PSW (b) Reflection ratio of the amplitude of the PSW over that of the incident solitary wave in the instrumented particle (7th from top) as obtained by theoretical models (solid red line), discrete numerical calculations (dashed blue line), and experiments.. (c) Arrival time of the SSW, in similar trend to the one of the PSW with an approximately 0.1 ms delay. (d) Reflection ratio of the amplitude of the SSW over the amplitude of the incident solitary wave. The reflection ratio becomes smaller as the elastic modulus increases.

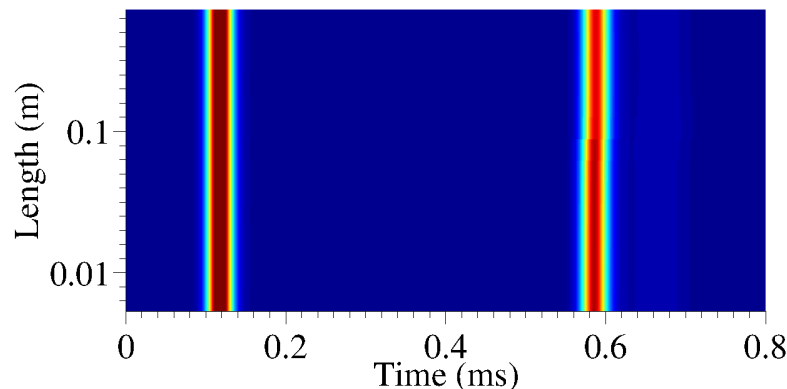


Figure 6.7: Surface plots showing the incident and the reflected solitary waves propagating in the time domain. The y-axis shows the different heights of the stainless steel cylinders. The first band visible on the left represents the incoming solitary waves, while the band on the right shows the reflected solitary waves (PSWs) arriving in the instrumented sensor after 0.53 ms. No secondary solitary wave is observed. Numerical results were obtained by testing 14 slender cylinder samples with different heights. The formation of the PSWs shows no sensitivity to the cylinder heights.

In this study, we observed no formation of SSWs despite the large variation in sample sizes tested. The AR and TOF of the primary reflected solitary wave did not show any significant dependence on the heights of the slender linear media, as the heights of the cylinders were varied (Figure 6.1a). The experimental data show a small variation in the range of 73% to 78%, which implies a strong reflection and that the TOF was relatively constant in the range of $0.44 \sim 0.45$ ms, with 1% experimental error.

We used one-dimensional approximation and neglected the generation of surface and flexural waves in the cylindrical specimens. When the HNSW reaches the interface of two media, it excites longitudinal waves in the cylinder which propagate along the axial direction of the rod. During the contact time T_c between the particle N and the linear media, the longitudinal waves travel a distance of cT_c along the axis of the rod, where c is the longitudinal wave speed in the cylindrical specimen. In the long cylindrical specimen, where $L > cT_c/2$, the time taken by the longitudinal wave to travel to and fro in the specimen was longer than the contact time of particle N with the specimen. In this case, the incident energy from the granular medium was not completely recovered and a small amount of elastic wave energy was lost in the form of leaked elastic waves in the specimen. For the case when $L < cT_c/2$, a partial amount of energy was recovered into the nonlinear medium during the contact time T_c . Using Eq. (6.8) and the material value for stainless steel, we obtained the characteristic length $L \equiv cT_c/2 = 101$ mm. In our

numerical simulations, we observed a small drop in the amplitude ratio after this characteristic length, however the reduction in the amplitude ratio was very limited (less than 5%) and within the sensitive limit of experimental setup. Therefore, the phenomenon was not very evident from the experimental data. In the FEM axis-symmetric model, the AR is constant for all values of heights, even for heights above the critical limits. This may be due to the fact that the mass of specimens is much larger and plays an important role in the interaction phenomenon, and thus energy loss is equal for all of the heights as it only depends on the material of the specimen.

Hunter (1957) and Reed (1985) and other researchers have studied a single particle drop on linear elastic cylinders. In their study, they reported a loss of a very small amount of energy due to wave propagation into the colliding walls. The results obtained from our work for the interaction of nonlinear granular media with linear elastic slender cylinders are in agreement with single particle drop behavior and confirm that the energy lost by elastic waves due to leaking into the linear media was not significant. Hence, the geometry of the stainless steel cylinders has negligible effects on the wave dynamics at the linear/nonlinear interface for the hard wall medium. When the cylindrical samples were made of soft materials, then, as mentioned in previous Section 6.1.1, the particle dynamics in the vicinity will be affected by the linear medium stiffness, which is inversely proportional to length.

6.1.3 Effects of Double-Layer Media: Upper-Layer Thickness

Figure 6.1b shows the finite element modeled for a two-layer composite medium. To understand the effect of layered mass on the interface dynamics of granular media with composite media, we arranged a stiff (stainless steel cylinder) medium in the top layer and a soft (polytetrafluoroethylene (PTFE) cylinders) medium in the bottom layer. We analyzed the effect of upper-layer inertia on the reflected pulses by varying the length of the top cylinder L_u , while keeping the length of the lower-layer fixed. The radius of both upper and lower layers were kept constant for various specimens. Section 2.4 describes the experimental setup used for this study. Similar to the analysis described in previous

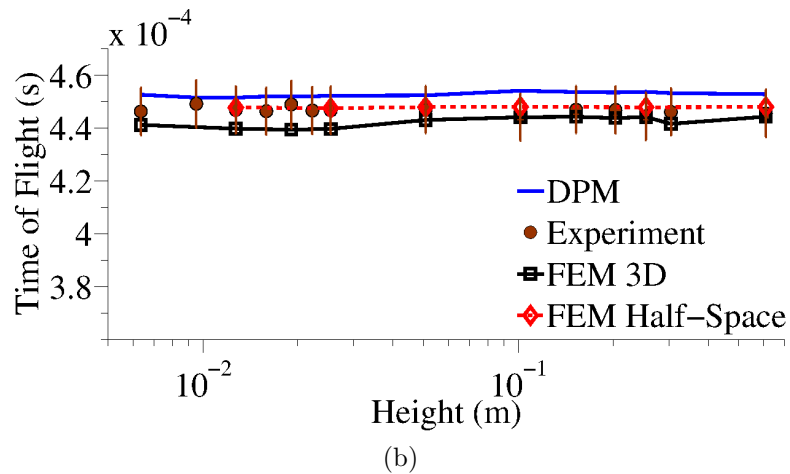
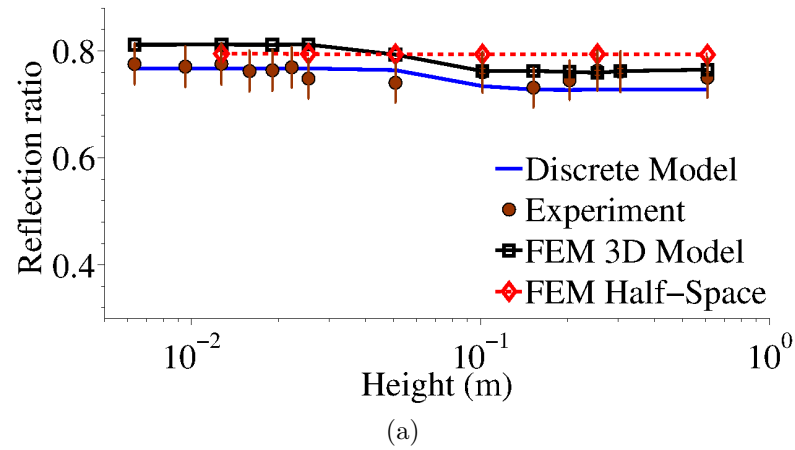


Figure 6.8: Time of flight and reflection ratio of the PSW reflected from the stainless steel slender cylinders as a function of the cylinders' heights. Numerical and experimental data are compared in the magnified Y-axis scale. (a) Arrival time of the PSW, with an extremely regular distribution of the experimental data in the range of $0.44 \sim 0.45$ ms (less than 1% error). (b) Amplitude ratio of the PSWs. Numerical results show a minute drop from 0.764 to 0.734 around the characteristic length of the linear medium ($L = 101$ mm), which is within the range of the error bars from the experimental results.

sections, Figure 6.9 shows the experimental results for the intensity of wave amplitude of the traveling pulse in granular chain measured at the instrumented particle. The change in geometry of the upper layer increases the mass of the upper layer and affects the properties of both the PSW and SSW (Figure 6.10 and Figure 6.11). The results show that as the length of the upper layer was increased by 16 times from 6.35 mm to 101.6 mm, the amplitude ratio of the PSW went up in experiments from 0.428 to 0.769 and the SSW became weak and eventually diminished from 0.3 to 0.

Another interesting observation from these results is the behavior of TOF for both of the reflected waves. The speed of the PSW also increased with the increase in the PSW's amplitude as the length of the upper layer was increased, and thus the arrival time of the wave TOF decreased; for example, in DPM, a reduction of 3.19% in the TOF for PSW was observed when L_u was increased from 6.35 mm to 101.6 mm. The secondary reflected solitary wave followed a drastic opposing trend and showed a gain of 32.5% in the value of TOF in experiments, increasing from $TOF = 0.619$ ms for $L_u = 6.35$ mm to $TOF = 0.821$ ms for $L_u = 101.6$ mm.

The results show that the arrival time and reflection ratios of both the primary and secondary solitary reflected waves were strongly governed by the mass of the upper medium, and, after the critical length of the upper layer, the SSW disappeared and a significant amount of reflected wave energy was transferred back into the granular media by PSW alone. The numerical results confirmed the experimental observation qualitatively. A small discrepancy in the numerical results was due to the inability of the model to capture the complete viscoelastic response of the lower layer PTFE media, which contributes significantly in the formation of the secondary reflected solitary waves. As expected, the results obtained, shown in Figure 6.10 and Figure 6.11, for the AR of primary and secondary reflected waves follow the conservation of momentum and energy principle.

The behavior of the wave dynamics during the interaction of granular media with the composite media was better understood by using the particle dynamics model. Considering v_{in} and v_{ref} as the particle N 's incident and reflected velocity, and using the conservation

of momentum principle, we obtained

$$\frac{v_{\text{ref}}}{v_{\text{in}}} = \frac{m - M_u}{m + M_u} \quad (6.25)$$

where m is the mass of the particle N , and M_u is the mass of the upper layer of the composite media. Because the upper layer was considered as stiff stainless steel material, we had $M_u > m$ for all of the analysis. When the incident solitary wave arrives at the interface of granular media and composite media, the particle N gets the first repulsion and rebounds back, after which the particle N impacts the rest of the chain, resulting in the formation of the primary reflected solitary waves. This analysis confirmed the obtained experimental and numerical results; that is, as the inertia of the upper layer is increased, the rebound of particle N gets stronger, resulting in the PSW of higher amplitudes. If we consider that the upper layer was made of soft medium (like PTFE), then as reported by Job et al. (2005) and described in Section 6.1.1, the particle N will continue to indent the upper layer and rebound back after a prolonged contact time, thereby delaying the formation of PSW.

Similarly, from particle dynamics and using Eq. (6.13), the ratio of incident solitary wave speed (V_{in}) and reflected solitary wave speed (V_{ref}) can be expressed as

$$\frac{V_{\text{ref}}}{V_{\text{in}}} = \left(\frac{v_{\text{ref}}}{v_{\text{in}}} \right)^{1/5} = \left(\frac{M_u - m}{M_u + m} \right)^{1/5}. \quad (6.26)$$

Thus, the traveling time T'_t of the reflected solitary wave for the change in the wave speed can be written as

$$T'_t = \frac{d}{V_{\text{in}}} \left(1 + \frac{V_{\text{in}}}{V_{\text{ref}}} \right) = \frac{T_t}{2} \left[1 + \left(\frac{M_u - m}{M_u + m} \right)^{-1/5} \right]. \quad (6.27)$$

Using Eq. (6.5) and Eq. (6.19), the modified TOF of the reflected solitary waves can be

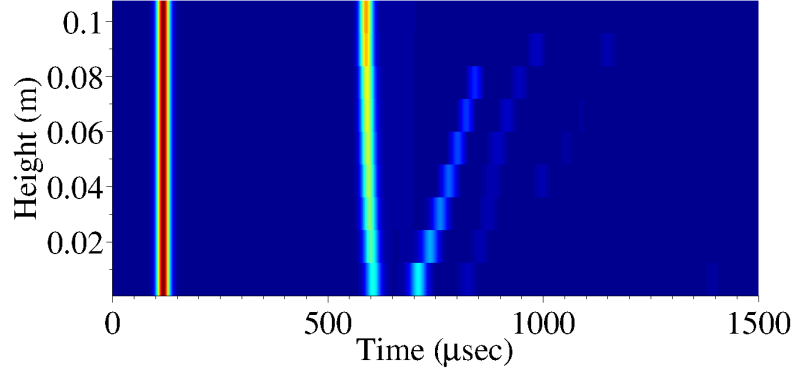


Figure 6.9: Surface plots of incident and backscattered solitary waves as a function of upper layer's height (L_u) in the composite linear media. The primary solitary wave was observed at ~ 0.6 ms, whereas the secondary solitary waves exhibit scattered arrival time in the time domain. Experimental results show the dominance of the PSW at large L_u and the emergence of the SSWs at small L_u . The surface plots are based on the force profile measured from the 7th bead in the chain, and the color bar on the right denotes the amplitude of the force profiles in newtons.

written as

$$TOF|_{\text{PSW}} \approx T_c + \frac{T_t}{2} \left[1 + \left(\frac{M_u - m}{M_u + m} \right)^{-1/5} \right] \quad (6.28)$$

$$= \left[3.218A|_w^{-2/5} + 1.181NA|_c^{-2/5} \left\{ 1 + \left(\frac{M_u - m}{M_u + m} \right)^{-1/5} \right\} \right] \left(\frac{m^2}{V_s} \right)^{1/5}. \quad (6.29)$$

When the mass of the upper layer media becomes infinite, i.e., $M_u \rightarrow \infty$, which is a semi-infinite wall, then the TOF calculated from Eq. (6.29) converges to the value described in Eq. (6.20).

The initial collision of the last particle in the chain caused the translational motion in the upper layer towards the soft lower layer (PTFE layer), thereby compressing it. The velocity of the upper layer after the initial collision of the particle N with the composite medium can be written as

$$V_u = \frac{2m}{m + M_u} v_{\text{in}}. \quad (6.30)$$

If the stiffness of the lower media is much less than that of the upper media, the upper media can be approximated as a rigid body during the interaction with the soft lower medium. Since, we used stainless steel ($E = 200$ Gpa) material cylinder in the upper layer and PTFE ($E = 1.53$ Gpa) material in the lower layer, we can use the rigid body assumption and write the displacement of upper layer's center, solely based on the dis-

placement of the lower layer's center i.e., $\frac{y_{N+1}+y_{N+2}}{2} \cong y_{N+2}$. Using the conservation of the energy principle for full elastic dynamic, we get

$$\frac{1}{2}M_u V_u^2 \cong \frac{1}{2}M_u \left(\frac{du_{N+2}}{dt} \right)^2 + \frac{1}{2}k_d u_{N+2}^2. \quad (6.31)$$

Using one-dimensional wave propagation theory in a slender cylinder member, the stiffness of the lower-layer media can be written as $k_d = E_d A / L_d$, where E_d is the elastic modulus of the lower medium and L_d is its length. Assuming perfect elastic conditions and neglecting energy losses, after integrating the equation, we obtain the contact delayed time between the upper- and lower-layer media

$$T_l = \pi \sqrt{\frac{M_u}{k_d}}. \quad (6.32)$$

The contact delayed time obtained from this equation depends only on the stiffness of the lower-layer media and not on the stiffness of the upper-layer. Thus, in the case of composite media as a wall boundary condition to the granular chains, the SSWs in the chain are formed because of the elastic resistance of the lower-layer media. At the end of this contact mechanism between the upper- and lower-layer media, the lower-layer media tries to regain its shape, which leads to the impact of the upper-layer media with the particle N , triggering the formation of SSWs in the nonlinear granular media. Using Eq. (6.29) and Eq. (6.32), we derived analytically the estimated time of arrival of SSW in the granular media as

$$TOF|_{\text{SSW}} \approx TOF|_{\text{PSW}} + T_l \quad (6.33)$$

which, after simplification, can be written as

$$TOF|_{\text{SSW}} \approx \left[3.218A|_w^{-2/5} + 1.181NA|_c^{-2/5} \left\{ 1 + \left(\frac{M_u - m}{M_u + m} \right)^{-1/5} \right\} \right] \left(\frac{m^2}{V_s} \right)^{1/5} + \pi \sqrt{\frac{M_u}{k_d}}. \quad (6.34)$$

From this analysis and numerical results, we found that after the critical length ($L_u = 25.4$ mm) there is no formation of SSW in the system. The obtained experimental results are in very good agreement with the analytical analysis (Figure 6.10b), even though we neglected the delay caused by attenuation of the SSW.

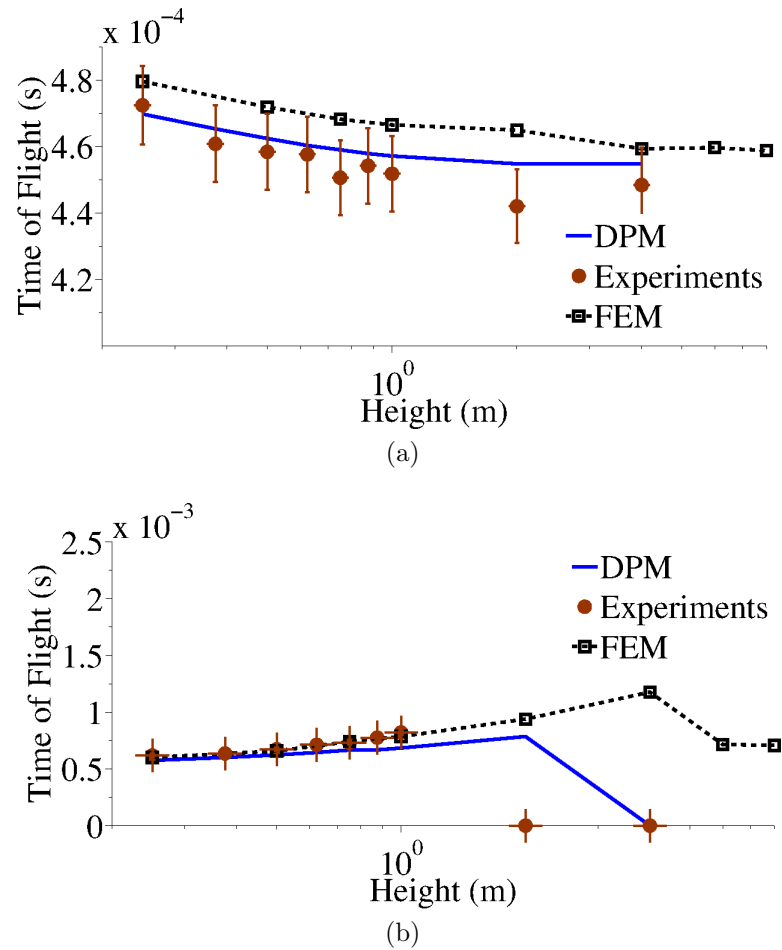


Figure 6.10: Comparison of experimental, theoretical, and numerical data for the time of arrival on the instrumented particle (TOF) of the primary and secondary reflected solitary waves in the chain of spheres, as a function of the upper-layer thickness (L_u) in the composite media. (a) Time of flight for the PSWs. The arrival time is within the 0.43 to 0.47 ms range. (b) Time of flight for the SSWs. Compared to that of the PSWs, the progression is in the opposite direction with improved responsiveness.

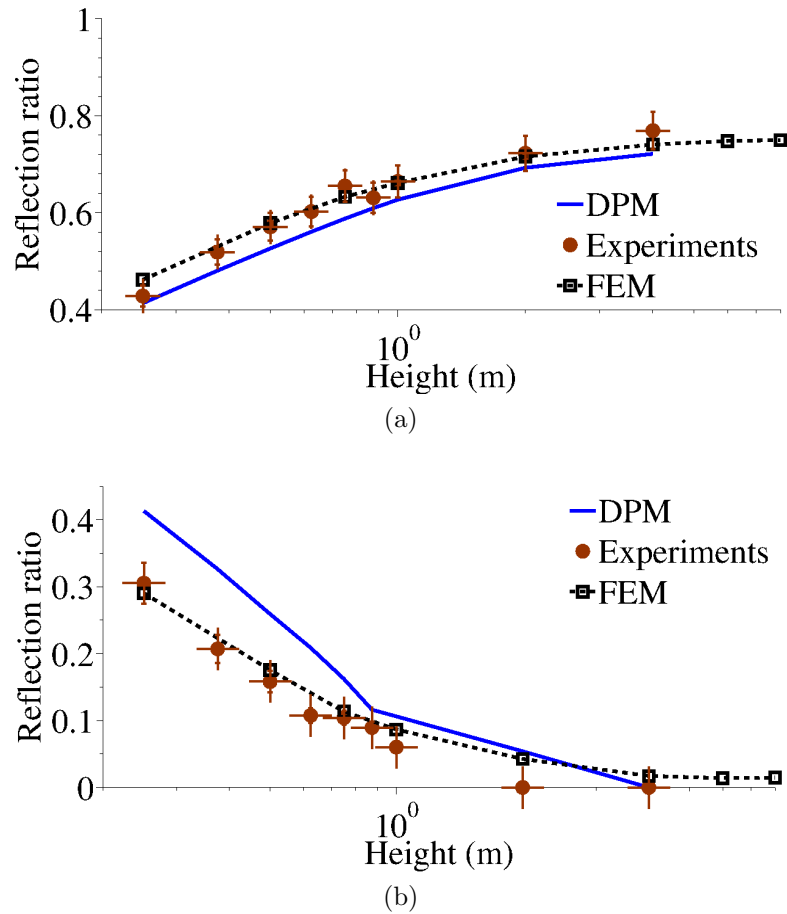


Figure 6.11: Comparison of experimental, theoretical, and numerical data for the amplitude ratio of the primary and secondary reflected solitary waves in the chain of spheres, as a function of the upper-layer thickness (L_u) in the composite media. (a) Amplitude ratio for the PSWs. The amplitude reflection ratio increases as L_u grows. (b) Amplitude ratio of the SSWs. In contrast to PSW reflection in (a), larger L_u yields the smaller SSW reflection in compensation for the increased PSW reflection. For the upper layer taller than ~ 22 mm, the magnitude of the reflection ratio drops below 10%

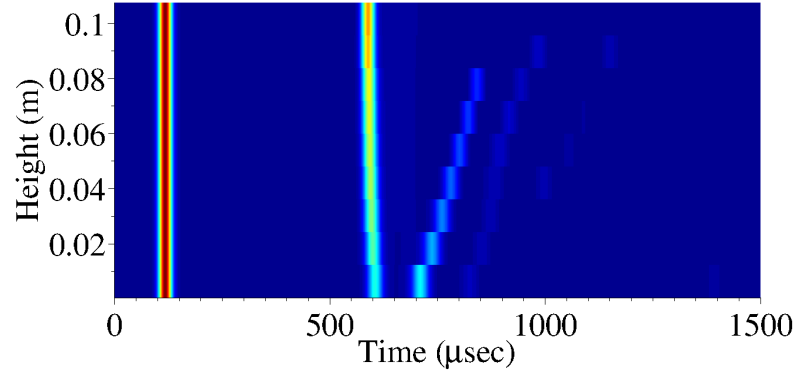


Figure 6.12: Numerical results showing the surface plots of incident and reflected solitary waves in granular chain as a function of lower-layer dimension of the composite linear media. The formation of the primary reflected solitary wave is insensitive to the lower-layer thickness, showing the constant amplitude and arrival time for all lower-layer thicknesses tested. However, the secondary solitary waves reveal significant delay in their formation as the dimension of the lower layer increases

6.1.4 Effects of Double-Layer Media: Lower-Layer Thickness

The study showed that the HNSWs interaction with the layered elastic media is affected not only by the properties of the topmost layer in composite media, but also by the properties and geometry of the lower layer. We varied the length of the bottom PTFE cylinder from 9.52 mm to 152.4 mm in experiments, while keeping the upper stainless steel cylinder length constant at 6.25 mm. Figure 6.12 shows the force intensity of the wave propagation in the granular media, as detected at the instrumented particle, for the variation of the bottom layer. As explained above, the color intensity represents the amplitude of the traveling pulse during the entire observation period. The upper-layer media was kept constant for all of the specimens; therefore, since the PSW is generated by the initial impact of the last bead with the upper-layer media, we found their response to be independent of the variation in the length of the lower-layer media, i.e., the AR of PSWs only varied from 0.40 to 0.46 in both experiments and numerics (Figure 6.14a). Similarly, the TOF of the PSW for all of the specimens were also almost constant (a small fluctuation of 2.5% from 0.46 ms to 0.47 ms) for a wide range of lower (PTFE) layer length (Figure 6.13a).

To understand the cause of delayed SSW, we used Eq. (6.34) and measured the analytical value of TOF for the SSW. The results obtained from analytical analysis were compared with experimental and numerical values in Figures 6.13b and 6.14b and found to be in

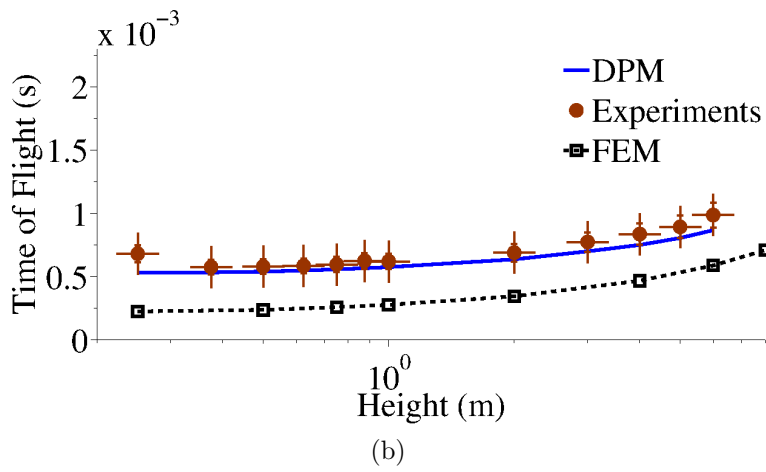
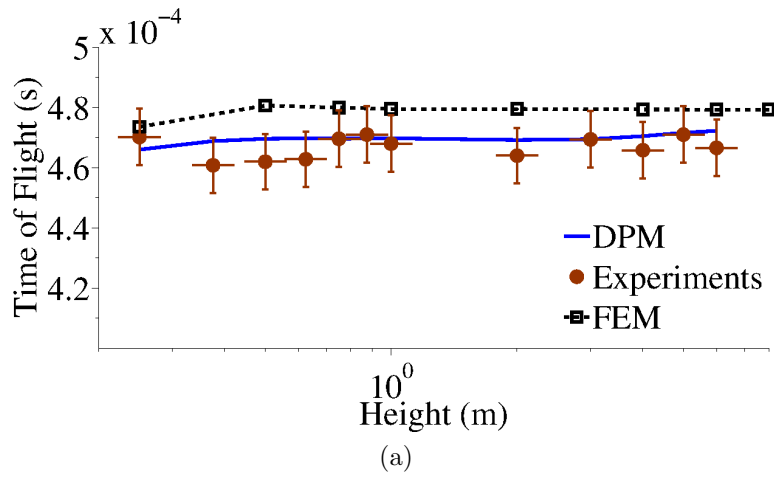
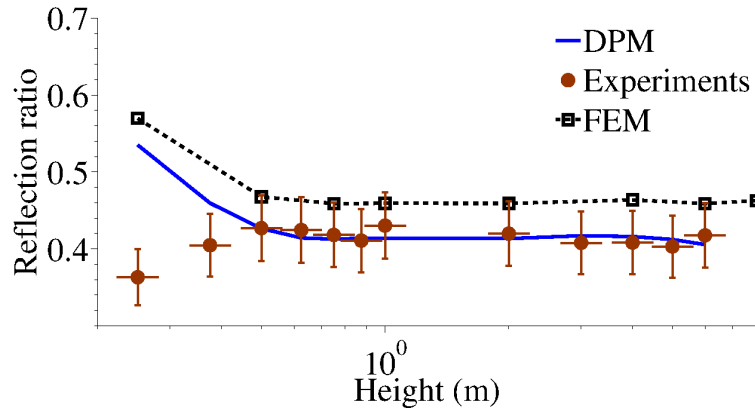
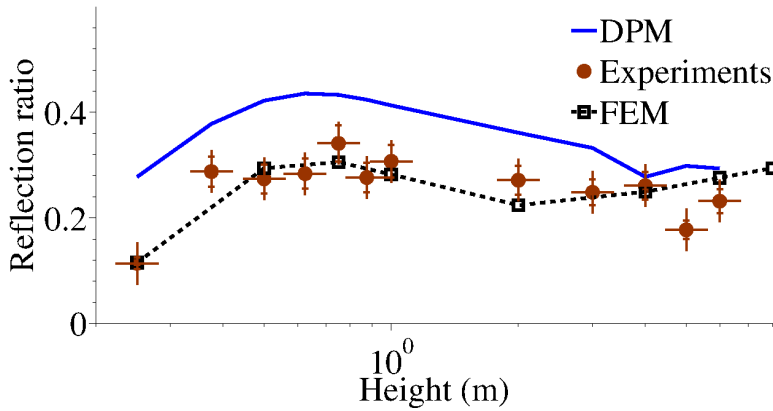


Figure 6.13: Comparison of experimental, theoretical, and numerical data for the time of arrival on the instrumented particle (TOF) of the primary and secondary reflected solitary waves in the chain of spheres, as a function of the lower layer thickness (L_l) in the composite media. (a) Time of flight for the PSWs. (b) Time of flight for the SSWs.



(a)



(b)

Figure 6.14: Comparison of experimental, theoretical, and numerical data for the amplitude ratio of the primary and secondary reflected solitary waves in the chain of spheres, as a function of the lower layer thickness (L_l) in the composite media. (a) Amplitude ratio for the PSWs. The amplitude reflection ratio increases as L_l grows. (b) Amplitude ratio of the SSWs.

very good agreement, which confirmed that the formation of secondary reflected solitary waves was sensitive to the stiffness of the lower-layer media. Due to a decrease in axial stiffness of the system as the length of the lower-layer media was increased, the value of TOF of SSW increases with the increase in the lower-layer media's length.

6.2 Interaction of Highly Nonlinear Waves with an Adjacent Two-Dimensional Thin Plate

We studied the interaction of nonlinear granular media with adjacent thin plate structure by varying the plate thickness and size of granular particles. We also studied the effect of plate's fixed boundary on the interface dynamics of the two media. [Zener \(1941\)](#) developed the theory to explain the impact of single sphere on the large plates using coefficient of restitution. [Sondergaard et al. \(1990\)](#) further did the parametric study on the bouncing of single solid sphere on flat plates and studied the effect of clamped support on the coefficient of restitution between spheres and plates; by varying the diameter of sphere impacted and varying the drop location on the plate. In their work, they found that a critical distance from the clamped support exists for a particular diameter, after which the coefficient of restitution becomes independent of the distance from support.

In our study, we performed analytical study and numerical simulations, and compared the results with experiments. We found very good agreement between the results obtained from three different approaches. The analytical work in this study is based on the model described in Section 6.1, which takes into account the kinetic energy of the plate motion. In our case, the particle N interacts with the thin plate. Similar to the notation in the previous section, u_{N+1} in this section represents the displacement of the top point on the plate, which is in immediate contact with the chain in the initial state before the wave is excited using a striker particle in the chain. The stiffness coefficient $A|_w$ was calculated using the material properties of the plate in contact. We have neglected the effect of dissipation in analytical and numerical analysis, which as will be shown later, the interface dynamics between the granular chain and the plate are affected significantly by

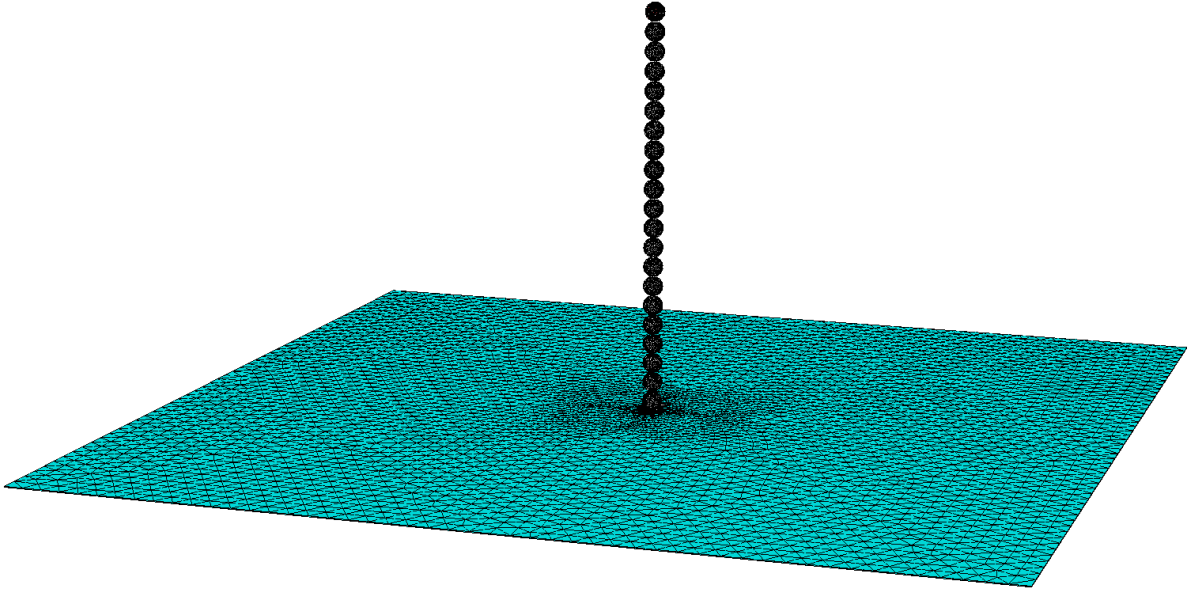


Figure 6.15: FEM showing a uniform one-dimensional vertically aligned chain of 21 spherical particles ($D = 9.52$ mm) placed on top of a horizontal thin plate ($t = 2.28$ mm). Two of the plate edges in one direction were applied with fixed boundary condition, and the other two edges in other direction were free. The wave in the chain is excited using the first particle as striker.

the inelasticity of the adjoined plate. The dissipation affects the overall behavior of the wave propagation as shown in Chapter 4, but it does not affect the result qualitatively. Yang et al. (2011a) developed a spectral element model for the plate, and coupled it with the discrete particle model of the granular chain to describe the interaction behavior between the granular chain and thin plate. The results from the finite element model are in good comparison with the discrete particle model coupled with a spectral element model and with the experimental study.

6.2.1 Effect of Aspect Ratio

This section described the interaction of granular media with the thin plate for various aspect ratios (D/t ; $D =$ particle diameter in granular media and $t =$ plate thickness) by using both granular medias of different particle sizes (D) and plates of various thickness (t). The experimental setup used to study the interaction between granular media and plate is described in Section 2.5. To understand the true effect of aspect ratio on the interface dynamics between granular media and plate, we placed the granular media at the center of the plate, far away from plate boundary condition. Figure 6.16

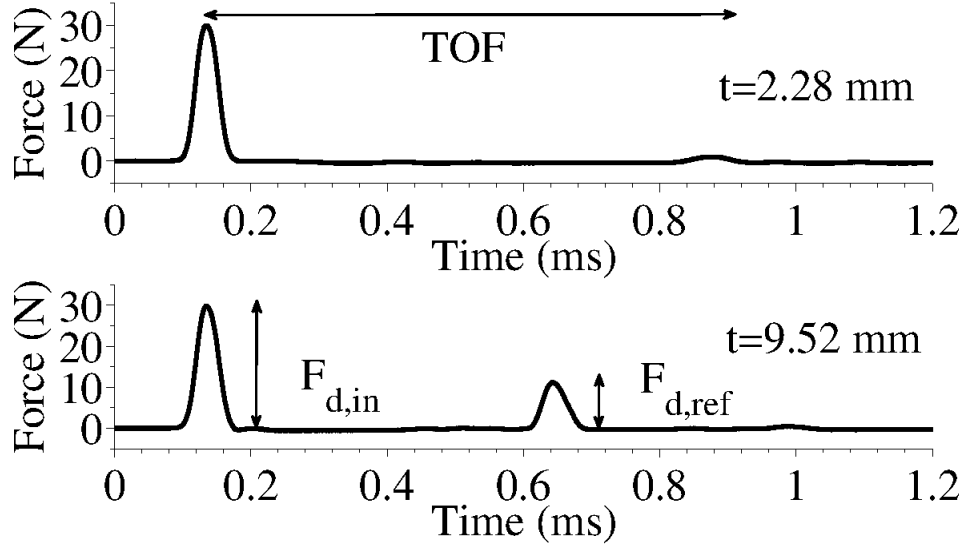


Figure 6.16: Force profiles obtained from experiments for solitary wave propagation in the granular media ($D = 9.52$ mm) under the interaction with two different plates. (a) Force profiles for a thin plate ($t = 2.28$ mm). (b) Force profiles for a thick plate ($t = 9.52$ mm). The reflected solitary waves against the thick plate exhibit stronger (larger F_{ref}) and faster (smaller TOF) compared to the thin plate case.

show an example of the nature of the force profile obtained from the instrumented particle in the experiment for two extreme cases, involving a uniform chain with particle diameter $D = 9.53$ mm placed on top of two different plates ($t = 2.28$ and 4.83 mm), respectively. Similar to the interaction of granular media with a one-dimensional wall boundary, we see that the characteristic of the reflected waves is affected by the change in the plate thickness value; the wave reflected from the thick plate has a larger reflected wave amplitude and faster wave speed as compared to the wave reflected from the thin plate. When the incident wave arrives at the interface, the particle N interacts with the plate medium. The wave reflection results from the two cases depict the restitution behavior between the chain and the respective plate, which is similar to the classical problem of single ball impact on a plate (Reed, 1985; Sondergaard et al., 1990; Tillett, 1954; Zener, 1941). Also, due to the discreteness and nonlinearity in granular media, the significant amount of energy of the incident wave is concentrated on the particle N (Nesterenko, 2001), and for a relatively small contact time between the particle N and the plate, the problem can be simplified as single ball drop on plate. Hence following a similar approach as the classical problem of single particle impact with thin plate, we used coefficient of restitution between particle N and thin plate to define the relationship between the reflected solitary wave in the chain with the aspect ratio of particle diameter to plate thickness.

Zener (1941) derived the analytical equation describing the dimensional approach (σ) of a single particle towards a thin plate under elastic impact in terms of the dimensionless time (τ) and inelasticity parameter (λ), which is given as

$$\frac{d^2\sigma}{d\tau^2} + \left(1 + \lambda \frac{d}{d\tau}\right) \sigma^{3/2} = 0 \quad (6.35)$$

$$\left. \begin{array}{l} \sigma = 0 \\ \frac{d\sigma}{d\tau} = 1 \end{array} \right\} \text{at } \tau = 0 \quad (6.36)$$

where λ is calculated from

$$\lambda = \frac{\pi^{3/5}}{4\sqrt{3}} \left(\frac{D}{t}\right)^2 \left(\frac{\rho_s}{\rho_p}\right)^{3/5} \left[\frac{v_{in}^2 \rho_p (1 - \nu_p^2)}{E_p}\right]^{1/10} \left[1 + \frac{E_p (1 - \nu_s^2)}{E_s (1 - \nu_p^2)}\right]^{-2/5} \quad (6.37)$$

here D and t are the particle's diameter and the plate's thickness, respectively. E , ν , and ρ are the elastic modulus, Poisson's ratio, and density, respectively. The subscripts s and p are the representative of the spherical particles and the thin plate material response, respectively. The impact velocity v_{in} corresponds to the maximum velocity of the N^{th} particle in the chain during the impact. From Eq. (6.37), we found that the inelasticity parameter λ depends on the material and geometrical properties of both the particle at the interface and the plate.

The numerical contact time between the particle N and the plate can thus be calculated using the dimensional contact time (τ_c), which is determined from Eqs. (6.35) and (6.36) (Zener, 1941)

$$T_c = m_s^{2/5} v_{in}^{-1/5} A|_p^{-2/5} \tau_c \quad (6.38)$$

where m_s is the mass of the spherical particle, and $A|_p$ is the contact stiffness between the particle N and the plate, as defined in Eq. (6.2).

The restitution coefficient e between particle N and plate can be calculated using Eq. (6.35) and Eq. (6.37) by setting the condition $d\sigma/d\tau \rightarrow 0$. Consequently, when $D/t \rightarrow 0$, i.e., either the particle diameter is too small or plate thickness is too big, the plate can be considered as the semi-infinite wall, such that $\lambda \rightarrow 0$. Assuming perfect elastic collision between particle N and the plate, we get $e \approx 1$. The contact time τ_c for this case is

determined using $\tau_{c,0} = 3.218$ (Eq. (6.8), Fig. 6.17). Vice versa, when $D/t \rightarrow \infty$, i.e., either the particle diameter is much larger or the plate is very thin, then $\lambda \rightarrow \infty$ and $e \approx 0$.

Based on the classical wave theory of plates (Reed, 1985), we know that if the waves in the plate returns back to the impact point after the reflection from the boundary, then the partial energy is retrieved in the form of potential energy in the striker. If the plate supports are far away, such that the flight time of wave reflection from supports do not arrive at the impact point during the contact time period of particle, than part of the energy is lost in the modes of plate.

Tillett (1954) showed that for single particle interaction with thin plate, when the inelasticity parameter λ increases, the restitution coefficient e decreases resulting in the increase in contact time τ_c between the particle and the plate. For the specific combinations of different chains and plates used in our experimental study, we observed a similar phenomenon. This effect is evident from Eq. (6.37), where the decrease in the plate stiffness value (E_p) results in an increase in the value of λ . The granular chain composed of smallest diameter ($D = 4.76$ mm), the λ value obtained for three different plates used in the experiment was < 1 , namely $\lambda = [0.32, 0.166, 0.072]$. Therefore the corresponding analytical contact time obtained for the chain interaction with three plates was approximately $T_c = 28.5$ μsec . This value is comparable to the contact time between particle of $D = 4.76$ mm and the elastic half space $T_{c,0} = 27.7$ μsec obtained from the Eq 6.38. As the particle diameter is increased in the second set of chain $D = 9.76$ mm, the inelasticity parameter value decreases from $\lambda = 1.28$ for the thinnest plate ($t = 2.29$ mm) to $\lambda = 0.2$ for the thickest plate ($t = 0.2$ mm), and therefore the contact time decreases from $T_c = 87.81$ μsec to $T_c = 59.1$ μsec , which is again comparable to elastic half space contact time $T_{c,0} = 55.6$ μsec . For the chain composed of largest diameter $D = 19.1$ mm, the aspect ratio with the thickest plate used in the experiment was $D_{max}/t_{max} = 3.95$, which implies that the plates selected in this case of bead diameter cannot be considered half space. This is evident from the λ value changes from 5.15 to 1.16, which leads to change in $T_c = 1435.17$ μsec for $t = 2.29$ mm to $T_c = 164.38$ μsec for $t = 4.83$ mm. The contact time between chain of bead diameter $D = 19.1$ and elastic half space is $T_{c,0} = 111.44$ μsec ,

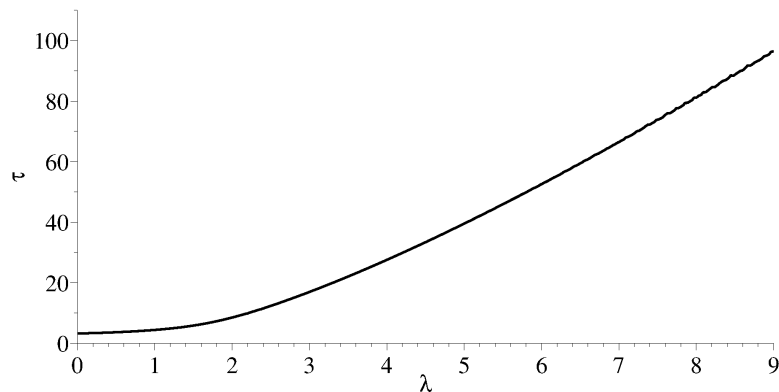


Figure 6.17: Plot showing theoretical value of dimensionless contact time (τ_c) as a function of inelasticity parameter (λ). The dimensionless contact time approaches $\tau_{c,0} = 3.218$ for the value corresponding to $\lambda = 0$, which is the case of elastic impact of spherical particle against a semi-infinite elastic media.

which is much larger than the contact time calculated for the corresponding chain with the actual plates used in the experiments. This will be the case when $0 < e < 1$, partial energy of the bouncing particle is lost in the intrinsic mode of inelasticity of plates, which are different from dissipative losses, such as plasticity or viscoelasticity.

Now we consider the reflected waves generated in the chain due to the interaction of granular media with plate. From Eq. (6.24), we found that the AR of the primary reflected solitary wave is also a function of the aspect ratio (D/t) of the particle N 's diameter and the plate's thickness. Figure 6.18 shows the numerical and experimental results for the combinations of various particle diameters and plate thicknesses used in the testing, as well as a comparison with the analytical values, which confirms that the AR of PSW decreases with the increase in aspect ratio. Taking a correlation with the single ball drop on the plate, it suggests that by increasing the particle diameter the inertial effect of the particle increases, and similarly, by decreasing the plate thickness the inelastic effects of the plate increase too. The results confirm that for combined effect of particle diameter and plate thickness for a large aspect ratio ($D/t > 5$), we observed almost negligible reflected solitary wave, i.e., the $AR \rightarrow 0$. The small discrepancy observed in experimental results was due to the presence of dissipation effects in the system, which, for simplicity's sake, were ignored in the current numerical model.

Using Eq. (6.18), we calculated the analytical values of TOF for the primary reflected solitary wave at the instrumented particles in the chain. The results obtained from numerics

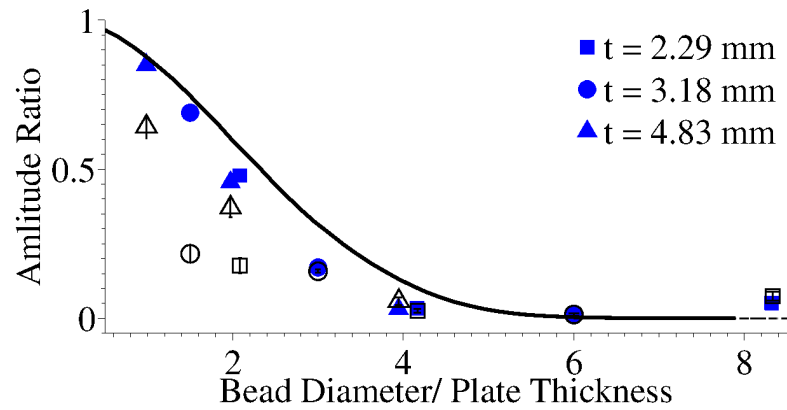
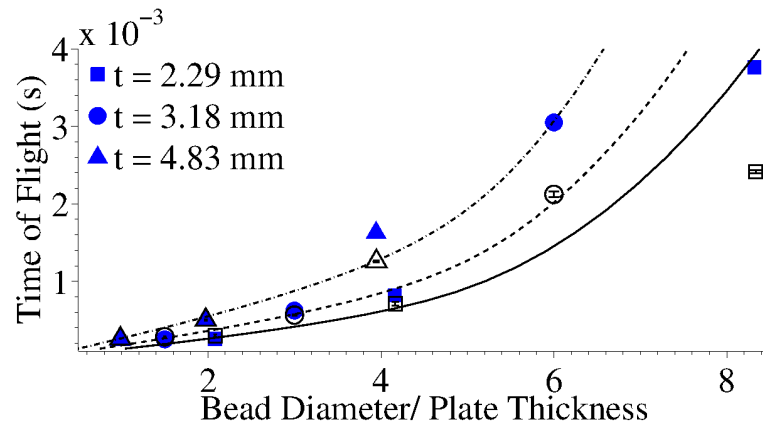
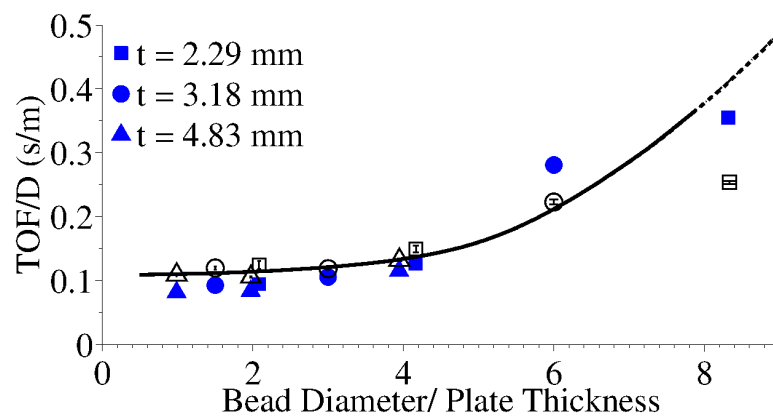


Figure 6.18: Amplitude ratio of reflected solitary waves (AR) as a function of the ratio of the sphere diameter to the plate thickness (D/t). The solid black line represents the analytical results, while the filled and hollow marks denote the finite element model and experimental results, respectively.



(a)



(b)

Figure 6.19: (a) Time of flight (TOF) as a function of D/t . (b) Normalized TOF with respect to D as a function of D/t . After normalization, three different curves in (a) overlap into a single curve in (b). The solid black line represents the analytical results, while the filled and hollow marks denote the finite element model and experimental results, respectively.

and experiments are compared with analytical values in Figure 6.19a. From this study, we found that the amplitude ratio of the reflected waves is only a function of aspect ratio (D/t), while the TOF value further depends on plate thickness or particle diameter, i.e., by increasing diameter of the particle or by decreasing thickness of the plate, the wave gets further delayed. Normalizing the Eq. (6.18) with the particle diameter $D = 2R$, we obtained simplified equation

$$\frac{TOF}{D} = \left[1.414(1 + e^{1/5})N \left(\frac{1 - \nu_s^2}{E_s} \right)^{2/5} + 0.853\tau_c \left(\frac{1 - \nu_s^2}{E_s} + \frac{1 - \nu_p^2}{E_p} \right)^{2/5} \right] \rho_s^{2/5} v_{\text{striker}}^{-1/5}. \quad (6.39)$$

Because e and τ_c are each a function of aspect ratio only, from this analysis and Figure 6.19b we found that the normalized TOF is also a function of aspect ratio only. The analysis suggested that by changing the relative particle dimension, increasing the particle diameter or decreasing the plate thickness, the contact time of particle N with the adjacent plate medium is affected.

6.2.2 Effect of Plate Boundary

In this section, we study the effect of the boundary condition on the interaction of granular media with the thin plate medium by placing the granular media at various locations along the centerline on the plate towards the fixed boundary condition. We used two sets of vertically aligned uniform chains with particle diameter $D = 9.53$, and 19.05 mm, respectively. Two of the plate's edges in one direction were clamped and the two in the other direction were free.

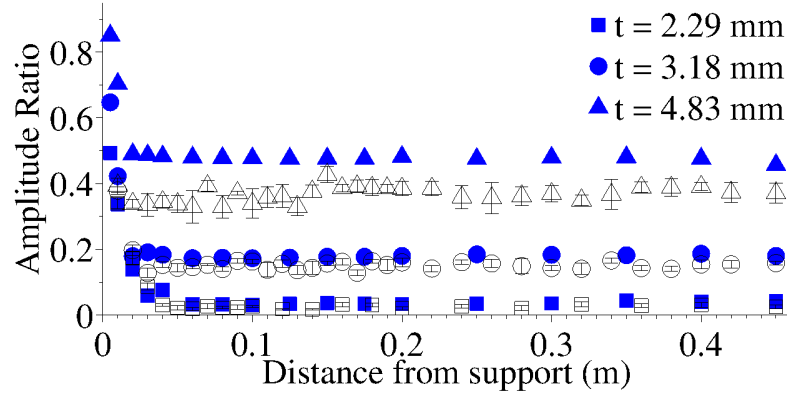
[Sondergaard et al. \(1990\)](#) studied the interaction between solid spheres of various diameters and materials with the plates of various thickness and material and found that the reflection of the shear or Rayleigh waves, rather than the dilatational waves, is the primary cause for the change in the interaction behavior between the particle and the plate when the distance from the support system is changed. The thin plates also support the formation of Lamb waves with different modes, and each mode propagates with different

group velocity. The wave speed inside a thin plate can be written as

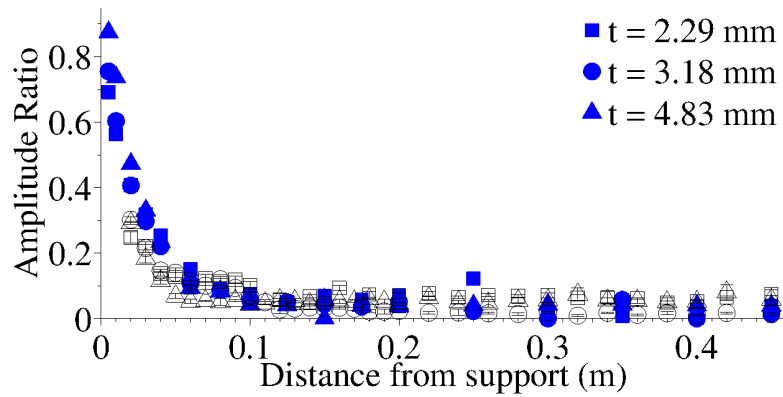
$$c = k \sqrt{\frac{E_p}{\rho_p}} \quad (6.40)$$

where k depends on the nature of the wave under consideration, such as dilatational wave, shear wave, Rayleigh wave ($k = 0.57$, $c \approx 2900$ m/s), or Lamb wave with a particular mode ($k = 0.2$ for the A_0 mode of the Lamb wave, ≈ 1000 m/s). Considering that the chain is placed at the center of the plate, the calculated time for the Rayleigh wave to propagate in an aluminum panel of dimensions $= 914 \times 914$ mm from the impact point to the boundary and back to the impact point will be $T_{\text{Rayleigh wave}} = 315.17 \mu\text{sec}$. Similarly, the calculated time for the A_0 mode of Lamb wave to propagate inside the plate will be $T_{\text{Lamb wave}} = 914 \mu\text{sec}$. When the flight time of wave inside the plate is compared with the contact time of bead with the plate for the chain placed at the center of the plate, mentioned in previous section, we can see that for the combination of bead with diameter $D = 19.1$ mm and plate thickness $t = [2.29, 3.18]$ mm, the contact time of bead is much larger than the Rayleigh wave flight time in plate and comparable with the Lamb wave flight time. We will use this information in this section to show that the nature of the reflected waves in the chain are affected significantly by the Rayleigh and Lamb waves in the plate.

Figure 6.20a and Figure 6.20b show the results obtained from the experiments and numerics for the amplitude ratio as a function of the distance from the clamped end. From these results, we found that when the chain was placed in the vicinity of the clamped support, the system induces strong reflected waves with higher amplitude and faster wave speed (smaller TOF) for both of the chains and for all of the plates. Another interesting phenomenon we found from the observation of these results is that the AR of the reflected waves for each chain and plate decreases and TOF value increases as the distance of the chain from the clamped support was increased. Furthermore, the boundary effect on the interface dynamics diminished completely, and the response of the wave interaction became independent of the distance from the clamped support when the chain was moved a sufficient distance away from the boundary, namely after a critical distance. But, for the chain with particle diameter $D = 9.53$ mm, and the plate having thickness on the comparable scale $t = 4.83$ mm, we found a strong reflected solitary wave in the zone



(a)



(b)

Figure 6.20: Amplitude ratio of reflected solitary waves (ARR) as a function of distance from the support. (a) Granular crystal with small spheres ($D = 9.53$ mm). (b) Granular media with large spheres ($D = 19.1$ mm). The filled and hollow marks denote the finite element model and experimental results, respectively.

outside of critical distance of the plate. As the granular particle diameter increases, the inertia of the chain also increases, which means the amplitude ratio of the reflected waves with larger particle diameter showed a steep decay of wave amplitude for all of the cases of plates, as compared to the chain with smaller particle diameter.

From the two studies of interaction of HNSWs with the thin plate, we found that the AR ratio of reflected waves in granular media decreases with the decrease in aspect ratio or with the increase in the distance from clamped support. From the analytical analysis we know that changing the aspect ratio or the distance from the clamped support affects the local stiffness value between particle N and thin plate. Thus, by monitoring the reflected waves in the granular media, we can predict the change in the effective local stiffness of the thin plate.

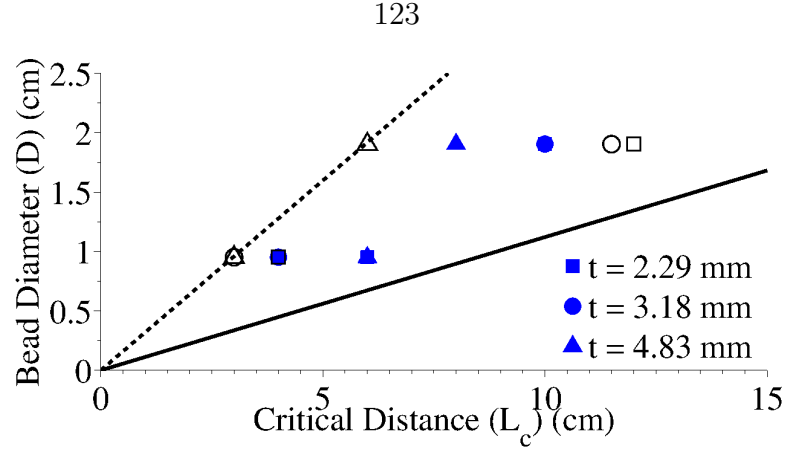


Figure 6.21: Critical distances (L_c) in various thicknesses (t) of plates and the diameters (D) of granular medias. Solid and dashed black lines denote the analytical predictions based on the propagation of guided waves with velocity parameter $k = 0.5$ and 0.2 (i.e., $c = 2,900$ and $1,000$ m/s), during the contact time $T_{c,0}$. The experimental and FEM results are represented by the hollow and filled marks, respectively.

The critical distance L_c in the plate can be defined as the distance for the waves to reach from the impact point to the nearest support point during the half contact time $T_{c,0}$ (Eq. (6.8))

$$L_{c,0} = \frac{cT_{c,0}}{2} \quad (6.41)$$

$$= 1.37kD \left[\rho_s \left(\frac{1 - \nu_s^2}{E_s} + \frac{1 - \nu_p^2}{E_p} \right) \right]^{2/5} \sqrt{\frac{E_p}{\rho_p}} v_{\text{striker}}^{-1/5}. \quad (6.42)$$

Figure 6.21 shows the critical distance obtained from experimental data, numerical results, and a comparison with the theoretical analysis. The theoretical analysis suggests that the obtained experimental and numerical results for the critical distance lies between $k = 0.57, c \approx 2900$ m/s for the Rayleigh wave propagation (black solid line) and $k = 0.2, c \approx 1000$ m/s for the A_0 mode of the Lamb wave propagation (black dashed line). This implies that the primary amount of energy carried by guided wave is in the form of A_0 mode of the Lamb waves, and that the critical distance depends on both the particle diameter and the plate thickness. For the thinner plate, as compared to the thicker plate, the critical distance is larger due to the increased contact time.

6.2.3 Discussion

By studying the effect of aspect ratio and plate boundary condition for the interaction of granular media with thin plates, we found that the effective restitution coefficient of the chain decreases with the increase in the aspect ratio (D/t) or by increasing the distance from the plate's fixed boundary condition. As mentioned earlier in the literature that during the interaction between chain and plate, the majority of chain energy is retrieved as potential energy between the last bead and the plate.

The conventional restitution parameter was used to derive a synonymous between the interaction of chain composed of spherical particles and thin plate with interaction of single spherical particle and thin plate. This assumption allowed us to simplify the complex interaction between chain and plate with interaction between single particle and plate. Using the coefficient of restitution, we can determine the approximate energy retrieved back in the chain and the properties of reflected solitary wave.

Similar to the intrinsic inelasticity parameter between single spherical particle and plate, we defined an intrinsic inelasticity between chain and plate. The dimensionless intrinsic inelasticity parameter depends on the properties of both bead and plate properties as well as on the striker velocity. This parameter helped us in understanding and comparing various combination of uniform chains with different diameter bead and plates of various thicknesses. The coefficient of restitution of chain can be determined from the inelasticity parameter and thus the force exerted on the plate by the chain can be calculated. We also showed that with increasing aspect ratio of the bead diameter in the chain towards the plate thickness, the inelastic parameter λ of the plate increases.

Increasing inelastic parameter also implies that a larger amount of kinetic energy of the chain is transferred to the kinetic energy of the plate in the form of various flexural modes. For example, the contact time defined for the last particle in the chain composed of uniform spheres with diameter $D = 19.1$ mm and plate with thickness $t = 2.28$ mm in Section 6.2.1 was $T_c = 1435.17$ μsec . Even though, the contact time in this case was much larger than the propagation time of Rayleigh wave or A_0 Lamb wave mode inside the plate, not significant amount of energy was retrieved back in the chain. This is because due to

large aspect ratio in this case, the value of inelasticity parameter was also large, which resulted in extremely small coefficient of restitution ($e = 0.00019$). Therefore, in this case the last particle in chain moves with plate motion for the later part of impact and does not contain significant momentum to generate reflected solitary wave in the chain.

The boundary condition of the plate helped in determining the effective inelasticity parameter between the chain and plate, and in defining the effective coefficient of restitution of the chain. When the chain will be placed closer to free boundary condition of the plate, the coefficient of restitution will be lower compared to when it is placed near fixed boundary condition in this study. We know that the Rayleigh wave's in-plane amplitude decays by $1/\sqrt{r}$, where r is the radial distance from the point source. The affect of this phenomenon becomes significant only when the chain is placed within the vicinity of the critical distance of the plate boundary. For the case studied in Section 6.2.1, the chain is placed far outside the critical limit, and therefore the nature of results does not get affected by the wave decay in the plate. For the second case studied in Section 6.2.2, as the chain is placed closer to the plate boundary condition, the effective restitution coefficient of chain increases and thus the energy reflected back in form of solitary wave also increases. To note is that we have neglected effects of energy dissipation for the wave traveling in the chain (as described in Chapter 4) and also the effect of energy losses for the wave motion in the plate, and may be energy losses due to relaxation of the stresses during the impact of particle N with the plate. The specimen considered in our case are aluminum plates, the energy lost in the elastic waves in these materials should be small. The addition of dissipation effect will decrease the wave energy reflected back in the chain after the interaction and will vary the properties of the reflected solitary waves in terms of smaller amplitude and slower speed, but the overall results will be of similar nature and will be effected equally. However, for a particular specific application, it is critical to define the parameters for energy losses as explained in Chapter 4. Based on the application setup and underlying specimen, for example hard steel plates, laminate, polymer, etc, the energy losses can be critical.

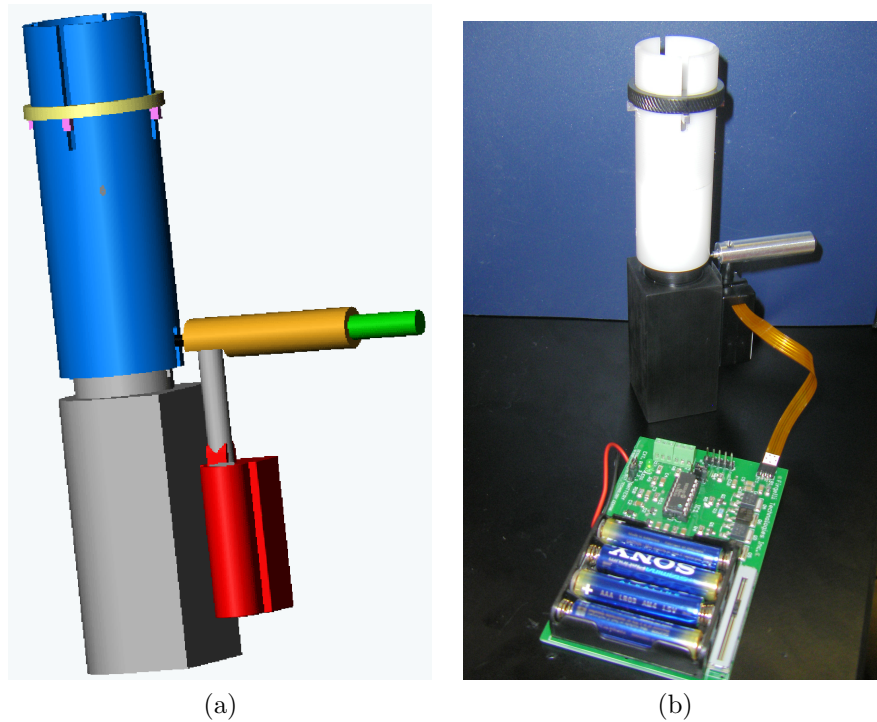


Figure 6.22: Fully automated nonlinear actuator (a) schematic and (b) model

6.3 Nonlinear Actuator Design

All the experiments described in this manuscript were performed by using a manually controlled nonlinear actuator, in which the pulses were generated by dropping a striker on top of the vertically oriented granular chain enclosed in a holder (shown in (Daraio et al., 2006b) and (Khatri et al., 2008)).

A fully automated device (Figure 6.22) which is able to excite highly nonlinear waves and operate independently in different orientations (not only vertically), has been developed in our laboratory (Eggenpieler et al., 2008). Due to its low power requirements and independent/remote operation, such a stand-alone system may be used for nondestructive evaluation (NDE) and in particular for structural health monitoring (SHM). The system designed is composed of a spring loaded adjustable striker, a chain of stainless steel particles of diameter 4.76 mm (provided by McMaster-Carr), a trigger, and a cyclically loading system (linear actuator) for the automated operation. Through this combination of elements, the system can generate pulses to be directed into a structure or material to be evaluated. The sensor system is portable, energy efficient. In comparison to conven-

tional test system, the signal to noise ratio is very high, which is very advantageous as the sensor output will not require any amplification in the monitoring of output from the sensor. By varying the diameter of the spherical particles in the chain or by developing a non-uniform chain, it is possible to excite different mode of vibration in the structures.

The ability of this complex nonlinear system of chain of particles interacting with various structures to be simplified with the single particle interaction with structures provide unique advantages. Based on the available knowledge present in the literature on the single particle interaction with rod/plate and other structures, an analytical scheme can be developed for advanced diagnostic of specimen without the requirement of baseline data.

The system can be modified in the future to operate it remotely through wireless transmission (i.e., via Bluetooth) and for controlling the input signal. This will allow the ability to place the nonlinear actuator system in the remote hot spots on structures. Hot spots are critical localized zones on structures of aircraft/ship/bridge or any other system, which are highly prone to defects, may it be fatigue cracks, corrosion, or damage in the weld joint.

Chapter 7

Conclusion and Future Work

In this thesis, we experimentally and numerically studied the formation and propagation of highly nonlinear solitary waves in a one-dimensional chain of spherical particles, and their use as information carriers. For numerical techniques, to overcome some of the limitations of the discrete particle model (DPM), which considers the particles as point masses of single degree of freedom, we developed a finite element model (FEM) of nonlinear granular system using a commercially available software (Abaqus). We validated our FEM in a static setting by comparison with the Hertzian contact law between two particles, and in a dynamic setting, by comparison with highly nonlinear solitary wave (HNSW) theory. The FEM results were also verified with experiments and a comparison was also made with the results obtained using a discrete particle model. An excellent agreement was found between all three approaches, namely experimental, finite element model, and discrete particle model. The reliability of a finite element simulation for the wave propagation model depends highly on spatial and temporal discretization. We performed the mesh convergences study of the spatial discretization of the particles in FEM to obtain an optimized mesh size (density) for an economic solution without losing accuracy. We also showed a comparison of results obtained from the symmetric model, and their various advantages in saving computational resources and delivering equivalent results for the solitary wave propagation.

We studied the dynamic response of uniform chains composed of ellipsoidal or cylindrical particles as well as hollow spheres. We found that the particles' geometry and orientation

provides additional design parameters for controlling the dynamic response of the system, compared to chains composed of spherical particles. Using the FEM, we found the contact interaction relationship between two particles as a function of particles' geometry and orientation. Numerical dynamic simulations revealed that the uniform chains composed of non-spherical granular particles support the formation and propagation of HNSWs. The characteristics of these waves were studied using analytical expressions based on the elliptical contact laws and found in excellent agreement with experimental data.

We also studied the interaction of HNSWs with boundaries composed of a granular chain and a linear elastic medium using experiments and numerics (finite element and discrete particle models). The comprehensive study revealed the formation of reflected solitary waves dependent on the nature of adjoining elastic media single- or multi-layered (uniform or composite media) cylinders. We explained the observed wave dynamics behavior between the two media by using the long-wavelength approximation in a granular system and particle dynamics in the vicinity of an interface. The reflected solitary waves were found to retain compact support without significant oscillations or dispersion effects.

We also investigated the interaction of granular media with thin large plates by varying the particle diameter and the plate thickness. For the thin plate as an adjacent media, we found that the reflected waves' properties are significantly affected by the inelasticity effects inherent to large plates. We found that the magnitude of the reflected waves decreases with the decrease in the aspect ratio. We also studied the effects of plate boundary conditions and found that there exists a critical distance from the plate boundary after which the part of energy imparted in the plate is lost, primarily in the form of A_0 mode of Lamb wave and Rayleigh wave, and the responses of the reflected waves in granular chain from the interface become independent of the distance between impact point and plate boundary.

The propagation of HNSWs in the experimental system of granular particles is dissipative in nature, which motivated us to study the wave decay in the uniform one-dimensional chain of spherical particles for different materials (stainless steel, teflon, and brass). We developed an analytical model to incorporate the dissipative effects and energy losses in the wave propagation based on a modified Hertzian contact law, where we added

an empirical dissipative term which depends on the relative velocities between adjacent particles. The exponents and prefactors of the dissipative terms were determined using an optimization scheme. In the FEM, we included linear Rayleigh damping parameters and used root-mean-square deviation to obtain the optimized mass-proportional damping factor. The experimental results were found to be in good agreement with the proposed analytical and finite element models in terms of capturing the evolution of the wave amplitude and wave shape in time. The experimental results showed that when the particles composing the chain are made of soft material, like rubber, PTFE, etc, the dissipative effects not only affect the wave amplitude, but it also affects the wave shape too. The current model only used the mass proportional damping effects, it is not capable of capturing the complete wave form, especially when the particles composing the chains are highly dissipative or viscous. The addition of stiffness proportional damping effects will provide additional degree of freedom in capturing both wave amplitude and wave shape for highly damped system, nevertheless, since the dissipative modeled used in finite element method is linear in nature, it may not be able to capture the overall nonlinear effects of energy losses.

The current finite element model of granular chains was restricted to a fully elastic material response of the particles. In the future, the inclusion of plasticity, viscoelastic, and inelastic material behavior for modeling the particles can provide a better understanding of the physical response of the system under large dynamic loading, and the contribution of energy losses due to various dissipative factors. Inclusion of a high strain rate in the finite element model will be essential in applications where HNSWs are used as dampers or applications with large dynamic loadings. Addition of these parameters to the finite element model can make it computationally expensive, as they can create convergence issue. Also the current finite element model for the HNSWs is restricted to one-dimensional chain of particles. Extending the model to two- and three-dimensional structures can be computationally challenging, as they will also lack the simplicity of axisymmetry. Nevertheless, the finite element model of HNSWs is a great tool and the model can be further developed to include the thermal effects, especially during the interaction of HNSWs with structures and it can be extended to study the interactions of HNSWs with complicate structures used in physical applications.

In many physical applications, such as airplane wings, cars, and ships, the body is made of plate/composite like structures. The work done here represents the first work—numerically, experimentally, and analytically—towards understanding the coupling between nonlinear granular media and adjacent linear elastic media. The preliminary study done in this research establishes the foundation that the HNSWs can be used as information carriers for the actuation and sensing of mechanical properties and boundary effects of adjoining media in non-destructive evaluation (NDE) and structural health monitoring (SHM).

Bibliography

- Basile Audoly and Yves Pomeau. *Elasticity and geometry: from hair curls to the nonlinear response of shells*. Oxford University Press, 2010. [78](#)
- Michael Bauccio. *ASM Metals Reference Book, Third Edition*. American Society for Metals, Materials Park, OH, 1993. [16](#)
- Leon Brillouin. *Wave Propagation in Periodic Structures*. McGraw-Hill, Dover Publications Inc, New York, 1946. [9](#)
- C. Brunhuber, F. G. Mertens, and Y. Gaididei. Envelope solitons on anharmonic damped atomic chains. *Physical Review E*, 73(1):016614, Jan 2006. doi: 10.1103/PhysRevE.73.016614. [1](#), [29](#), [47](#)
- Ricardo Carretero, Devvrath Khatri, Mason Porter, Panayotis Kevrekidis, and Chiara Daraio. Dissipative solitary waves in periodic granular media. *Physical Review Letters*, 102(024102), 2009. [xvi](#), [29](#), [47](#), [55](#), [56](#)
- William Carter and Stanley Marsh. Hugoniot equation of state of polymers. *Los Alamos National Laboratory LA-13006-MS*, 1995. doi: 10.2172/95183. [xxvii](#), [18](#), [23](#)
- Thomas K. Caughey. Classical normal modes in damped linear systems. *Journal of Applied Mechanics*, 27(269–271), 1960. [52](#)
- Anindya Chatterjee. Asymptotic solution for solitary waves in a chain of elastic spheres. *Physical Review E*, 59(5):5912–5919, May 1999. doi: 10.1103/PhysRevE.59.5912. [1](#), [14](#), [29](#), [92](#)

- C. Coste and B. Gilles. On the validity of hertz contact law for granular material acoustics. *The European Physical Journal B - Condensed Matter and Complex Systems*, 7:155–168, 1999. ISSN 1434-6028. 10.1007/s100510050598. [14](#), [15](#)
- C. Coste, E. Falcon, and S. Fauve. Solitary waves in a chain of beads under hertz contact. *Physical Review E*, 56:6104–6117, Nov 1997. doi: 10.1103/PhysRevE.56.6104. [1](#), [13](#), [14](#), [15](#), [29](#), [57](#)
- P. A. Cundall and O. D. L. Strack. A discrete numerical model for granular assemblies. *Geotechnique*, 29:47–65, 1979. doi: 10.1680/geot.1979.29.1.47. [28](#)
- Chiara Daraio and Vitali Nesterenko. Strongly nonlinear waves in a chain of polymer coated steel beads. *Physical Review E*, 73(026612), 2006. [1](#), [2](#), [15](#)
- Chiara Daraio and Piervincenzo Rizzo. Method and device for actuating and sensing highly nonlinear solitary waves in surfaces, structures and materials. *United States Patent Application*, (20090199643), October 2008. [83](#)
- Chiara Daraio, Vitali Nesterenko, Eric Herbold, and Sungho Jin. Strongly nonlinear waves in a chain of teflon beads. *Physical Review E*, 72(016603), 2005. [1](#), [2](#), [14](#), [15](#), [17](#), [18](#), [29](#), [30](#), [57](#), [58](#)
- Chiara Daraio, Vitali Nesterenko, Eric Herbold, and Sungho Jin. Energy trapping and shock disintegration in a composite granular medium. *Physical Review E*, 96(058002), 2006a. [2](#), [14](#)
- Chiara Daraio, Vitali Nesterenko, Eric Herbold, and Sungho Jin. Tunability of solitary wave properties in one dimensional strongly nonlinear phononic crystals. *Physical Review E*, 73(026610), 2006b. [1](#), [2](#), [12](#), [13](#), [14](#), [15](#), [17](#), [29](#), [57](#), [58](#), [72](#), [126](#)
- Charles-Augustin de Coulomb. An essay on rules of maxima and minimis a few static problems relating to architecture. *Memory of Mathematics and Physics*, 7:343–382, 1776. [6](#)
- Robert Doney and Surajit Sen. Decorated, tapered, and highly nonlinear granular chain. *Physical Review Letters*, 97:155502, 2006. [1](#)

- Jacques Duran. *Sands, Powders, and Grains: An Introduction to the Physics of Granular Materials*. Springer-Verlag, New York, 2000. [6](#)
- E. Falcon, C. Laroche, S. Fauve, and C. Coste. Behavior of one inelastic ball bouncing repeatedly off the ground. *The European Physical Journal B – Condensed Matter and Complex Systems*, 3(1):45–57, 1998a. doi: 10.1007/s100510050283. [47](#), [84](#)
- E. Falcon, C. Laroche, S. Fauve, and C. Coste. Collision of a 1-d column of beads with a wall. *The European Physical Journal B – Condensed Matter and Complex Systems*, 5: 111–131, 1998b. ISSN 1434–6028. doi: 10.1007/s100510050424. [84](#)
- Efunda Inc. Stainless steel aisi type 316, 2011. [xxvii](#), [16](#), [18](#), [23](#)
- Damien Eggenpieler, Chiara Daraio, and Devvrath Khatri. Automated actuator device for the excitation of tunable highly nonlinear waves in granular systems. U.S. Serial/Patent 61/135,266, 2008. [83](#), [126](#)
- Michael Faraday. On a peculiar class of acoustical figures; and on certain forms assumed by groups of particles upon vibrating elastic surfaces. *Philosophical Transactions of the Royal Society of London*, 121:299–340, 1831. ISSN 02610523. [6](#)
- E. Fermi, J.R. Pasta, and S.M. Ulam. Studies of the nonlinear problems. *University of Chicago Press*, 2(978–988), 1965. [11](#)
- Gero Friesecke and Jonathan A. D. Wattis. Existence theorem for solitary waves on lattices. *Communications in Mathematical Physics*, 161:391–418, 1994. ISSN 0010-3616. doi: 10.1007/BF02099784. [13](#)
- Guanghai Fu. An extension of hertz’s theory in contact mechanics. *Journal of Applied Mechanics*, 74(2):373–374, 2007. doi: 10.1115/1.2188017. [9](#)
- Werner Goldsmith. *Impact: The Theory and Physical Behaviour of Colliding Solids*. Courier Dover Publications, New York, 2001. [25](#), [91](#)
- Upendra Harbola, Alexandre Rosas, Aldo H. Romero, Massimiliano Esposito, and Katja Lindenberg. Pulse propagation in decorated granular chains: An analytical approach. *Physical Review E*, 80(5):051302, Nov 2009. doi: 10.1103/PhysRevE.80.051302. [1](#), [29](#)

- Tedric Harris. *Rolling Bearing Analysis*. Wiley-Interscience, New York, 2001. [72](#)
- E. B. Herbold and V. F. Nesterenko. Shock wave structure in a strongly nonlinear lattice with viscous dissipation. *Physical Review E*, 75(2):021304, Feb 2007. doi: 10.1103/PhysRevE.75.021304. [1](#), [29](#), [47](#)
- Eric B. Herbold, Vitali F. Nesterenko, and Chiara Daraio. Influence of controlled viscous dissipation on the propagation of strongly nonlinear waves in stainless steel based phononic crystals. *AIP Conference Proceedings*, 845(1):1523–1526, 2006. doi: 10.1063/1.2263614. [1](#), [2](#), [47](#), [48](#)
- Heinrich Hertz. Contact between solid elastic bodies. *Journal of Pure and Applied Mathematics*, 92, 1882. [7](#), [8](#), [59](#)
- E. J. Hinch and S. Saint-Jean. The fragmentation of a line of balls by an impact. *Proceedings: Mathematical, Physical and Engineering Sciences*, 455(1989):3201–3220, 1999. ISSN 13645021. [48](#)
- Jongbae Hong. Universal power-law decay of the impulse energy in granular protectors. *Physical Review Letters*, 94:108001, 2005. [1](#)
- Jongbae Hong and Aiguo Xu. Nondestructive identification of impurities in granular medium. *Applied Physics Letters*, 81(25):4868–4870, 2002. ISSN 00036951. doi: 10.1063/1.1522829. [2](#), [84](#)
- Thomas J. R. Hughes and Englewood Cliffs. *The Finite Element Method: Linear Static and Dynamic Finite Element Analysis*. Dover Publications, Prentice-Hall, 1987. [52](#)
- S. C. Hunter. Energy absorbed by elastic waves during impact. *Journal of the Mechanics and Physics of Solids*, 5(3):162–171, 1957. ISSN 0022–5096. doi: 10.1016/0022-5096(57)90002-9. [91](#), [102](#)
- Jeong-Young Ji and Jongbae Hong. Existence criterion of solitary waves in a chain of grains. *Physics Letters A*, 260(1–2):60–61, 1999. ISSN 0375–9601. doi: 10.1016/S0375-9601(99)00488-0. [13](#)

- Stéphane Job, Francisco Melo, Adam Sokolow, and Surajit Sen. How hertzian solitary waves interact with boundaries in a 1d granular medium. *Physical Review Letters*, 94(17):178002, May 2005. doi: 10.1103/PhysRevLett.94.178002. [2](#), [14](#), [15](#), [48](#), [57](#), [84](#), [105](#)
- Stéphane Job, Francisco Santibanez, Franco Tapia, and Francisco Melo. Wave localization in strongly nonlinear hertzian chains with mass defect. *Physical Review E*, 80(2):025602, Aug 2009. doi: 10.1103/PhysRevE.80.025602. [1](#), [14](#), [29](#)
- K. L. Johnson. *Contact Mechanics*. Cambridge University Press, Cambridge, 1987. [8](#), [22](#), [36](#), [47](#), [59](#), [60](#), [61](#), [62](#), [70](#)
- Devvrath Khatri, Chiara Daraio, and Piervincenzo Rizzo. Highly nonlinear waves' sensor technology for highway infrastructures. *Nondestructive Characterization for Composite Materials, Aerospace Engineering, Civil Infrastructure, and Homeland Security 2008*, 6934(1):69340U, 2008. doi: 10.1117/12.775848. [83](#), [126](#)
- Devvrath Khatri, Chiara Daraio, and Piervincenzo Rizzo. Coupling of highly nonlinear waves with linear elastic media. *Sensors and Smart Structures Technologies for Civil, Mechanical, and Aerospace Systems 2009*, 7292(1):72920P, 2009. doi: 10.1117/12.817574. [83](#)
- D. J. Korteweg and De Vries. On the change of form of long waves advancing in a rectangular canal, and on a new type of long stationary waves. *Edinburgh and Dublin Philosophical Magazine and Journal of Science*, 39(422–443), 1895. [11](#)
- A. N. Lazaridi and V. F. Nesterenko. Observation of a new type of solitary waves in a one-dimensional granular medium. *Journal of Applied Mechanics and Technical Physics*, 26:405–408, 1985. ISSN 0021–8944. 10.1007/BF00910379. [13](#), [15](#)
- R. S. MacKay. Solitary waves in a chain of beads under hertz contact. *Physics Letters A*, 251(3):191–192, 1999. ISSN 0375–9601. doi: 10.1016/S0375-9601(98)00867-6. [13](#)
- Felicia S. Manciu and Surajit Sen. Secondary solitary wave formation in systems with generalized hertz interactions. *Physical Review E*, 66(1):016616, July 2002. doi: 10.1103/PhysRevE.66.016616. [84](#)

- Marian Manciu, Surajit Sen, and Alan J. Hurd. Crossing of identical solitary waves in a chain of elastic beads. *Physical Review E*, 63(1):016614, Dec 2000. doi: 10.1103/PhysRevE.63.016614. [13](#), [14](#)
- Marian Manciu, Surajit Sen, and Alan J. Hurd. Impulse propagation in dissipative and disordered chains with power-law repulsive potentials. *Physica D: Nonlinear Phenomena*, 157(3):226–240, 2001. ISSN 0167–2789. doi: 10.1016/S0167-2789(01)00302-5. [47](#), [48](#)
- Daniel Maugis. *Contact, Adhesion and Rupture of Elastic Solids*. Springer-Verlag, New York, 2010. [91](#)
- Vitali Nesterenko. Propagation of nonlinear compression pulses in granular media. *Journal of Applied Mechanics and Technical Physics*, 5(733–743), 1983. [1](#), [11](#), [12](#), [13](#), [29](#), [62](#), [72](#)
- Vitali Nesterenko. *Dynamics of Heterogeneous Materials*. Springer-Verlag, New York, 2001. [1](#), [2](#), [11](#), [12](#), [13](#), [20](#), [29](#), [49](#), [57](#), [62](#), [63](#), [64](#), [72](#), [90](#), [92](#), [115](#)
- Vitali Nesterenko, Chiara Daraio, Eric Herbold, and Sungho Jin. Anomalous wave reflection at the interface of two strongly nonlinear granular media. *Physical Review Letters*, 95:158702, Oct 2005. doi: 10.1103/PhysRevLett.95.158702. [2](#), [29](#), [84](#)
- Sir Isaac Newton. *The mathematical principles of natural philosophy, Volume 2*. Benjamin Motte, London, 1729. [9](#)
- Carino Nicholas. *The Impact-Echo Method: An Overview: Section 6, Chapter 1*. ASCE Publications, New York, 2001. [83](#)
- Ivindra Pane and Eberhard Blank. Role of plasticity on indentation behavior: Relations between surface and subsurface responses. *International Journal of Solids and Structures*, 43(7-8):2014, 2006. ISSN 0020–7683. doi: 10.1016/j.ijsolstr.2005.08.010. [48](#)
- L. Pauchard and S. Rica. Contact and compression of elastic spherical shells: The physics of a ‘ping-pong’ ball. *Philosophical Magazine Part B*, 78(2):225–233, 1998. doi: 10.1080/13642819808202945. [77](#), [80](#)

- L. Pauchard, Y. Pomeau, and S. Rica. Deformation of elastic shells. *Comptes Rendus de l'Academie des Sciences Series IIB Mechanics Physics Chemistry Astronomy*, 324(7): 411–418, 1997. doi: doi:10.1016/S1251-8069(99)80052-9. [77](#)
- Mason Porter, Chiara Daraio, Eric Herbold, Ivan Szelengowicz, and Panayotis Kevrekidis. Highly nonlinear solitary waves in phononic crystal dimers. *Physical Review E*, 77(015601), 2008. [2](#), [14](#), [29](#), [57](#), [58](#)
- Mason Porter, Chiara Daraio, Ivan Szelengowicz, Eric Herbold, and Panayotis Kevrekidis. Highly nonlinear solitary waves in heterogeneous periodic granular media. *Physica D: Nonlinear Phenomena*, 238(666-676), 2009. [2](#), [14](#), [29](#), [57](#), [58](#)
- John Prescott. *Applied Elasticity*. Dover Publications, New York, 1946. [61](#)
- M. J. Puttock and E. G Thwaite. *Elastic compression of spheres and cylinders at point and line contact*. Commonwealth Scientific and Industrial Research Organization, Melbourne, 1969. [61](#)
- J. N. Reddy. *An Introduction to the Finite Element Method*. McGraw–Hill, New York, 1993. [41](#)
- J. Reed. Energy–losses due to elastic wave-propagation during an elastic impact. *Journal of Physics D:Applied Physics*, 18(12):2329–2337, 1985. [91](#), [102](#), [115](#), [117](#)
- Michel Remoissenet. *Waves Called Soliton – Concepts and Experiments*. Springer-Verlag, Berlin, 1999. [1](#)
- Osborne Reynolds. Lvii. on the dilatancy of media composed of rigid particles in contact. with experimental illustrations. *Philosophical Magazine Series 5*, 20(127):469–481, 1885. doi: 10.1080/14786448508627791. [6](#)
- Patrick Richard, Mario Nicodemi, Renaud Delannay, Philippe Ribiere, and Daniel Bideau. Slow relaxation and compaction of granular systems. *Nature Materials*, 4(2):121–128, Feb 2005. doi: dx.doi.org/10.1038/nmat1300. [6](#)
- E. A. Ripperger. The propagation of pulses in cylindrical bars: An experimental study. pages 29–39, 1953. [25](#)

- Alexandre Rosas and Katja Lindenberg. Pulse dynamics in a chain of granules with friction. *Physical Review E*, 68(4):041304, Oct 2003. doi: 10.1103/PhysRevE.68.041304. [14](#), [48](#)
- Alexandre Rosas, Aldo H. Romero, Vitali F. Nesterenko, and Katja Lindenberg. Observation of two-wave structure in strongly nonlinear dissipative granular chains. *Physical Review Letters*, 98(16):164301, Apr 2007. doi: 10.1103/PhysRevLett.98.164301. [1](#), [14](#), [29](#), [47](#), [48](#)
- Alexandre Rosas, Aldo H. Romero, Vitali F. Nesterenko, and Katja Lindenberg. Short-pulse dynamics in strongly nonlinear dissipative granular chains. *Physical Review E*, 78(5):051303, Nov 2008. doi: 10.1103/PhysRevE.78.051303. [14](#), [48](#)
- H.H. Ruan, Z.Y. Gao, and T.X. Yu. Crushing of thin-walled spheres and sphere arrays. *International Journal of Mechanical Sciences*, 48(2):117–133, 2006. ISSN 0020–7403. doi: 10.1016/j.ijmecsci.2005.08.006. [78](#)
- Surajit Sen and Marian Mănciu. Discrete hertzian chains and solitons. *Physica A*, 268(3):644–649, 1999. doi: doi:10.1016/S0378-4371(99)00107-7. [1](#), [14](#)
- Surajit Sen, Marian Mănciu, and James D. Wright. Soliton-like pulses in perturbed and driven hertzian chains and their possible applications in detecting buried impurities. *Physical Review E*, 57:2386–2397, 1998. [2](#), [29](#)
- Surajit Sen, Jongbae Hong, Jonghun Bang, Edgar Avalos, and Robert Doney. Solitary waves in the granular chain. *Physics Reports*, 462(2):21–66, 2008. ISSN 0370-1573. doi: 10.1016/j.physrep.2007.10.007. [1](#), [13](#), [29](#), [57](#), [72](#)
- Arun Shukla, Martin H. Sadd, Raman Singh, Qiming Tai, and S. Vishwanathan. Role of particle shape and contact profile on the dynamic response of particulate materials. *Optics and Lasers in Engineering*, 19(1–3):99–119, 1993. ISSN 0143–8166. doi: 10.1016/0143-8166(93)90037-L. [57](#)
- Simulia. *Abaqus version 6.8 Documentation*. Dassault Systemes S.A., Providence, RI, 2008. [30](#)

- Robert S. Sinkovits and Surajit Sen. Nonlinear dynamics in granular columns. *Physical Review Letters*, 74(14):2686–2689, April 1995. doi: 10.1103/PhysRevLett.74.2686. [14](#)
- R. Sondergaard, K. Chaney, and C. E. Brennen. Measurements of solid spheres bouncing off flat plates. *Journal of Applied Mechanics*, 57:694–699, 1990. [113](#), [115](#), [120](#)
- Alessandro Spadoni and Chiara Daraio. Generation and control of sound bullets with a nonlinear acoustic lens. *Proceedings of the National Academy of Sciences of the USA*, 107(7230), 2010. [2](#)
- D. A. Spence. Self similar solutions to adhesive contact problems with incremental loading. *Proceedings of the Royal Society of London. Series A. Mathematical and Physical Sciences*, 305(1480):55–80, 1968. doi: 10.1098/rspa.1968.0105. [8](#)
- J. P. A. Tillett. A study of the impact of spheres on plates. *Proceedings of the Physical Society. Section B*, 67(10):794, 1954. [91](#), [115](#), [117](#)
- D. P. Updike and A. Kalnins. Axisymmetric behavior of an elastic spherical shell compressed between rigid plates. *Journal of Applied Mechanics*, 37(3):635–640, 1970. doi: 10.1115/1.3408592. [77](#)
- D. P. Updike and A. Kalnins. Axisymmetric postbuckling and nonsymmetric buckling of a spherical shell compressed between rigid plates. *Journal of Applied Mechanics*, 39(1):172–178, 1972. doi: 10.1115/1.3422607. [77](#)
- Lautaro Vergara. Scattering of solitary waves from interfaces in granular media. *Physical Review Letters*, 95(10):108002, Sep 2005. doi: 10.1103/PhysRevLett.95.108002. [2](#), [84](#)
- Lautaro Vergara. Delayed scattering of solitary waves from interfaces in a granular container. *Physical Review E*, 73(6):066623, Jun 2006. doi: 10.1103/PhysRevE.73.066623. [1](#), [2](#), [29](#), [84](#)
- W. J. Wang and Z. G. Zhu. Dissipative solitary waves in granular crystals. *Physical Review Letters*, 102(2):024102, 2009. [48](#)
- Jinkyu Yang, Devvrath Khatri, Paul Anzel, and Chiara Daraio. Interaction of highly nonlinear solitary waves with thin plates, 2011a. Accepted. [114](#)

Jinkyu Yang, Claudio Silvestro, Devvrath Khatri, Luigi De Nardo, and Chiara Daraio. Interaction of highly nonlinear solitary waves with linear elastic media. *Physical Review E*, 83(046606), 2011b. [85](#)

Clarence Zener. The intrinsic inelasticity of large plates. *Physical Review*, 59:669–673, April 1941. doi: 10.1103/PhysRev.59.669. [113](#), [115](#), [116](#)

Yan Zhu, Arun Shukla, and Martin H. Sadd. The effect of microstructural fabric on dynamic load transfer in two dimensional assemblies of elliptical particles. *Journal of the Mechanics and Physics of Solids*, 44(8):1283–1303, 1996. ISSN 0022–5096. doi: 10.1016/0022-5096(96)00036-1. [15](#), [20](#)